

# **Laser-induced shape transformation of silver nanoparticles embedded in glass**

## **Dissertation**

zur Erlangung des akademischen Grades  
doktor rerum naturalium (Dr. rer. nat.)

vorgelegt der

Naturwissenschaftlichen Fakultät II  
der Martin-Luther-Universität Halle-Wittenberg

von

**Andrei Stalmashonak**

geb. am 25. Mai 1980 in Minsk, Weißrussland

Gutachter:

1. Prof. Dr. Heinrich Graener (Universität Hamburg)
2. Prof. Dr. Gero von Plessen (Physikalisches Institut, RWTH Aachen)
3. PD Dr. Manfred Dubiel (Martin-Luther-Universität Halle-Wittenberg)

verteidigt am 04.12.2009



## List of publications which include the results presented in this work

- I. **A. Stalmashonak**, G. Seifert, H. Graener, A. Podlipensky, M. Leitner, and B. Sepiol, “Multicolor laser assisted deformation of silver nanoparticles in glass,” *Physics, chemistry and application of nanostructures: reviews and short notes to Nanomeeting 2007*, Eds.: V. E. Borisenko, S. V. Gaponenko, V. S. Gurin, 172-175 (WSP, Singapore, 2007).
- II. **A. Stalmashonak**, G. Seifert, and H. Graener, “Optical three-dimensional shape analysis of metallic nanoparticles after laser-induced deformation,” *Opt. Lett.* **32**, 3215-3217 (2007), *Virtual Journal of Ultrafast Science* 6(12) (2007), *Virtual Journal of Nanoscale Science & Technology* 16(22) (2007).
- III. **A. Stalmashonak**, A. A. Unal, G. Seifert, and H. Graener, “Optimization of dichroism in laser-induced transformation of silver nanoparticles in glass,” *Proceedings of SPIE* **7033**, 70331Z (2008).
- IV. A. A. Unal, **A. Stalmashonak**, G. Seifert, and H. Graener, “Femtosecond shape transformation dynamics of silver nanoparticles in glass,” *Proceedings of SPIE* **7032**, 703225 (2008).
- V. **A. Stalmashonak**, A. Podlipensky, G. Seifert, and H. Graener, “Intensity-driven, laser induced transformation of Ag nanospheres to anisotropic shape,” *Appl. Phys. B* **94**, 459-465 (2009).
- VI. A. A. Unal, **A. Stalmashonak**, G. Seifert, and H. Graener, “Ultrafast dynamics of silver nanoparticle shape transformation studied by femtosecond pulse-pair irradiation,” *Phys. Rev. B* **79**, 115411 (2009), *Virtual Journal of Nanoscale Science & Technology* 19(12) (2009).
- VII. **A. Stalmashonak**, G. Seifert, and H. Graener, “Spectral range extension of laser-induced dichroism in composite glass with silver nanoparticles,” *J. Opt. A: Pure Appl. Opt.* **11**, 065001 (2009), selected as feature article.
- VIII. **A. Stalmashonak**, G. Seifert, A. A. Unal, U. Skrzypczak, A. Podlipensky, A. Abdolvand, and H. Graener, “Towards the production of micro-polarizers by irradiation of composite glasses with silver nanoparticles,” *Appl. Opt.* **48**, F38-F44(2009).
- IX. **A. Stalmashonak**, H. Graener, and G. Seifert, “Transformation of silver nanospheres embedded in glass into nanodisks using circularly polarized fs pulses,” *Appl. Phys. Lett.* **94**, 193111 (2009), *Virtual Journal of Nanoscale Science & Technology* 19(21) (2009).
- X. **A. Stalmashonak**, A. A. Unal, H. Graener, and G. Seifert, “Effects of temperature on laser-induced shape modification of silver nanoparticles embedded in glass,” *J. Phys. Chem. C.* **113**, 12028-12032 (2009).

- XI. A. A. Unal, **A. Stalmashonak**, H. Graener, and G. Seifert, “Time-resolved investigation of laser-induced shape transformation of silver nanoparticles in glass,” *Phys. Rev. B* **80**, 115415 (2009).
- XII. **A. Stalmashonak**, H. Graener, and G. Seifert, “Production of micro-polarizing structures by fs laser irradiation of composite glasses with silver nanoparticles,” in preparation.
- XIII. A. A. Unal, **A. Stalmashonak**, H. Graener, and G. Seifert, “Effects of electron emission strengths on the formation of prolate and oblate spheroids from Ag nanospheres,” in preparation.
- XIV. **A. Stalmashonak**, O. Kiriyyenko, C. Matyssek, W. Hergert, H. Graener, and G. Seifert, “Effect of local electric field enhancement on the shape transformation of Ag nanoparticles embedded in glass,” in preparation.

<b>CHAPTER 1. INTRODUCTION AND GENERAL AIMS .....</b>	<b>1</b>
<b>CHAPTER 2. OPTICAL PROPERTIES OF NANOCOMPOSITES CONTAINING METAL NANOPARTICLES .....</b>	<b>3</b>
2.1. SURFACE PLASMON RESONANCE OF ISOLATED METAL NANOPARTICLES.....	3
2.2 OPTICAL PROPERTIES OF NANOCOMPOSITES WITH HIGH FRACTION OF METAL NANOPARTICLES.....	10
<b>CHAPTER 3. PROCESSES ARISING BY INTERACTION OF THE LASER PULSES WITH METAL NANOPARTICLES INCORPORATED IN DIELECTRIC MEDIA.....</b>	<b>13</b>
3.1. ENERGY RELAXATION FOLLOWING THE EXCITATION OF THE NANOPARTICLE: WEAK PERTURBATION REGIME.....	13
3.2. ELECTRON-PHONON COUPLING AND ELECTRON HEAT CAPACITY OF SILVER UNDER CONDITIONS OF STRONG ELECTRON-PHONON NONEQUILIBRIUM .....	16
3.3. TWO TEMPERATURE MODEL FOR THE STRONG EXCITATION REGIME .....	20
3.4. HEAT TRANSFER FROM THE NANOPARTICLE TO THE GLASS MATRIX .....	22
3.5. PHOTOEMISSION FROM NANOPARTICLES INCORPORATED IN DIELECTRIC MEDIA .....	24
3.5.1. <i>Nonlinear ionization</i> .....	24
3.5.2. <i>Surface plasmon assisted emission of electrons from silver nanoparticles embedded in glass.</i> .....	27
3.5.3. <i>Emission of ions (small clusters) from nanoparticle</i> .....	32
<b>CHAPTER 4. EXPERIMENTAL TECHNIQUE .....</b>	<b>33</b>
4.1. PREPARATION AND CHARACTERIZATION OF GLASS SAMPLES CONTAINING SILVER NANOPARTICLES .....	33
4.2. LASER SYSTEMS USED FOR NANOPARTICLES' SHAPE TRANSFORMATION .....	35
4.3. IRRADIATION TECHNIQUE .....	38
4.4. TEMPERATURE DEPENDENT IRRADIATION .....	38
4.5. SPECTROSCOPIC TECHNIQUE.....	39
4.6. TECHNIQUE USED FOR INVESTIGATION OF INTENSITY DEPENDENCE .....	39
4.7. TECHNIQUE USED FOR OPTICAL DETERMINATION OF NPS SHAPE.....	41
<b>CHAPTER 5. LASER INDUCED SHAPE TRANSFORMATION OF AG NANOPARTICLES EMBEDDED IN SODA-LIME GLASS .....</b>	<b>43</b>
5.1 INFLUENCE OF THE LASER POLARIZATION, PULSE INTENSITY AND NUMBER OF PULSES APPLIED ON NANOPARTICLES' SHAPE .....	44

5.1.1. <i>Optical 3D shape analysis of nanoparticles after laser induced deformation</i> .....	44
5.1.2. <i>Effect of the laser pulse intensity and writing density on the anisotropic shape modifications</i> .....	50
5.1.3. <i>Summary</i> .....	55
5.2. “OFF-RESONANT” EXCITATION: IRRADIATION WAVELENGTH DEPENDENCE.....	55
5.2.1. <i>Long wavelength irradiation</i> .....	56
5.2.2. <i>Subsequent irradiation</i> .....	59
5.2.3. <i>“Residual” peak observed by long wavelength irradiation</i> .....	60
5.2.4. <i>Two wavelengths irradiation</i> .....	61
5.2.5. <i>Summary</i> .....	63
5.3. EFFECTS OF TEMPERATURE ON THE LASER INDUCED MODIFICATIONS OF AG NANOPARTICLES .....	64
5.3.1. <i>Modelling of the heat flow from a laser-excited nanoparticle into the glass matrix (including ejection of ions)</i> .....	65
5.3.2. <i>Irradiation of preheated samples</i> .....	67
5.3.3. <i>Irradiation with different laser repetition rates</i> .....	69
5.3.4. <i>Interpretation of the experimental data and summary</i> .....	70
5.4. LIMITING FACTORS OF LASER-INDUCED DICHROISM IN COMPOSITE GLASSES WITH SILVER NANOPARTICLES .....	73
5.5. MECHANISM OF THE ANISOTROPIC SHAPE MODIFICATIONS OF SPHERICAL AG NANOPARTICLES IN SODA-LIME GLASS UPON FS LASER IRRADIATION .....	75
<b>CHAPTER 6. TOWARDS THE PRODUCTION OF SUB-MICRON POLARIZING STRUCTURES .....</b>	<b>81</b>
6.1. INFLUENCE OF NANOPARTICLES CONCENTRATION ON LASER-INDUCED DICHROISM IN COMPOSITE GLASSES .....	81
6.2. MICRO-POLARIZED MATRIXES .....	86
6.3. SUMMARY .....	88
<b>CHAPTER 7. SUMMARY OF THE WORK.....</b>	<b>89</b>
<b>REFERENCES .....</b>	<b>91</b>

## **Chapter 1. Introduction and general aims**

Glasses and other dielectrics containing metal nanoparticles are very promising materials for photonics applications owing to their unique linear and nonlinear optical properties. These properties are dominated by the strong surface plasmon resonances (SPRs) of the metal nanoparticles. The SPs occur when the electron and light waves couple with each other at a metal-dielectric interface, and they are simply regarded as the collective oscillation of the nanoparticles (NPs) electrons. The spectral position of the SPRs in the compound materials can be designed within a wide spectral range covering the visible and near-infrared spectra by choice of the electronic properties of the metal and the dielectric matrix [1.1,1.2], or by manipulation of size [1.1, 1.3], shape [1.3, 1.4], and spatial distribution [1.5] of the metal clusters. This makes the composite materials very promising candidates for some applications in the field of photonics [1.6, 1.7, 1.8]. One of the main issues in this context is to structure the optical properties of such materials on a micro-, or even submicron scale. This aspect, in fact, occupies many researchers within the scientific community. The scientific interest covers from the study of optical subwavelength structures such as plasmonic waveguides based on metal nanoparticles [1.9, 1.10] to the much larger scale, micrometer scale, where the composite materials are appropriate for production of a number of standard and advanced optical elements such as: gratings, segmented filters, polarizers, etc.

Recently, it was shown that laser-induced techniques represent a very powerful and flexible tool for (local) structuring of the optical properties of composite materials with metal nanoparticles [1.11, 1.12, 1.13, 1.14, 1.15, 1.16, 1.17, 1.18, 1.19]. Particularly, it was discovered that initially spherical silver nanoparticles embedded in soda-lime glass experience a persisting transformation of the shape when irradiated with intense fs laser pulses at a wavelength near to the SP resonance [1.15-1.19]. This was macroscopically observed as an optical dichroism. The irradiation resulted in permanent polarization dependent colour changes.

Although many pieces of knowledge about the mechanisms leading to this shape transformation have been collected in the last years, still further detailed investigations are needed to get a comprehensive picture of the physical processes behind.

This thesis considers aspects of interactions of intense fs laser pulses with silver nanoparticles incorporated in soda-lime glass; and reveals new information concerning the processes arising by excitation of the silver nanoparticles by the laser pulses and leading to structural alterations.

The studies presented in the thesis aim to understand in details the mechanism of NP shape transformation, as well as, to optimize the technique of laser-induced modification of the optical properties of composite materials with metal nanoparticles for production of (sub-)micron structures with high polarization contrast and very broad tunable range of dichroism; that, in turn, will allow this technique to be used in many applications.

For the sake of compactness, comprehensive reviews of optical properties of nanocomposites with metal particles are intentionally avoided. Thus, next chapter of the thesis (Chapter 2) will only briefly review some of these properties. Also throughout the thesis, wherever it was required, the necessary background is provided.

In Chapter 3 an overview of the possible processes arising by interaction of the laser pulses with metal nanoparticles will be given. The calculations describing the energy relaxation in NP-Glass system in strong excitation regime will be developed; and the possible mechanism of the photoionization in our case will be discussed.

Chapter 4 presents preparation technique as well as characterization of silver-doped nanocomposite glasses which were used for the research as samples; and introduces the experimental apparatus.

The fifth chapter provides the key information needed for understanding the physical mechanism leading to the laser-induced transformation of silver nanoparticles embedded in glass. The series of experimental results, investigating the dependences of laser assisted shape modifications of Ag nanoparticles on the laser pulse intensity, excitation wavelength, temperature etc., are presented. At the end, the possible mechanism responsible for the observed effects is discussed.

Afterwards, chapter 6 will present the results on production of polarized microstructures in the glass containing silver nanoparticles using laser irradiation technique. Based on the findings obtained in Chapter 5 and detailed analysis of the influence of NP concentration on the laser-induced shape transformation, a modified technique of irradiation, which enables the production of fine, micron size, polarization and wavelength selective structures with high polarization contrast and large dichroism will be considered.

Chapter 7 then draws the thesis to its conclusions by giving a summary of the main achievements.



## **Chapter 2. Optical properties of nanocomposites containing metal nanoparticles**

Interaction of the light with nanocomposites reveals novel optical phenomena indicating unrivalled optical properties of these materials. The linear and nonlinear optical response of metal nanoparticles is specified by oscillations of the surface electrons in Coulomb well formed by the positively charged ionic core. This type of excitations is called the Surface Plasmon (SP). In 1908 Gustav Mie [2.1] proposed a solution of Maxwell's equations for spherical particles interacting with plane electromagnetic waves, which explains the origin of the SP resonance in extinction spectra and coloration of the metal colloids.

During the last century optical properties of nanoparticles have been extensively studied and metal-dielectric nanocomposites found various applications in different fields of science and technology [2.2, 2.3, 2.4, 2.5, 2.6, 2.7]. Since the optical properties of metal nanoparticles are governed by the surface plasmon resonance, they are strongly dependent on material, size, shape, concentration and distribution of the particles as well as on the properties of the surrounding matrix. Control over these parameters enables such metal-dielectric nanocomposites to become promising media for development of novel nonlinear materials, nanodevices and optical elements.

Thus, in this section the SP resonance and main optical properties of the metal nanoparticles embedded in a dielectric media will be considered. Complete and excellent review of optical properties of nanostructured random media can be found in Ref. 2.8 and 2.9.

### **2.1. Surface plasmon resonance of isolated metal nanoparticles.**

As it was mentioned above, exposure of a metal nanoparticle to an electric field results in a shift of the free conduction electrons with respect to the particles' metal ion-lattice. The resulting surface charges of opposite sign on the opposite surface elements of the particles (see Fig. 2.1) produce a restoring local field within the nanoparticle, which rises with increasing shift of the electron gas relative to the ion background. The coherently shifted electrons of the metal particle together with the restoring field consequently represent an oscillator, whose behavior is defined by the electron density and the geometry of the particle. Throughout this text its resonances are called surface plasmons on metal nanoparticles.

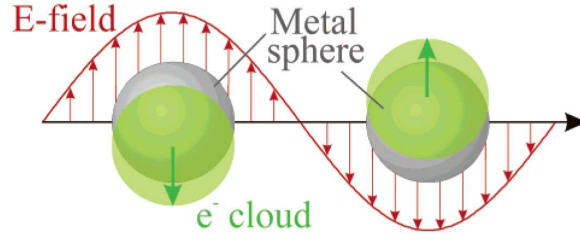


Fig.2.1. Plasmon oscillations in metal sphere induced by electromagnetic wave.

An exact analytical theoretical description of surface plasmons of spherical metal nanoparticles is part of Mie's theory for the scattering and absorption of light by spheres [2.8, 2.10]. According to Mie-theory, the different eigenmodes of the spherical particles are dipolar or multipolar in character. For particles which are small compared to the local variations of the involved electromagnetic fields, the quasistatic approximation [2.8] is valid. It assumes the exciting field to be homogeneous and not retarded over the particle's volume. Under these assumptions, the results of electrostatics can be applied by using the corresponding frequency depended dielectric function. In this case, the polarisability  $\alpha$  and induced dipole moment  $p$  of the metal sphere embedded in dielectric can be given as [2.11]:

$$\alpha = 4\pi R^3 \frac{\epsilon_i(\omega) - \epsilon_h}{\epsilon_i(\omega) + 2\epsilon_h}, \quad (2.1)$$

$$\vec{p}(\omega) = \alpha \epsilon_0 \vec{E}_0(\omega) = 4\pi \epsilon_0 R^3 \frac{\epsilon_i(\omega) - \epsilon_h}{\epsilon_i(\omega) + 2\epsilon_h} \vec{E}_0(\omega), \quad (2.2)$$

where  $R$  is the radius of the nanoparticle,  $E_0$  the electric field strength of an incident electromagnetic wave,  $\epsilon_0$  the electric permittivity of vacuum,  $\epsilon_i(\omega)$  and  $\epsilon_h$  are the relative complex electric permittivity of metal and host matrix, respectively.

In turn, the absorption cross section of a spherical metal inclusion placed in a transparent dielectric matrix, where the imaginary part of the relative complex electric permittivity approaches zero ( $Im[\epsilon_h] \rightarrow 0$ ) is then given as:

$$\sigma(\omega) = 12\pi R^3 \frac{\omega}{c} \epsilon_h^{3/2} \frac{\epsilon_i''(\omega)}{[\epsilon_i'(\omega) + 2\epsilon_h]^2 + \epsilon_i''(\omega)^2}, \quad (2.3)$$

where  $\epsilon_i'(\omega)$  and  $\epsilon_i''(\omega)$  are real and imaginary part of the electric permittivity of the metal, which in turn can be described by the Drude-Sommerfeld formula:

$$\epsilon_i(\omega) = \epsilon_b + 1 - \frac{\omega_p^2}{\omega^2 + i\gamma\omega}. \quad (2.4)$$

Here,  $\gamma$  is a damping constant of the electron oscillations and  $\epsilon_b$  is the complex electric permittivity associated with interband transitions of the core electrons in atom. The free electron plasma frequency is given by:

$$\omega_p = \sqrt{\frac{Ne^2}{m\epsilon_0}}, \quad (2.5)$$

where  $N$  is the density of the free electrons and  $m$  is the effective mass of an electron. As it can be seen from the Eqs. 2.1 – 2.3, the well known Mie resonance occurs at the SP frequency  $\omega_{SP}$  under the following conditions:

$$[\epsilon_i'(\omega) + 2\epsilon_h] + \epsilon_i''(\omega)^2 \rightarrow \text{Minimum}. \quad (2.6)$$

If the imaginary part of the metal electric permittivity is small in comparison with  $\epsilon_i'(\omega)$  or it has small frequency dependence, then Eq. 2.6 can be written as:

$$\epsilon_i'(\omega_{SP}) = -2\epsilon_h. \quad (2.7)$$

Thus, if the condition Eq. 2.7 is complied, the dipole moment and local electric field in the vicinity of the nanosphere grow resonantly and can achieve magnitudes in many orders overcoming the field of the incident wave. This phenomenon is responsible for the SP enhanced nonlinearities of the metal colloids.

As it can be seen, Eq. 2.7 requires the real part of the dielectric function of metals to be negative. This is indeed the case for noble metals in the visible spectral region (Fig. 2.2 for Ag and Au). For a dielectric environment having  $\epsilon_h = 2.25$  surrounding the silver nanoparticle, the resonance condition is observed to occur at around 400 nm, while for gold nanoparticles the resonance wavelength is around 540 nm. A consequence of this is the bright colours exhibited both in transmitted and reflected light.

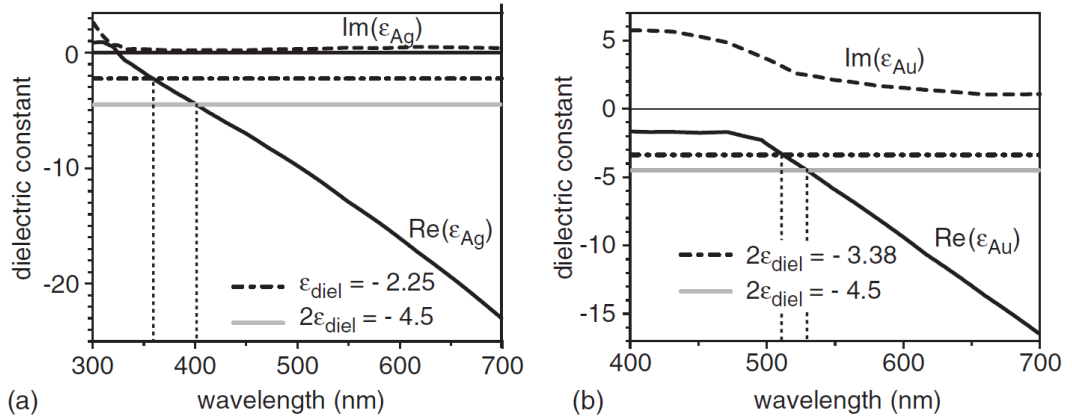


Fig. 2.2. (a) Dielectric constant of silver (solid and dashed lines) and the negative of the dielectric constant of a dielectric media ( $n = 1.5$ ;  $\epsilon_h = 2.25$ ) fulfilling the SPR of nanoparticles condition (grey line). (b) Dielectric constant of gold (solid and dashed lines) and the negative of the dielectric constants of two dielectrics ( $n = 1.3$ ;  $\epsilon_h = 1.69$ , dash-dotted line) and ( $n = 1.5$ ;  $\epsilon_h = 2.25$ , grey line), both fulfilling the SPR of nanoparticles condition. The figure is adapted from Ref. 2.2.

Each of the noble metals has its specific surface plasmon absorption band. For instance, silver nanoparticles embedded in glass matrix exhibit SP band at about 417 nm, as can be seen from the extinction spectra presented in Fig. 2.3. In turn, SP for Au and Cu nanoparticles is shifted in the red spectral range and peaked at 528 nm and 570 nm, respectively. The broad absorption bands below 500 nm for both Au and Cu containing nanocomposite glasses are associated with interband transitions, namely from d- to s-shell, of the core electrons in the metal atoms. However, for silver the interband resonance is peaked at 310 nm (4 eV) far away from the SP resonance [2.12].

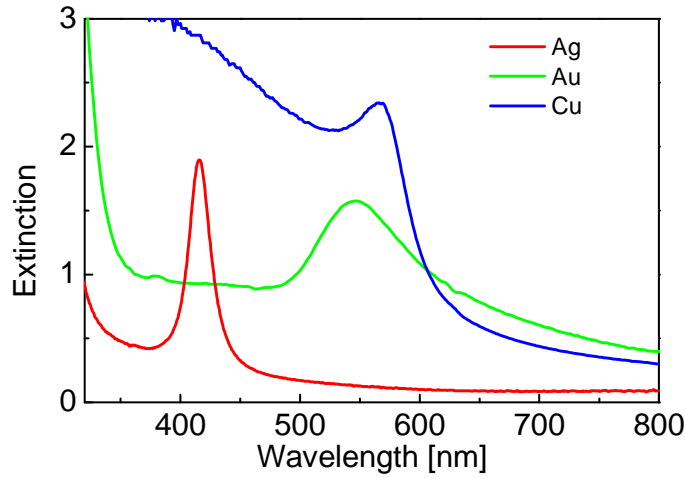


Fig. 2.3. Extinction spectra of glass containing spherical silver, gold and copper nanoparticles.

Using Eq. 2.7 and by substituting the real part of the metal electric permittivity from Eq. 2.4, the position of the SP resonance can be expressed as follows:

$$\omega_{SP}^2 = \frac{\omega_p^2}{\text{Re}[\epsilon_b] + 1 + 2\epsilon_h} - \gamma^2. \quad (2.8)$$

As it can be seen in the Eq. 2.8, the core electrons have a significant influence on the surface plasmon and obviously define the position of the SP resonance in extinction spectra (Fig. 2.3) for different noble metals. On the other hand, the Eq. 2.8 qualitatively describes a dependence of the SP resonance on the dielectric properties of the host matrix, into which the metal nanoparticles are incorporated. An increase of dielectric constant (refractive index) evokes the shift of absorption maximum towards long wavelengths [2.8, 2.13, 2.14] (as it could be expected from Fig. 2.2 and seen in Fig. 2.4). The curves in Fig. 2.4 represent the spectral positions of surface plasmon resonances of silver nanoparticles embedded in three different media: vacuum ( $\epsilon_h=1$ ), glass ( $\epsilon_h=2.25$ ), and  $\text{TiO}_2$  ( $\epsilon_h=6.25$ ). It is clearly seen that the SP resonance maxima are more red-shifted for nanocomposites with higher dielectric constant of the matrix.

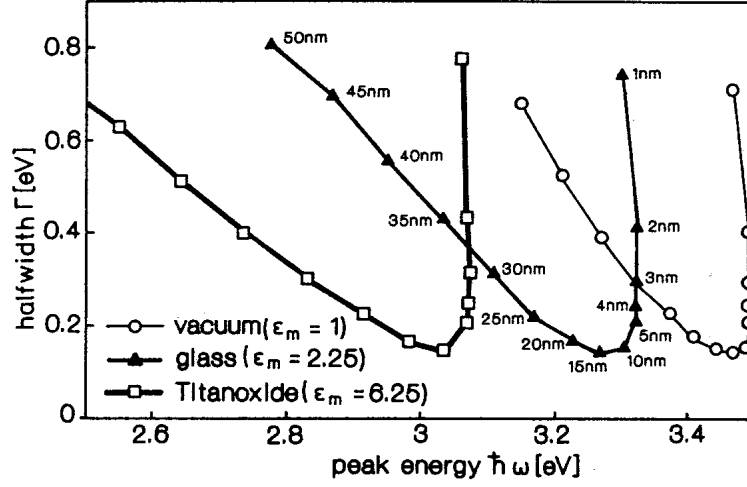


Fig. 2.4. Halfwidth of the surface plasmon resonance of silver nanoparticles versus the respective peak energy for several embedding media and particles size. Parameters with curves are the nanoparticles size. The figure is adapted from Ref. 2.8.

This Fig. 2.4 also shows that the position of the SP resonance depends on the size of metallic nanoparticles. In fact, its position remains quasi-constant for the nanoparticles with radius smaller than 15 nm, while the band halfwidth for these clusters differs by the factor of 4. This is often described as an intrinsic size effect [2.8, 2.15, 2.16]. If the particle size is below the dimension of the mean free path of the electrons in the metal ( $\approx 10\text{-}15$  nm) [2.17], the electron scattering at the particle surface mainly increases the imaginary part of the dielectric function. For the smaller particles ( $> 1$  nm) the spill-out of electrons from the particle surface should be taken into account, which results in an inhomogeneous dielectric function. As a result, very broad plasmon bands are observed for small nanoparticles (Fig. 2.4).

On the other hand, increase in the radius of the nanosphere larger than 15 nm leads to the shift of the SP resonance towards longer wavelengths with simultaneous increase in the band halfwidth (Fig. 2.4 and Fig. 2.5). This effect for the larger particle is referred as the extrinsic size effect [2.8, 2.15, 2.18, 2.19, 2.20]. Here, higher-order (such as quadrupolar) oscillations of conduction electrons become important. In addition to the red shift and broadening of SP band, Fig. 2.5 for silver shows the second peak in extinction spectra, which is the result of these quadrupole effects.

From the size dependence of the SP it is quite obvious that metal nanoparticle with nonspherical shape will show several SP resonances in the spectra. For instance, the ellipsoidal particles with axes  $a \neq b \neq c$  own three SP modes corresponding to polarizabilities along principal axes given as:

$$\alpha_k(\omega) = \frac{4\pi}{3} abc \frac{\epsilon_i(\omega) - \epsilon_h}{\epsilon_h + (\epsilon_i(\omega) + \epsilon_h)L_k}, \quad (2.9)$$

where  $L_k$  is the geometrical depolarization factor for each axis ( $\sum L_k = 1$ ). Moreover, increase in the axis length leads to the minimization of the depolarization factor. For the spherical particle  $L_a = L_b = L_c = \frac{1}{3}$ .

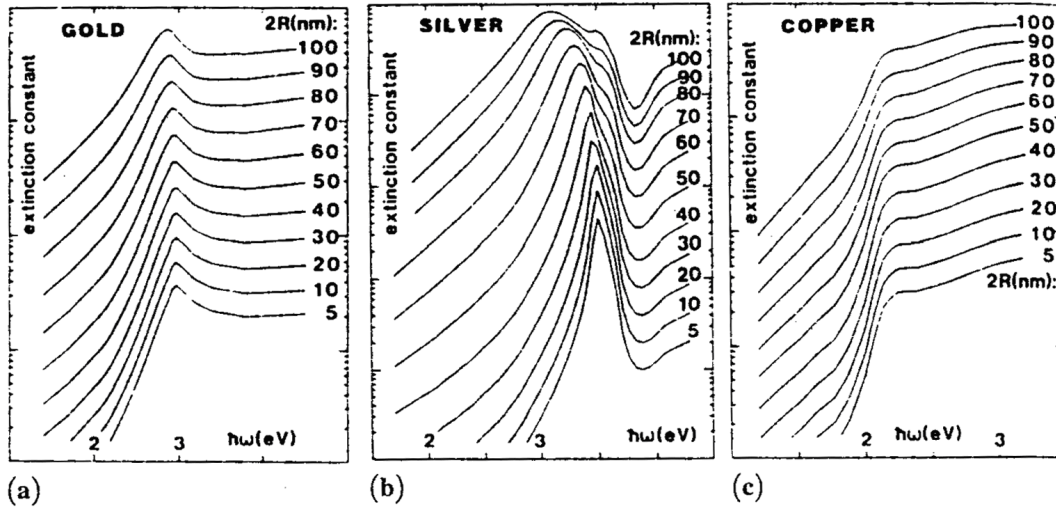


Fig. 2.5. Calculated Mie extinction spectra of spherical nanoparticles of various metals. Parameter is the size  $2R$ .  $\epsilon_i=1$ . The figure is adapted from Ref. 2.8.

Thus, if the propagation direction and polarization of the electromagnetic wave do not coincide with the axes of the ellipsoid, the extinction spectra can demonstrate three separate SP bands corresponding to the oscillations of free electrons along axes [2.8]. For spheroids  $a \neq b = c$  the spectra demonstrate two SP resonances. However, if the light is polarized parallel to one of the axis, only one single SP band corresponding to appropriate axis is seen (Fig. 2.6). Moreover, the band lying at higher wavelengths is referred to the long axis, while the small axis demonstrates resonance at shorter wavelengths compared to the single resonance of a nanosphere of the same volume. The spectral separation of the two surface plasmon bands of the ellipsoidal nanoparticle, as it was shown in the Ref. 2.21, depends strongly on its aspect ratio, which is defined as the ratio of the long to the short axes.

Fig. 2.6 shows the calculated (using the Mie theory for spheroids [2.22]) polarized extinction spectra of prolate ( $a = b < c$ ) and oblate ( $a = b > c$ ) silver spheroids with different aspect ratios, which are embedded in glass. The volume of spheroids is equal to the volume of the nanosphere with radius of 15 nm. As the nanosphere shape is distorted to become a spheroid, two resonances of electron oscillations are created. The red-shifted (in respect to the original SP band of spherical silver nanoparticles which is lying at  $\sim 410$  nm) bands are obtained for the light polarized along the long axis, while the blue-shifted bands refer to the short axis. The spectral gap between SP bands rises for the nanoparticles with higher aspect ratios. However, at the same time, it is clearly seen that for prolate and oblate spheroids having the same aspect ratio, the positions of SP resonances are different. Namely, the spectral

separation between SP bands is higher for the nanoparticles having zeppelin-like shape.

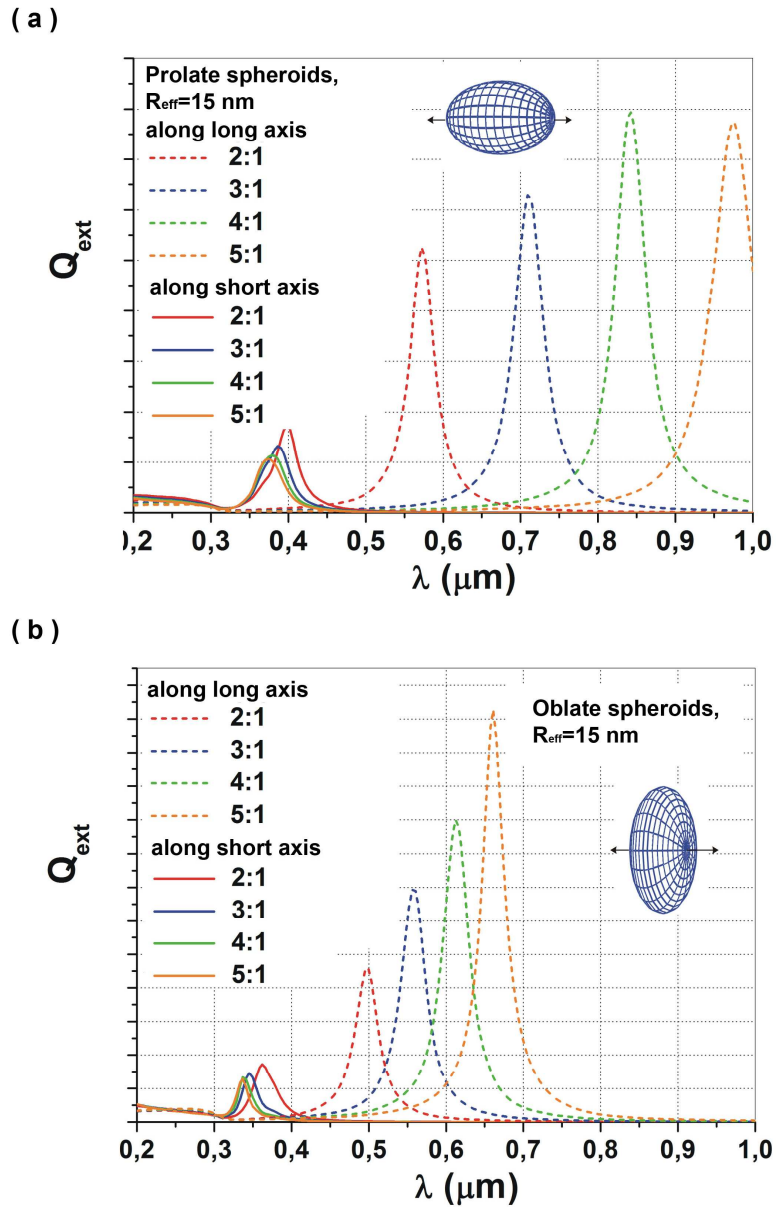


Fig. 2.6. Calculated using the Mie theory for spheroids [2.22] polarized extinction spectra of prolate (a) and oblate (b) silver spheroids with different aspect ratios, which are embedded in glass. The volume of spheroids is equal to the volume of the nanosphere with radius of 15 nm. Dashed curves – polarization of the light is parallel to the long axis; solid line – parallel to the short axis. In insets, the shapes of spheroids are shown schematically.

For many years now, the dichroic property of elongated metallic nanoparticles has been used for manufacturing of broad-band high-contrast polarizers [2.23]. This became possible owing to the fact that by appropriate choice of aspect ration between

the axes of the nanoparticles, the position of the SP resonance can be designed within a broad spectral range. This aspect will be discussed in more detail in the next chapters.

## 2.2 Optical properties of nanocomposites with high fraction of metal nanoparticles.

Increasing fraction of metal nanoparticles in a medium leads to the decrease of average particle distances. Thus, enhancement of the dipole moment of spherical metal NPs by excitation near to the SP resonance results in strong collective dipolar interactions between nanoparticles, which affect the linear and nonlinear optical properties of a nanocomposite material. For the purpose of this work it is sufficient to describe this effect in the approximation of the well known Maxwell-Garnett theory, which is widely applied to describe the optical properties of metal particles in dielectric matrices [2.9, 2.24, 2.25, 2.26]. Although it does not correctly take into account the multipolar interactions between nanoparticles considered in other works [2.27, 2.28], the Maxwell-Garnett theory can be used in the following because it describes quite well the position and shape of the SP resonance and its dependence on the metal filling factor [2.9].

Thus, the effective dielectric constant  $\varepsilon_{eff}(\omega)$  of a composite material with spherical metal inclusions having a fill factor  $f$  (volume of the silver inclusions per unit volume of the composite material  $f = V_{Ag}/V_{total}$ ) is given by the expression:

$$\varepsilon_{eff}(\omega) = \varepsilon_h \frac{(\varepsilon_i(\omega) + 2\varepsilon_h) + 2f(\varepsilon_i(\omega) - \varepsilon_h)}{(\varepsilon_i(\omega) + 2\varepsilon_h) - f(\varepsilon_i(\omega) - \varepsilon_h)}, \quad (2.10)$$

where  $\varepsilon_i(\omega)$  and  $\varepsilon_h$  are complex electric permittivities of the metal (given by the Eq. 2.4) and host matrix.

Based on this description, complex index of refraction of a composite medium can be defined as

$$n(\omega) = n' + in'' = \sqrt{\varepsilon_{eff}(\omega)}. \quad (2.11)$$

Hence, the absorption coefficient  $\alpha$  and refractive index  $n'$  of the medium with dielectric constant  $\varepsilon_{eff}(\omega)$  can be expressed as

$$\alpha = \frac{2\omega}{c} \text{Im} \sqrt{\varepsilon_{eff}(\omega)}, \quad (2.12)$$

$$n'(\omega) = \text{Re} \sqrt{\varepsilon_{eff}(\omega)}, \quad (2.13)$$

where  $c$  is the light velocity. Using Eqs. (2.10) – (2.13), the absorption cross-section and dispersion spectra [Fig. 2.7(a-b)] of glass with spherical silver nanoparticles can be calculated as a function of the volume filling factor of metal clusters in the glass matrix:  $\varepsilon_h = 2.3$ ,  $\omega_p = 9.2$  eV,  $\gamma = 0.5$  eV [2.29],  $\varepsilon_b = 4.2$  [2.26].



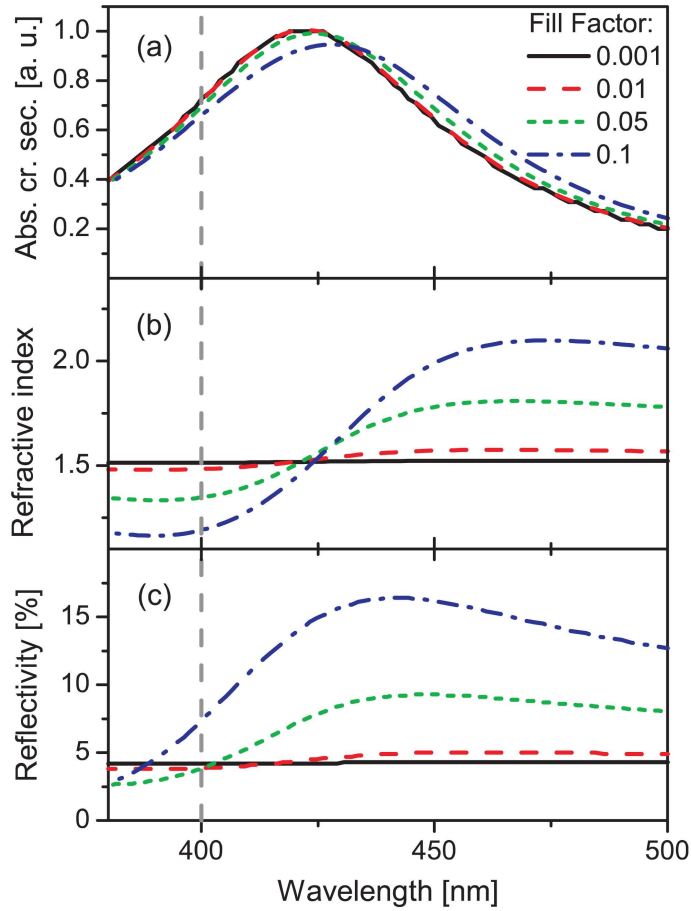


Fig. 2.7. (a) – Absorption cross-section, (b) – dispersion and (c) – reflection spectra of composite glass containing Ag nanoparticles calculated according to the Maxwell–Garnett theory.

It is seen that the collective dipolar interactions between nanoparticles cause a broadening and red shift of the absorption band with increasing filling factor of silver inclusions in the glass matrix [Fig. 2.7(a)]. Also the effective refractive index of the composite glass changes with growing fill factor [Fig. 2.7(b)]: while at low content of silver nanoparticles in glass ( $f = 0.001$ ) the refractive index is actually identical with that of clear glass ( $n' = 1.52$ ), higher fill factor results in significant modifications of dispersion dependences of the composite glass. For  $f = 0.1$ , the refractive index varies between  $\sim 1.2$  and  $2.1$  on the different sides of the SP resonance. Finally, as shown in Fig. 2.7(c), also the sample reflectivity  $R$ , for normal incidence given by

$$R(\omega) = \left| \frac{n(\omega) - 1}{n(\omega) + 1} \right|^2 \quad (2.14)$$

changes upon increasing the volume fill factor. In particular, in the visible range the main effect is an increase of reflectivity of the composite medium with increasing content of spherical Ag nanoparticles.

## **Chapter 3. Processes arising by interaction of the laser pulses with metal nanoparticles incorporated in dielectric media**

This chapter is dedicated to the general understanding of laser pulse interaction with metal nanoparticles. The aim is to collect all physical processes, which may occur when the laser pulse starts to interact with the nanoparticle, as well as all later events and mechanisms, which are triggered by it.

Depending on the laser parameters (e.g. weak and strong excitation regimes) and nanoparticle properties, one can expect various kinds of physical phenomena. Recent investigations of the laser pulse interaction with metal nanoparticles are mostly concentrated on the SP dynamics and the energy exchange (relaxation) mechanisms arising by it (see Ref. 3.1, 3.2, 3.3, 3.4, 3.5, 3.6 for a review). These studies employ weak laser pulses to excite the nanoparticles, thereby ensuring only weak electronical perturbations to the nanoparticle. In such a low perturbation regime, the changes induced to the surface plasmon bands of the nanoparticles are transient and totally reversible. For the strong excitation, however, the energy absorbed by the nanoparticle becomes very high, which creates big perturbation for the nanoparticle electrons resulting in persistent (irreversible) changes to the nanoparticle. In this regime the processes related to the heating and cooling of nanoparticles (e.g. e-e, e-ph scattering, etc.) have to be modified. At the same time, this strong excitation can open up additional channels of the energy relaxation in the form of e.g. hot electron and ion emissions (see for example Ref. 3.7, 3.8, 3.9, 3.10).

As it was mentioned above, the intensities of the laser pulses used in this work are so high that it leads to the irreversible nanoparticles shape modification. Therefore, to explain the presented results, the possible mechanisms that could take place in the strong excitation regime will be discussed in this chapter. Even though it is impossible to account for all the complicated many-body interactions among electrons, phonons, ions, etc., in this regime, some theoretical estimations will be attempted.

### **3.1. Energy relaxation following the excitation of the nanoparticle: Weak perturbation regime**

The absorption of a femtosecond laser pulse produces a coherent collective oscillation of the nanoparticle electrons [Fig. 3.1(a)]. During this quasi-instantaneous

process, the phase memory is conserved between the electromagnetic field and the electronic states, and the density of excited states depends on the spectral shape of the laser pulse. The corresponding electron distribution is non-thermal [3.11, 3.12, 3.13] and lasts for few femtoseconds [3.1, 3.2]. Electrons having energies between  $E_F - \hbar\omega$  and  $E_F$  are excited above the Fermi energy with final energies between  $E_F$  and  $E_F + \hbar\omega$ . The excitation is sketched with rectangular-shaped boxes, whose dimensions are determined by the energy of the exciting laser pulse  $\hbar\omega$  as the length and the absorbed energy density as the width.

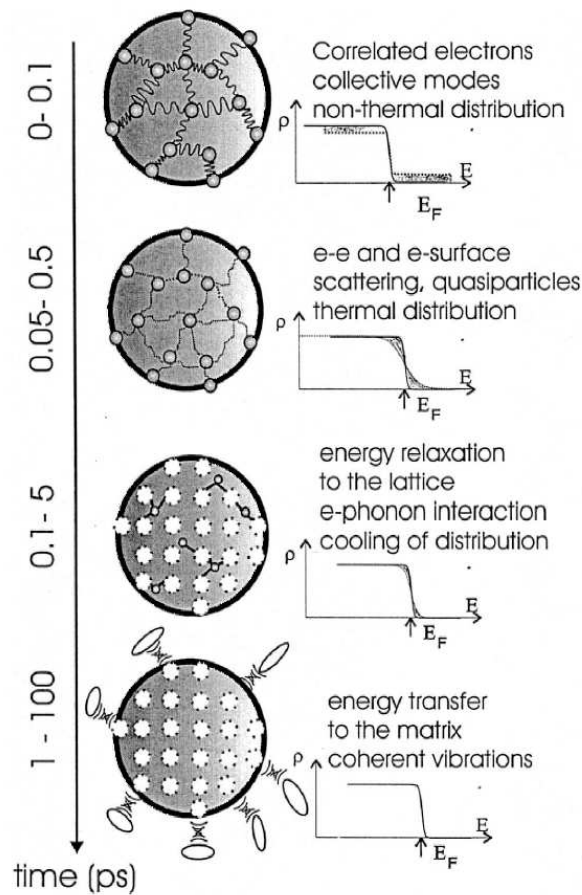


Fig. 3.1. Sketch of the relaxation processes in a metallic nanoparticle. The figure is adapted from Ref. 3.1.

The next step of the energy relaxation corresponds to a thermalization of the electrons. The occupied electronic states tend to a Fermi–Dirac distribution with a well defined temperature which depends on the laser pulse intensity. The phase coherence is lost and the collective modes have decayed into quasi-particle pairs. Figure 3.1(b) shows the equilibrated thermal Fermi distribution following the e-e scattering processes. The excited electrons possess high energies above the Fermi level, and the resulting temperature of the electronic system is much higher compared to the equilibrium temperature before the laser excitation.

Several time-resolved photoemission experiments, performed in noble metal films, have shown that the temporal scale of this thermalization process is of a few hundreds of femtoseconds [3.12, 3.14, 3.15, 3.16, 3.17]. For small particles, with a diameter typically less than a few tens of nanometers, the scattering time of the electrons at the particle surface is also around few hundreds femtoseconds. Voisin et al. [3.18] report an internal electron thermalization time of  $\approx 350$  fs for 12 nm radius Ag nanoparticles in a BaO-P<sub>2</sub>O<sub>5</sub> matrix, which is comparable to the one determined from Ag films [3.19]. The time it takes for the internal thermalization decreases for smaller nanoparticles, for example, it is around 150 fs for 2 nm radius Ag nanoparticles embedded in an Al<sub>2</sub>O<sub>3</sub> matrix. For the 9 and 48 nm Au nanoparticles in solutions, the decay lifetimes of 500 and 450 fs were found, respectively, for the internal electron thermalization [3.2]. The size dependence of the thermalization time is in good agreement with a simple model which phenomenologically introduces surface induced reduction of the Coulomb interaction screening due to the spillout and d-electron wave function localization effects [3.18, 3.20].

Another important mechanism in the electron dynamics, which is shown in Fig. 3.1(c), is the energy transfer to the lattice. The hot electrons cool externally by electron-phonon (e-ph) interactions until the temperatures of the electron gas and the lattice are equilibrated. The resulting electronic temperature is lower than its peak value, but higher than the equilibrium temperature. Since the e-ph interactions occur on a time scale comparable to the internal electron thermalization, a clear separation between e-e and e-ph relaxation as sequential processes is therefore incorrect. It means that the non-thermal electrons of the Fig. 3.1(a) already interact with the phonons during the same time they scatter with themselves to achieve the Fermi distribution of Fig. 3.1(b). This simultaneous e-ph coupling is an important channel of electron relaxation, which heats the nanoparticle lattice in time.

In the last years, many groups attempted to define the time scale of this thermalisation process in different combination of metals and matrixes [3.21, 3.22, 3.23, 3.24, 3.25, 3.26, 3.27, 3.28]. Normally one can expect that the lattice heating takes longer time compared with the electronic heating, and the maximum lattice temperature cannot reach temperatures as high as electron temperatures since the electronic heat capacity is about 2 orders of magnitude smaller than the lattice heat capacity.

In addition, Hartland et. al. show that the thermalisation time depends on the laser intensity [3.8, 3.29]. In the next sections the two temperature model (2TM, in literature also called TTM) that describes the thermal situations of electrons and phonons and the heat transfer between these two systems will be considered in more details. This model will be extended to include very high electronic temperatures to account for the conditions of strong excitation regime.

The last step in the relaxation is the energy transfer to the dielectric matrix [Fig. 3.1(d)]. This transfer corresponds to the heat diffusion from the metal to the environment. It is therefore sensitive to the thermal conductivity of the surrounding medium; and as it will be shown later, it plays one of the important roles in the mechanism of nanoparticles shape transformation. Therefore, this process will be also considered more deeply in the next sections.

### 3.2. Electron-phonon coupling and electron heat capacity of silver under conditions of strong electron-phonon nonequilibrium

Upon pulse interaction with the nanoparticle, the electrons heat up gradually to a hot electronic distribution. During and after their heating, the electrons couple with the nanoparticle lattice vibrations (the phonons) and heat up the nanoparticle. The heat gained by the nanoparticle lattice can be found from the heat lost by the electrons using the two-temperature model (2TM) [3.1, 3.30], where the heat flow between two subsystems (electrons and lattice) is defined by two coupled differential equations. 2TM is the commonly accepted theory to describe the energy relaxation mechanisms between electrons and lattice. The electronic system is characterized by an electron temperature  $T_e$  and the phononic system by a lattice temperature  $T_l$ . The electron-phonon coupling factor  $G(T_e)$  is responsible for the energy transfer between two subsystems. The heat equations describing the temporal evolution of  $T_e$  and  $T_l$  are given as follows:

$$C_e(T_e) \frac{\partial T_e}{\partial t} = -G(T_e)(T_e - T_l) + S(t), \quad (3.1)$$

$$C_l \frac{\partial T_l}{\partial t} = G(T_e)(T_e - T_l), \quad (3.2)$$

where  $C_e(T_e)$  and  $C_l$  are the electronic and lattice heat capacities, respectively;  $S(t)$  in Eq. (3.1) is a source term describing the absorbed laser pulse energy per nanoparticle, which can be given as:

$$S(t) = \frac{I \sigma_{abs}}{V_{NP}} \cdot \exp\left[-4 \ln 2 \cdot (t / \tau_{FWHM})^2\right]. \quad (3.3)$$

Here  $I$  is the peak pulse intensity,  $\sigma_{abs}$  is the absorption cross section of a single nanoparticle ( $\approx 3000 \text{ nm}^2$  for a silver nanoparticle in a dielectric environment with refractive index of  $n = 1.52$  [3.31]);  $V_{NP}$  is the nanoparticle volume, and  $\tau_{FWHM}$  determines the full width at half maximum of the temporal pulse profile.

A key issue in the application of the models based on 2TM for quantitative description of the kinetics of the energy redistribution in the irradiated target is the choice of adequate temperature dependent thermophysical properties of the target material included in the 2TM equation for the electron temperature (Eq. 3.1), namely, the electron-phonon coupling factor, the electron heat capacity, and the heat conductivity. Due to the small heat capacity of the electrons in metals and the finite time needed for the electron-phonon equilibration, irradiation by a short laser pulse can transiently bring the target material to a state of strong electron-lattice nonequilibrium, in which the electron temperature can rise up to tens of thousand Kelvins, comparable to the Fermi energy, while the lattice still remains cold. At such high electron temperatures, the thermophysical properties of the material can be affected by the thermal excitation of the lower band electrons, which, in turn, can be very sensitive to the details of the spectrum of electron excitations specific for each metal. Indeed, it has been shown for Au that in the range of electron temperatures

typically realized in femtosecond laser material processing applications, thermal excitation of d band electrons, located around 2 eV below the Fermi level, can lead to a significant (up to an order of magnitude) increase in the electron-phonon coupling factor and positive deviations of the electron heat capacity from the commonly used linear dependence on the electron temperature [3.32, 3.33]. Thus, the approximations of a linear temperature dependence of the electron heat capacity and a temperature independent electron-phonon coupling factor, used in most of the current 2TM calculations, are inappropriate for the quantitative description of material response to a strong ultrafast laser excitation and should be reconsidered based on the analysis of the electronic structure of a given material. However, for the heat capacity of the nanoparticle lattice ( $C_l$ ) the room temperature values are reasonable approximations, as  $C_l$  does not change so much as the temperature increases. For the case of silver, it is known that the change of  $C_l$  upon lattice temperature increase by 1500 K is less than 20% compared with its room temperature value of  $3.5 \times 10^6 \text{ Jm}^{-3}\text{K}^{-1}$  [3.34].

As it was mentioned, in the literature,  $C_e$  is commonly defined by a linear function of electron temperature in the form  $C_e(T_e) = \gamma T_e$ , where  $\gamma$  is the electronic heat capacity constant. This expression for the electronic heat capacity is only valid at low electron temperatures, where the Sommerfeld expansion of the electronic free energy is commonly used. Electron heat capacity constant of the above expression is given as  $\gamma = \pi^2 k_B^2 g(\varepsilon_F)/3$  and defined by the value of the electron density of states (DOS) at the Fermi level,  $g(\varepsilon_F)$ . Within the frame of free electron gas model,  $\gamma$  can also be associated with the free electron number density  $n$  and the Fermi energy as  $\gamma = \pi^2 n k_B^2 / 2\varepsilon_F$  [3.35].

However, the Sommerfeld expansion is no more valid at high electron temperatures, and the electron heat capacity calculation should include the full spectrum of the electron DOS by taking the derivative of the total electron energy density with respect to the electron temperature [3.35], as given in the following:

$$C_e(T_e) = \int_{-\infty}^{\infty} \frac{\partial f(\varepsilon, \mu, T_e)}{\partial T_e} g(\varepsilon) \varepsilon d\varepsilon, \quad (3.4)$$

where  $g(\varepsilon)$  is the electron DOS at the energy level  $\varepsilon$ ,  $\mu$  is the chemical potential at  $T_e$ , and  $f(\varepsilon, \mu, T_e)$  is the Fermi distribution function of the form

$$f(\varepsilon, \mu, T_e) = \frac{1}{\exp[(\varepsilon - \mu)/k_B T_e] + 1}. \quad (3.5)$$

The evaluation of  $\partial f / \partial T_e$  requires the knowledge of the chemical potential as a function of the electron temperature,  $\mu(T_e)$ . From the conservation of the total number of electrons, the chemical potential can be obtained by setting the result of the integration of the product of the electron DOS and the Fermi distribution function at  $T_e$  over all energy levels to be equal to the total number of electrons  $N_e$  [3.35]

$$N_e = \int_{-\infty}^{+\infty} f(\varepsilon, \mu(T_e), T_e) g(\varepsilon) d\varepsilon. \quad (3.6)$$

Since  $C_e$  depends on the electron temperature, the electron-phonon coupling is also expected to have temperature dependence. The electron-phonon coupling was first analyzed within the free electron gas model by Kaganov *et al.* [3.36]. It was suggested that the electron-lattice energy exchange rate could be expressed in terms of the electron relaxation times at  $T_e$  and  $T_l$ . At lattice and electron temperatures much higher than the Debye temperature and  $T_e \gg T_l$ , the rate of energy transfer from the electrons to the lattice per unit volume can then be expressed as [3.30, 3.36]

$$\frac{\partial E_e}{\partial t} = G(T_l - T_e), \quad G = \frac{\pi^2}{6} \frac{m C_s^2 n}{\tau(T_e) T_e}, \quad (3.7)$$

where  $m$  is the effective electron mass,  $C_s$  is the speed of sound,  $n$  is the number density of electrons, and  $\tau(T_e)$  is the electron relaxation time defined as the electron-phonon scattering time  $\tau_{e-ph}$ , and evaluated under the assumption that the lattice temperature is equal to the electron temperature [3.36]. Electron-phonon scattering time is proportional to the inverse of the lattice temperature and when  $T_e = T_l$ , then  $\tau_{e-ph} \sim 1/T_e$ , which results in a constant value for the  $G$  factor given by Eq. 3.7.

For this reason,  $G$  has been defined in the literature as a constant, temperature independent value that is found either by the above model or by best-fitting the values from the experimental results. Typical  $G$  values used for silver range between  $3 \times 10^{16}$  to  $3.5 \times 10^{16} \text{ Wm}^{-3} \text{K}^{-1}$  [3.1, 3.37, 3.38].

For the strong excitation, however, as it has been mentioned before, high electronic temperatures trigger the thermal excitation of the  $d$ -band electrons located below the Fermi level. For this reason dramatic changes are expected for the rate of the electron-phonon energy exchange. Therefore, the correct treatment of the  $G$  factor in the strong perturbation regime again requires the consideration of the full spectrum of electron DOS (as it was done above for the  $C_e$ ). The resulting expression for the temperature dependent electron-phonon coupling factor can be given by [3.39]

$$G(T_e) = \frac{\pi \hbar k_B \lambda \langle \omega^2 \rangle}{g(\epsilon_F)} \int_{-\infty}^{\infty} g^2(\epsilon) \left( -\frac{\partial f}{\partial \epsilon} \right) d\epsilon, \quad (3.8)$$

where  $\lambda$  denotes the electron-phonon coupling constant, and the value of  $\lambda \langle \omega^2 \rangle$  is 22.5 for silver.

Taking into account the above given theory, it is possible to calculate the dependences of electron heat capacity and electron-phonon coupling factor on the electronic temperature. First of all, looking to the electron DOSs for silver [Fig. 3.2(a)] calculated with Vienna *ab initio* simulation package [3.39, 3.40], one can see the presence of prominent region of high density of states, associated with the  $d$  band located  $\sim 3$  eV below the Fermi level. It is seen, that for the Fermi distribution functions at low electron temperatures,  $T_e \sim 0.1$  eV ( $\sim 10^3$  K), the region of the electron DOS affected by thermal excitations ( $\sim k_B T_e$ ) is similar to that of the free electron gas model, with only  $s$  electrons being excited. At higher electron temperatures,  $T_e \sim 1$  eV ( $\sim 10^4$  K), a significant number of  $d$  band electrons can be excited and can make a substantial contribution to the thermophysical properties of the material. Indeed, at electron temperatures below  $\sim 5000$  K the calculated chemical



potential follow the dependence predicted from the Sommerfeld expansion of the electron free energy in the free electron gas model with one free electron per atom. At higher electron temperatures, however, the thermal excitation of electrons from the high density of states edge of the d band to the lower density of states s band results in the increase of the chemical potential and large deviations from the prediction of the free electron gas model [Fig. 3.2(b)].

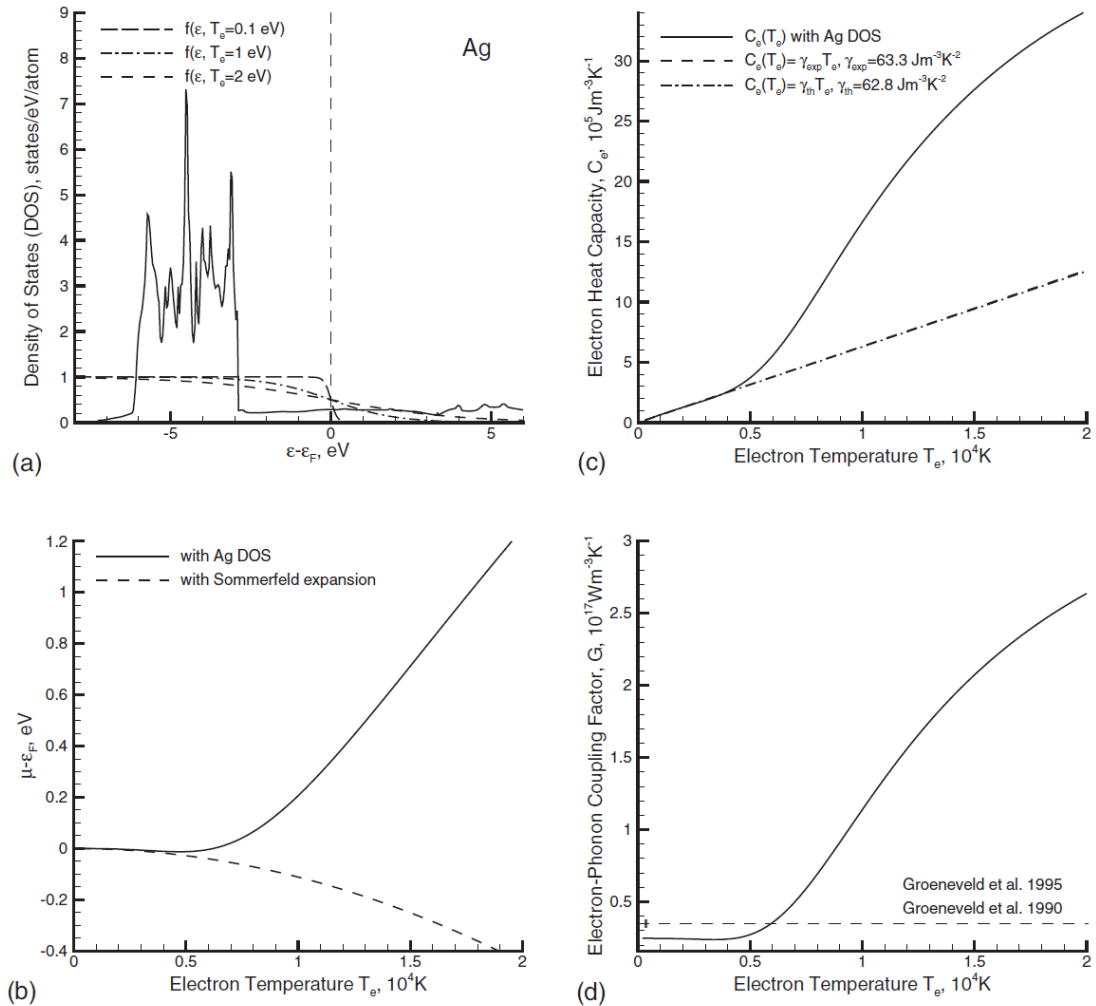


Fig. 3.2. (a) The electron DOS of silver obtained in the electronic structure calculation performed with VASP (solid line) and the Fermi distribution function shown for three different values of the electron temperature (dashed and dash-dotted lines). The Fermi distributions are shown centered at the Fermi level at zero temperature; (b)–(d) Electron temperature dependence of thermophysical properties of silver: (b) the chemical potential, (c) the electron heat capacity, and (d) the electron-phonon coupling factor. Solid lines show the results of the calculations performed with DOS obtained from VASP. Dashed lines in (c) and (d) show the commonly used approximations of the thermophysical material properties based on experimental measurements. Figure is adapted from Ref. 3.39.

The temperature dependence of the  $C_e$  for silver is depicted in Fig. 3.2(c). The deviation between the linear temperature dependence of the  $C_e$  obtained from the free

electron gas model (dashed-dotted line) and the nonlinear temperature dependence of  $C_e$  calculated from Eq. 3.4 (solid line) is clearly seen above  $T_e$  values of  $\sim 5000$  K. The free electron gas model approximates the  $C_e$  values very well up to 5000 K ( $\gamma \approx 63 \text{ Jm}^{-3}\text{K}^{-2}$  is used for Ag [3.41]), and indeed the calculations considering the full DOS (Eq. 3.4) follow closely the same linear dependence. However, further increase of the electron temperatures cause significant changes in the  $C_e$  as a result of the contributions coming from the core electrons, compared to the commonly used linear approximation. Therefore, usage of the linear  $C_e$  dependence in the 2TM could definitely result in an overestimation of the electron temperatures, which proves to be inappropriate for the strong excitation regime (when  $T_e$  is higher than several thousands of Kelvins). This nonlinear behavior of the  $C_e$  for high electron temperatures depends strongly on the electron DOS and should be expected to have different behavior for different metals. Calculations on other noble metals (such as Cu and Au) also show an increase of the  $C_e$  values for higher  $T_e$  [3.39], which is not necessarily the case for other metals.

For the electron-phonon coupling term shown in Fig. 3.2(d) it is seen that it stays nearly constant up to electron temperatures of  $\sim 5000$  K. At higher temperatures a significant strengthening of the  $G$  factor is observed when a large number of  $d$ -band electrons are thermally excited and contribute to the electron-phonon energy exchange. The enhancement of the electron-phonon coupling at high electron temperatures implies a faster energy transfer from the hot electrons to the lattice.

A consequence of the temperature dependent electron-phonon coupling term is that the electron-phonon relaxation times ( $\tau_{e-ph}$ ) increase with increasing electron temperatures and hence the applied laser pulse energy [3.42, 3.43]. Therefore, slightly different electron-phonon relaxation results presented in the literature could be explained by the temperature dependence of the electron-phonon relaxation.

### 3.3. Two temperature model for the strong excitation regime

As it was already discussed, the strong irradiation regime creates huge electron-phonon non-equilibrium conditions due to the very small heat capacity of electrons (at room temperature) and the finite time needed for the electron-phonon equilibration. Thus the high energy fs pulse transiently raises the  $T_e$  over several thousands of Kelvins while the lattice still remains cold.

Taking into account the wide range temperature dependences for the electron heat capacity  $C_e$  and electron-phonon coupling parameter  $G$  given in previous section, one can now solve the coupled heat equations (Eqs. 3.1 and 3.2) for the quantitative modeling of the energy relaxation dynamics followed by the strong irradiation of silver nanoparticles.

As an illustration to this regime, Fig. 3.3(a) depicts the results of 2TM calculations for the case of a single silver nanoparticle excited by a 150 fs pulse with an intensity of  $0.5 \text{ TW/cm}^2$  (above the permanent nanoparticle shape modification threshold [3.44]) and central wavelength of 400 nm ( $\hbar\omega = 3.1 \text{ eV}$ ), i.e., close to the surface plasmon resonance. It is easily seen that, upon absorbing the laser pulse energy, the conduction electrons of the nanoparticle gain very high temperatures ( $\sim 10^4$  K) within

the pulse. Reaching the maximum  $T_e$ , the hot electronic system heats the cold silver lattice to a region of temperatures above the melting point of (bulk) silver within a few picoseconds. The electronic and lattice temperatures meet at a value near 2000 K in 40 ps after the pulse interaction. This suggests the plausibility of the melting of nanoparticles in such a short time. Plech *et al.* observed by time-resolved X-ray scattering studies the melting of gold nanoparticles suspended in water within 100 ps after strong laser pulse excitation [3.45, 3.46]. However, it should be noticed here that these calculations do not take into account the energy transfer to the matrix and losses due to possible electron emission processes from the nanoparticle, which are additional cooling mechanisms of the electronic sea. The details of these cooling processes will be considered in the next sections.

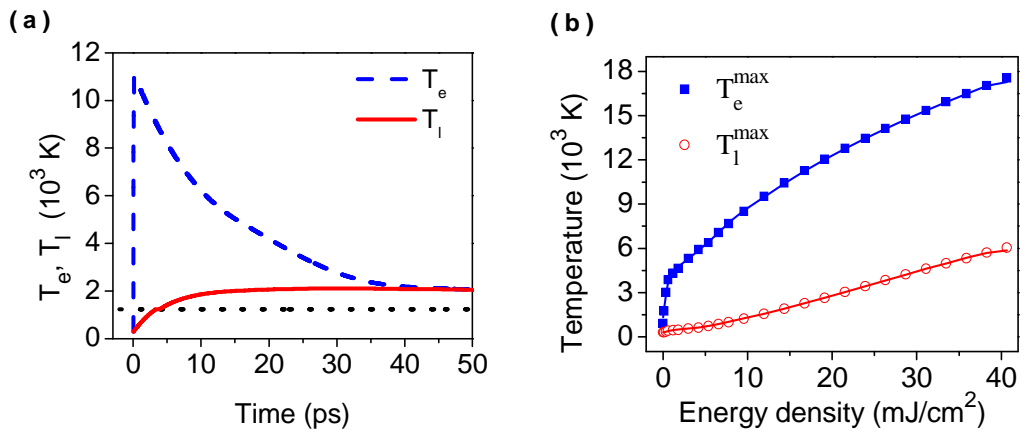


Fig. 3.3. (a) Time evolution of electronic and lattice temperatures of a silver nanoparticle following the absorption of an intense fs laser pulse (around  $20 \text{ mJ/cm}^2$  of energy density). The dotted line at 1235 K marks the melting temperature of bulk silver; (b) The dependences of electronic (blue squares) and lattice (red circles) temperature maxima on a wide range of laser energy densities.

Figure 3.3(b) shows the dependences of electronic and lattice temperature maxima on a wide range of applied energy densities (from very weak up to extreme irradiation conditions). The weak regime (up to  $T_e$  values of 5000 K) shows a rapid increase in electronic temperature owing to the very low electronic heat capacity  $C_e$  in this interval. However, these electrons do not heat up the lattice efficiently due to the less e-ph coupling  $G$ . Further increases in the energy density of the pulses cause higher  $T_e$  values, but the rise of electronic temperature slows down due to the increasing  $C_e$  value. The lattice temperatures are seen to increase with a higher slope in this regime as a result of the increasing efficiency of the  $G$  factor.

As an example, it is useful to mention here that if one would employ standard linear values for  $C_e$  (i.e.  $C_e(T_e) = \gamma T_e$ ), the pulse of energy density  $20 \text{ mJ/cm}^2$  (used in the presented 2TM calculations) would induce the rise of electronic temperature higher than  $10^5 \text{ K}$  and the resulting  $T_l$  values would be much higher than the evaporation temperature, which are definitely not correct.

### 3.4. Heat transfer from the nanoparticle to the glass matrix

The above given 2TM describes only the heat transfer between the electrons and the nanoparticle lattice. To get the complete “thermodynamical” picture of the nanoparticle and the surrounding glass system, this 2TM has to be extended by the heat transfer from the nanoparticle to the glass matrix. The excess energy of the nanoparticle is released to the surrounding via phonon couplings across the nanoparticle-glass interface [3.47, 3.48]. Therefore, cooling of the nanoparticle (and heating of the glass matrix) can be calculated considering energy flow from the hot particle to the glass through a spherical shell of infinitesimal thickness. Heat transfer from this first heated glass shell is then described by ordinary heat conduction. Because of the huge difference in thermal diffusivities of Ag ( $123 \text{ nm}^2/\text{ps}$ ) and glass ( $0.5 \text{ nm}^2/\text{ps}$ ), any temperature gradient within the NP can be neglected when calculating the transient temperatures in the glass around the nanoparticle (Fig. 3.4). The temporal and spatial evolution of temperature within the glass can then be calculated by the radial heat equation, where the rate of temperature change ( $\partial T(r,t)/\partial t$ ) is proportional to the curvature of temperature density ( $\partial^2 T(r,t)/\partial r^2$ ) through the thermal diffusivity ( $\chi$ ) of the glass medium:

$$\frac{\partial T(r,t)}{\partial t} = \chi \frac{\partial^2 [rT(r,t)]}{\partial r^2}. \quad (3.9)$$

The time scales for the particle cooling range from tens of picoseconds to nanoseconds, depending on the laser excitation strength, the size of the nanoparticle and surrounding environment [3.48, 3.49].

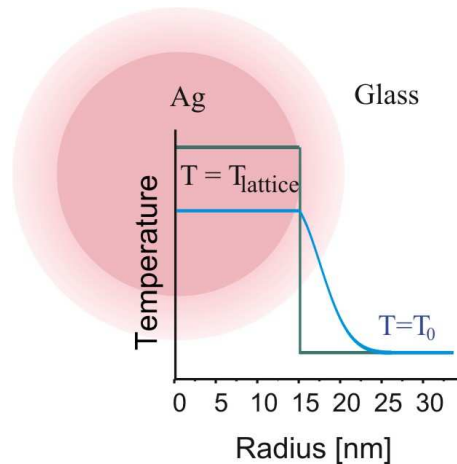


Fig. 3.4. Temperature distribution in NP-Glass system for different times after irradiation; green line –  $\sim 50 \text{ ps}$ , blue line – a few ns.

Figure 3.4 shows the radial temperature distribution in NP-glass system calculated numerically in the limit of the above-described ‘three temperature model’ (3TM) for two different times after irradiation. After  $\approx 50 \text{ ps}$ , i.e., when within a spherical NP

with radius of 15 nm (red disk in Fig. 3.4) an equilibrated high temperature of  $\approx 2000$  K has been established, the temperature of the surrounding glass matrix is still equal to room temperature (green line). It takes a few nanoseconds to establish a heat-affected zone (light magenta circular ring) of the order of 5 nm around the NP by energy dissipation into the glass (blue line).

More details about the first ten nanoseconds of the time evolution of glass temperatures in different distances away from the nanoparticle are given in Fig. 3.5(a). In a distance of 1 nm from the NP surface the glass is heated up to  $T_{\max} \approx 1050$  K within approximately 1 ns after irradiation, then slowly cools down again. With increasing distance of the shells, the maximum temperature decreases and is reached considerably later. For instance, in a distance of the 6 nm a peak value of  $T_{\max} \approx 500$  K is reached only after  $\approx 10$  ns. The further evolution of the heat dissipation is shown by some characteristic radial temperature profiles in Fig. 3.5(b); here the NP is included, i.e.,  $r = 0$  denotes the center of an Ag nanoparticle. At 20 ns the temperatures of nanoparticle and nearest shells are around 450-500 K, while the temperature in a distance 150 nm is still equal to the room temperature. After only 80 ns, however, the total energy is nearly homogeneously distributed and the temperature of the layer containing NPs is  $\approx 330$  K. These calculations have been done for a single metallic nanoparticle of 15 nm radius being surrounded by glass and irradiated by the pulses at 400 nm, with intensities of  $0.5 \text{ TW/cm}^2$ . As an average radius of 150 nm glass surrounding an Ag NP corresponds to an Ag volume fill factor (volume of the silver inclusions per unit volume of the composite material) of  $10^{-3}$ , the presented model calculations should reasonably describe the situation in samples with silver concentration in this range.

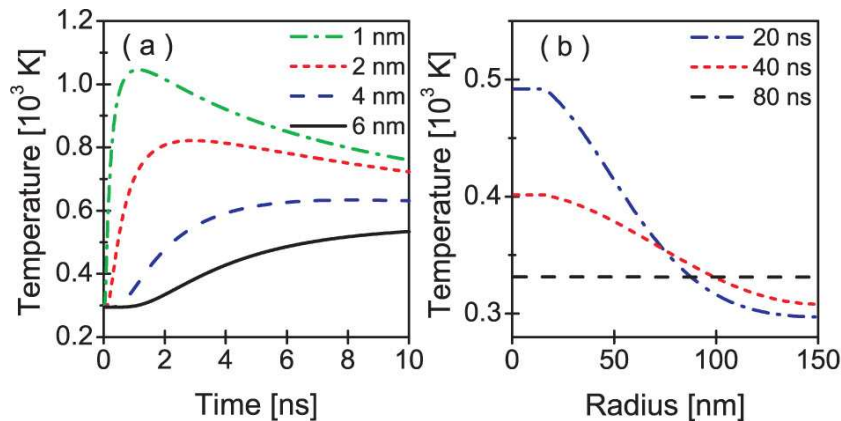


Fig. 3.5. (a) Time evolution of glass temperatures in different shells away from nanoparticle calculated by 3TM. (b) Temperature distribution for longer times (more than 20 ns) after irradiation calculated by 3TM.

Summarizing the above results one can conclude the following: (i) In the first few ns after the laser pulse the temperature of the NPs is above 1000 K, and the matrix temperature in the nearest shell up to a distance of 3 nm from the NP can reach or exceed the glass transition temperature [3.50]; this will cause softening of the glass,

which is needed for NP shape transformation [3.44]. (ii) After  $\approx 80$  ns the system has come to a steady state within the focal volume; from then on heat transfer into the rest of the sample has to be taken into account. It should be mentioned here that this model neglects any glass heating by laser-driven electron and ion emission (which can take place by strong excitation). However, such contributions will only be present within the first few picoseconds after the laser pulse, and will only affect a shell of few nanometers around the NP (it will be shown in Chapter 5). Thus, due to energy conservation the temperature evolution on the time-scale of several nanoseconds or slower discussed here should not be affected by this simplification.

### **3.5. Photoemission from nanoparticles incorporated in dielectric media**

In previous sections the thermophysical processes arising by interaction of the laser pulses with nanocomposites were briefly discussed. This section is devoted to the possible electrophysical processes (such as photoemission of electrons and ions from the nanoparticles), which can take place in strong excitation regime. Therefore, at the first, the basics of the nonlinear ionization will be considered. Then, the following subsection will briefly describe the ionization of silver nanoparticles in glass and effect of surface plasmon on it. The electric field enhancement in the vicinity of the NP will also be discussed. In the last subsection, the attention will be focused on the possible ejection of ions from ionized (therefore positively charged), hot nanoparticle. All these processes can make strong influence on the energy (re-) distribution in NP-Dielectric system, and as it will be shown later, they are very important for the laser-induced nanoparticles shape transformation.

#### *3.5.1. Nonlinear ionization*

Under some circumstances the nonlinear interactions of the electromagnetic wave with matter can lead to permanent structural modifications in it. This, results in considerable changes of the linear and nonlinear optical properties of the exposed material. As used here, the most important mechanism responsible for the permanent modification of matter is the laser assisted ionization.

Ionization of material requires transition of electrons to (above) the vacuum level. The absorption of a photon with energy higher than the ionization energy ( $E_{\text{photon}} \geq E_i$ ) leads to the photoionization of the material, where an electron escapes from atom's potential energy. Such single photon ionization processes can take place independent of the laser intensity (i.e., high photon flux), but of course the degree of ionization will be much higher for high intensities. Therefore, when the laser frequency is high enough, the atomic or bulk properties of the material (such as the dipole moment and absorption) are linearly dependent on the laser intensity. If the photon energy of excitation wave is less than the ionisation energy, the ionization due to single photon absorption is excluded. However, increase of the light intensity leads to enhancement of two-photon absorption in the medium. Thus, ionization of the material can be induced even by intense laser excitation at wavelengths far away

from the fundamental absorption edge due to two-photon (multi-photon) absorption caused by nonlinear processes in the material. One has to distinguish two classes of nonlinear ionization mechanisms: photoionization and avalanche ionization [3.51], which results in plasma formation responsible for nonlinear phenomena and structural modifications in dielectrics.

Photoionization refers to direct excitation of the electrons by the laser field. Moreover, the ionization caused by nonlinear absorption of several photons is described as the multi-photon ionization [Fig. 3.6(a), rot arrows]. On the other hand, increase of the laser intensity refers to growths of the electric field strength of the electro-magnetic wave. In turn, strong electric fields can suppress the Coulomb well of the electron bonded with an atom. If the deformation of the electron potential energy is high enough [Fig. 3.6(b)], the electron tunnels through the short potential barrier and becomes free. This mechanism of photoionization is called the tunnel ionization. These both types of the photoionization depend on material, laser frequency and intensity.

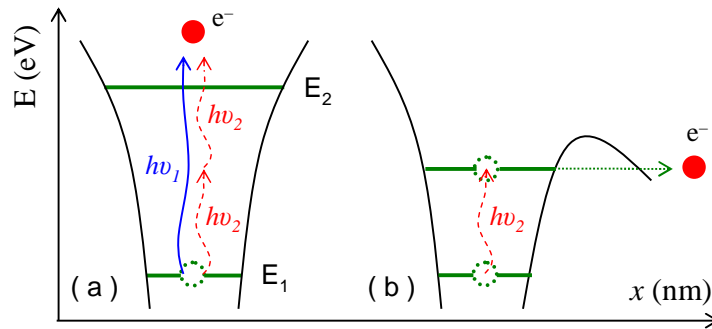


Fig. 3.6. (a) Single photon (with energy  $h\nu_1$ ) and multi-photon (with energy  $h\nu_2$ ) ionization. (b) Sketch showing the possibility of tunnelling ionization. The atomic potential of the atom is deformed by the laser field.

Strong laser interaction with nanoparticles depends on the kinetic energy of the electrons oscillating in the field, and the ionization energy of the nanoparticle atoms. In this context, two parameters are commonly used to characterize the laser interaction with the particle: Ponderomotive energy [3.52] and Keldysh parameter [3.53, 3.54]. Considering an electron in the inhomogeneously oscillating electromagnetic field  $E(t) = E \cdot e^{-i\omega t}$  of the laser, the electron experiences a force that originates from second-order terms of the Lorentz force on the nanoparticle. This is called as the ponderomotive force and given by

$$F_p = -\frac{e^2}{4mc\epsilon_0\omega_L^2} \nabla E^2, \quad (3.10)$$

where  $e$  is the electron charge,  $m$  is the electron mass,  $E$  is the amplitude of the electric field, and  $\omega_L$  is the laser frequency. From the force equation, the ponderomotive energy can be found ( $F = -\nabla U$ ) as

$$U_p = \frac{e^2}{4mc\epsilon_0\omega_L^2} E^2. \quad (3.11)$$

Replacing the E-field amplitude with the laser intensity  $I = (c\epsilon_0/2)E^2$  this energy can be written as follows

$$U_p = \frac{e^2}{2m\omega_L^2} I, \quad (3.12)$$

which describes the cycle-averaged oscillation energy of the electron. As it is seen in Eq. (3.12), the ponderomotive energy is wavelength ( $\lambda = 2\pi c/\omega_L$ ) and intensity dependent. It grows up quadratically with the wavelength and linearly with the intensity. Replacing the  $e$  and  $m$  punitively, it can be given neatly in the form

$$U_p = 9.34 \cdot \lambda^2 [\mu m] I [10^{14} W/cm^2]. \quad (3.13)$$

Having stated the laser frequency (or wavelength) and intensity dependence of the ponderomotive energy, now it is possible to relate this information with the Keldysh parameter  $\gamma$ , which is a practical parameter to distinguish between the tunnel and multi-photon ionisation:

$$\gamma = \sqrt{\frac{E_i}{2U_p}}. \quad (3.14)$$

The Keldysh parameter relates the ionization potential of the atom  $E_i$  to the ponderomotive energy of the electrons. According to the equations (3.13) and (3.14), the Keldysh parameter increases with increasing laser frequency, and when  $\gamma \gg 1$  i.e.  $E_i \gg U_p$ , ionization occurs by multi-photon absorption. When  $\gamma \leq 1$ , field ionization (tunnelling or above barrier) dominates.

The free electrons induced by photoionization result in a broad absorption band and the laser radiation can be absorbed linearly if the plasma density becomes high enough. Indeed, according to the Drude model the electric permittivity of the free electron carrier can be given as

$$\epsilon(\omega) = 1 - \frac{\omega_p^2}{\omega^2 + i\gamma\omega}, \quad (3.15)$$

where  $\omega_p = \sqrt{\frac{Ne^2}{m\epsilon_0}}$  is the plasma frequency,  $N$  is the density of the free electrons and  $m$  is the effective mass of an electron;  $\gamma$  is a damping parameter associated with Drude scattering time. The absorption of a medium depends on imaginary part of the complex electric permittivity and for the free electron plasma it is

$$\epsilon''(\omega) = \frac{\omega_p^2 \gamma}{\omega(\omega^2 + \gamma^2)}. \quad (3.16)$$



It is obvious that absorption of the free carrier increases with growth of the free electron density, which in turn depends on the laser intensity and ionization rate. Further absorption of the laser radiation by the free electrons leads to rapid plasma heating, moving the conduction electrons to the higher energy states. If resulting electrons energy exceeds the bottom of the conduction band by more than the band gap energy between valence and conduction band, the hot free electron can transfer saved energy to an electron in valence band via non-elastic collisions. As an outcome, one receives two electrons in the bottom of conduction band, each of which can be involved in the collisional ionization again. Thus, the electron plasma density grows in this case quickly proportional to exponential function of time [3.51]. This mechanism of ionization is called the avalanche ionization. As it can be seen from the discussion, the avalanche ionization requires some seed electrons in the conduction band, which can be produced by photoionization of impurities and defects in the matrix. For the case of nanocomposites with metallic nanoparticles, electrons, which were emitted from nanoparticle, can seed the avalanche ionisation in surrounding dielectric media.

Further plasma relaxation leads to the energy transfer from the electrons to the lattice (matrix). It has to be pointed out that the energy transfer occurs in time scales much shorter as the thermal diffusion time. Nevertheless, for the laser pulses with duration longer than several tens of ps the energy transfer occurs on time scale of the pulse duration. Then the energy is transported out of the exposed area by thermal diffusion. If the temperature of the irradiate region overcomes the melting or fraction temperature, the damage of the surface can be achieved. In the case of intense fs laser pulses the avalanche ionization leads to the extremely high electron density and energy of the laser pulse effectively deposited in plasma. Only after laser pulse is gone the plasma energy is transferred to the lattice. Since the energy transfer is much faster than the thermal diffusion time, induced ablation by ultra-short laser pulses occurs with minor thermal defects.

### *3.5.2. Surface plasmon assisted emission of electrons from silver nanoparticles embedded in glass*

In the last years the SP assisted photoelectron emission from supported Ag nanoparticles has been extensively studied upon excitation with intense ultrashort laser pulses [3.55, 3.56, 3.57, 3.58, 3.59, 3.60, 3.61, 3.62]. The electron work function from the silver clusters defined as an energy gap between the Fermi level and the energy of the free electron in the vacuum is of about 4.3 eV [3.57, 3.60, 3.63]. Moreover, it was testified that excitation near to the SP resonance extremely enhances the two-photon photoemission yield from the Ag nanoparticles [3.62].

In the composite glass containing metal nanoparticles, probability of the SP assisted photoemission can be strongly affected by a structure of electron energy manifold in the host matrix. In turn, an energy level scheme of the soda-lime glass with embedded Ag nanoparticles can be presented as a junction of the dielectric with a metal (Fig. 3.7). The valence band maximum of the glass lies 10.6 eV below the vacuum level. The lowest energy level of the conduction band in the glass is placed 1.6-1.7 eV below the energy of the free electron in vacuum. Thus, an energy gap

between the Fermi level in the silver inclusion (4.3 eV) and conduction band in the glass is about 2.7 eV and consequently any radiation with photon energy  $>2.7$  eV could evoke a tunnel transition of the electrons from the silver inclusion in to conduction band of the surrounding glass matrix, even by single photon absorption.

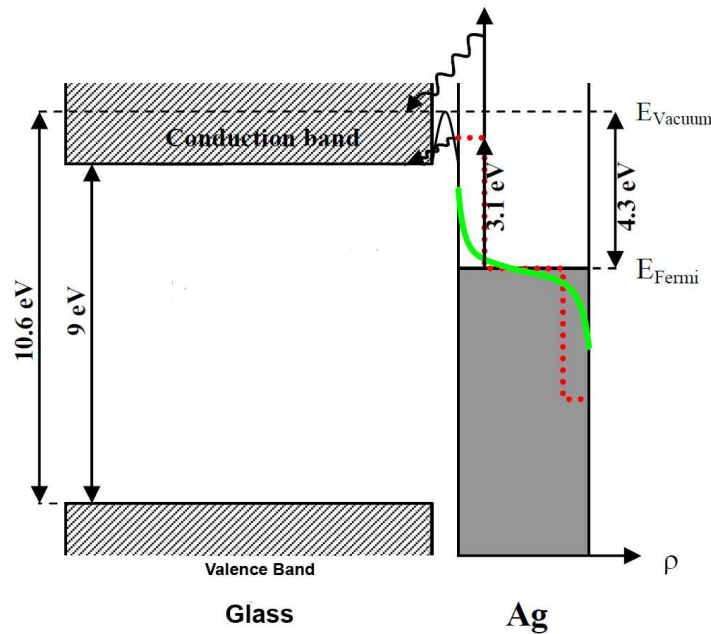


Fig. 3.7 Energy level scheme of the electrons in the composite glass containing silver inclusions. The red dotted line indicates a non-thermal distribution of the electrons in Ag nanoparticle caused by excitation of SP resonance. The green one –distribution of the electrons after thermalization. The Figure is adapted from Ref. 3.64.

Excitation of the Ag nanoparticles near to the SP resonance ( $\sim 3$  eV) by the fs laser at 400 nm (3.1eV) leads to a non-thermal distribution of the electrons in the conduction band of the metal (Fig.3.26, red dotted line). Since the maximal electron energy in this case exceeds the bottom of the conduction band of the matrix in 0.4 eV, the electron injection in the conduction zone of the glass could be possible. At the same time, upon the two-photon plasma excitation, the electrons can overcome the ionization energy level and without any obstacles penetrate into the glass matrix. In turn, the injection of the electrons from metal inclusions into the conduction band of the surrounding matrix is obviously the origin of a rise of conductivity in the composite glass with Ag nanoparticles upon fs laser irradiation near to the SP resonance [3.65].

Electrons being emitted during the laser pulse interaction will be driven by the strong, oscillating electric field and therefore generate an anisotropic distribution of emission directions, obviously given by the electric field oscillations (polarization) of the laser pulse. The anticipated 100 fs pulses at  $\lambda = 400$  nm correspond to 75 full oscillation cycles with mostly very high amplitudes. A simple estimation shows that a conduction band electron of the nanoparticle can gain a linear acceleration of around  $10^{20}$  m/s<sup>2</sup> upon encountering a linear-polarized pulse of 0.3 TW/cm<sup>2</sup> intensity (corresponding to an electric field amplitude of  $10^9$  V/m) within the half plasmon period. This is indeed huge electric field amplitude on the nanoparticle. In the

absence of any damping, the above acceleration can push the electron approximately 0.1 nm away from the nanoparticle surface. However, in the case of SP excitation, the oscillation amplitudes of the surface plasmon waves can overcome the excitation amplitude by typically two orders of magnitude (for silver nanoparticles with  $R \approx 15$  nm) [3.66, 3.67, 3.68]. This leads to a strong enhancement of the local electromagnetic field in the vicinity of the nanoparticle. By excitation with polarized light the E-field enhancement (Fig. 3.8) occurs in special points on the surface. Namely, in the case of spherical nanoparticles, the field is enhanced on the poles of the nanoparticle, depending on the polarization direction of the exciting light. However, in the case of non-spherical particles, it is induced mostly at the tips and corners of the particles [3.63, 3.66, 3.69]. It should be also mentioned here that the local E-field enhancement (EFE) depends on the wavelength (Fig. 3.9); and as it can be seen, in the direction of the laser polarization it has the maximum at longer wavelength than the SP resonance. In the case of non-spherical (spheroids) particles the full spectrum of electric field enhancement factor is shifted to the long wavelength region (Fig. 3.10).

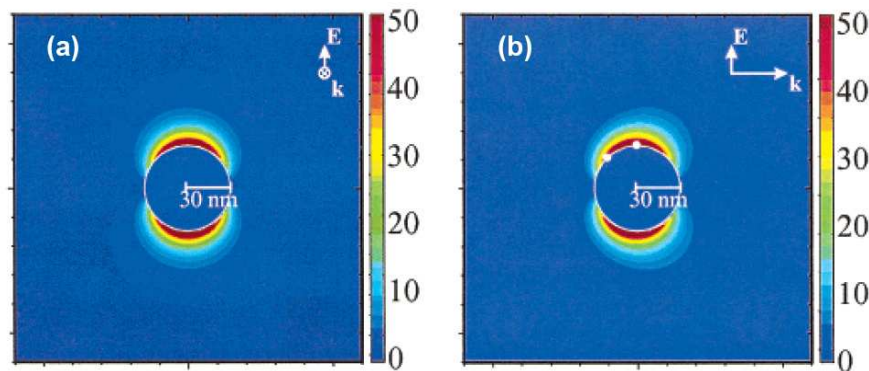


Fig. 3.8. E-field contours for radius 30 nm Ag spheres in a vacuum. Two cross-sections are depicted. (a) The plane containing the propagation and polarization axes and (b) the plane perpendicular to the propagation axis. Labeled points 1 and 2 illustrate locations for Fig. 3.9. The figure is adapted from [3.66].

As a result of the enhanced electric field at the particle-glass interface, the conduction band electron (discussed above) can move away from the nanoparticle surface to approximately 10 nm. Electrons driven so far away from the nanoparticle have left the region of the strongest field enhancement, and will thus experience a weaker backward force due to the reversed field of the next half plasmon period, and may finally be trapped in the glass matrix. These numbers make plausible that under the specified conditions there is a non-negligible probability for emission of even 'cold' electrons. Increase of the electric field in the vicinity of the nanoparticle could strongly suppress energy levels on the metal-dielectric junction and induce effective electron carrier flow from the surface of nanoparticle parallel to the laser polarisation. The anisotropy in this case is determined by anomalous distribution of the local electric field over nanosphere (Fig. 3.8). On the other hand, the electric field in the vicinity of the metal cluster could overcome a breakdown threshold of the glass resulting in the high density electron plasma formation and even ablation of the glass matrix on the poles of the nanosphere.

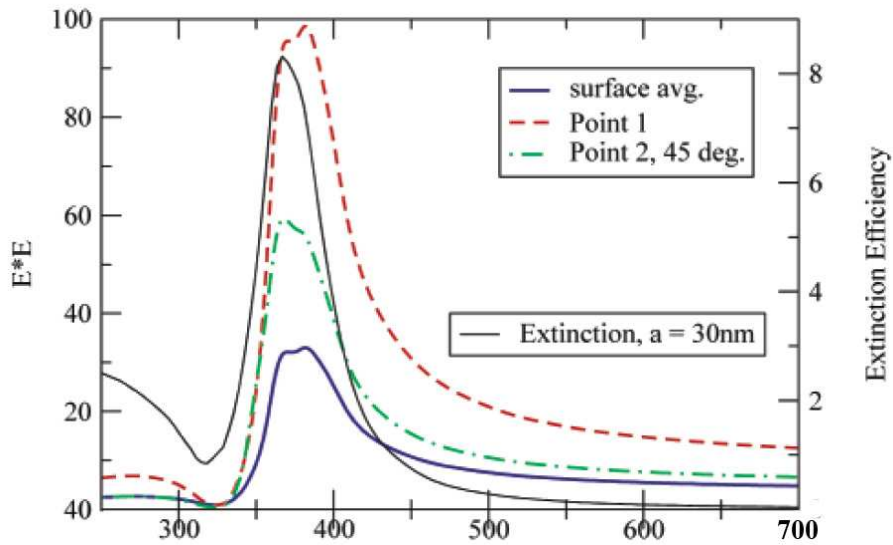


Figure 3.9. Comparison of extinction efficiency, surface-averaged E-field enhancement, and E-field enhancement for specific points for radius 30 Ag spheres in a vacuum. The two points chosen are point 1, along the polarization direction, and point 2, at a 45° angle relative to the polarization direction and in the x-z plane. The figure is adapted from [3.66].

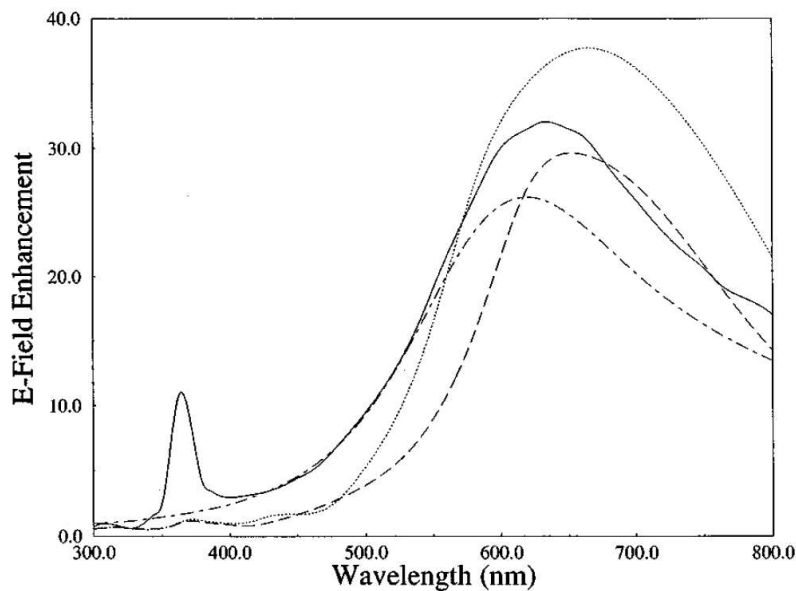


Figure 3.10. Electric field enhancement factor vs wavelength for a prolate spheroid having a major axis of 200 nm and an aspect ratio of 2:1. The results include a T-matrix result (solid), Dipole-Dipole Approximation (DDA) with rough surface (dotted), DDA with exact spheroid surface (dashed), and modified long wavelength approximation (MLWA) (dash-dot). The figure is adapted from [3.70].

Further thermalization of the electrons with characteristic time of a few hundreds of femtoseconds obviously restricts the photoemission processes. However, in the case of strong excitation the energy of some electrons could be high enough to jump in the conduction band of the glass [3.71]. As it was shown above, the maximal electronic temperature after e-e scattering can be higher than  $10^4$  K. The electrons are thermalized to form a hot Fermi distribution (Fig. 3.11, the red solid curve). As it can be seen, the high energy tail of the high  $T_e$  Fermi distribution exceeds the energy needed for nanoparticle electrons to penetrate into the glass conduction band (red area,  $>2.6$  eV). Therefore, even in the time when the pulse is gone, there is a probability of ‘hot’ electron emission. As the directionality of the pulse is no more there, this thermal emission of electrons is isotropic. However, if the pulse is still present, these electrons can be driven by the electric field in direction of laser polarisation.

As a result, irradiation of the silver nanoparticles embedded in glass by the strong laser pulses can lead to two different types of electron emission processes, which could be classified according to their nature of occurrence as ‘pulse-enhanced’ or ‘purely thermal’; the first being anisotropic and the second are isotropic. The isotropic purely thermal electron emissions start after the pulse has gone away and continue to happen as long as the electrons possess high temperatures (few ps). The pulse-enhanced electron emission processes, on the other hand, comprise a ‘direct’ and a ‘pulse-enhanced thermal’ electron emission component. The direct electron emission processes are the fastest that happen within the first few plasmon oscillation periods. The second component of the pulse-enhanced electron emissions is thermal in nature, owing to the increased electron temperatures along the plasmon oscillation directions. Therefore, at the end, when the emitted electrons will be trapped in the conduction band(s) of the glass, the pulse-enhanced ionisation will lead to a non-homogenous electron concentration along the poles of the nanoparticle (along laser polarization), while the purely thermal electron emission homogeneously spreads the electrons in the surroundings of nanoparticle. In next chapter it will be shown that this anisotropic ionisation is one of the most important processes in the laser-induced nanoparticles shapes transformation.

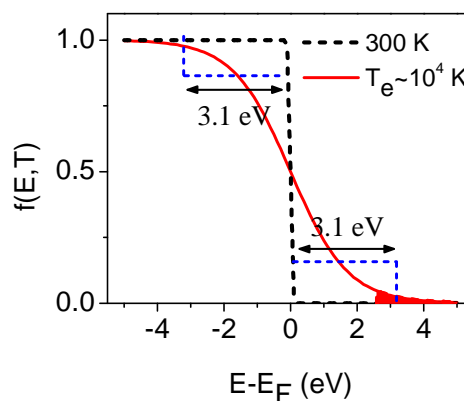


Fig. 3.11. Changes in the Fermi distribution of the electronic system following an ultrashort laser pulse irradiation at an energy of 3.1 eV, which excites electrons below the Fermi level to high energies (represented by the arrows). The resulting hot electronic distribution is shown with the solid curve.

### 3.5.3. Emission of ions (small clusters) from nanoparticle

As one can expect, the ionisation of nanoparticles leads to a redistribution of the charges in NP-Glass system. The nanoparticle gets positively-charged (due to the emitted electrons) and hot over time (due to e-ph scattering, Chapter. 3.3 ). Therefore it becomes unstable electrically and thermally. So it is obvious that after a few picoseconds electric potential and thermal energy can overcome the binding energy of Ag ions, which are being emitted into the surrounding glass matrix [3.10, 3.72, 3.73]. Experimentally, Podlipensky *et al.* [3.73] show by luminescence study the presence of Ag ions in the glass matrix emitted upon femtosecond laser irradiation. Additionally, by transmission electron microscopy (TEM) of the glasses with silver nanoparticles irradiated by fs laser pulses it was observed that this ion emission leads to partial dissolution of the nanoparticles, creating small Ag aggregates around the remaining nanoparticle [3.74, 3.75].

The physical concept behind these ion emission processes is mainly the so called Coulomb explosion [3.72], which is a direct consequence of the nanoparticle charging. The repulsive Coulomb forces among the accumulated charges lead to the dissolution (destruction) of the nanoparticle. Even extreme cases of nanoparticle dissolution mechanisms were observed for nanoparticles in aqueous medium [3.8], where not only the ions but also some small fragments could leave the nanoparticle because of the soft surrounding. Nevertheless, independent of the way it happens, the total volume of the nanoparticle is reduced over time due to material ejections.

It is obvious that this process of ion ejection will also lead to the changes in energy relaxation (temperature distribution) in NP-Glass system. Some part of the energy will be taken from the nanoparticle and, via kinetic energy of the ions, be transferred to the glass when the ions are trapped there.

In the following these isotropically emitted ions can meet the already trapped electrons (result of NPs ionisation) and annihilate (recombine) with them to the atoms (or small silver clusters), which are seen in the TEM images [3.74, 3.75].

The experimental observations and analysis regarding these electron and ion emission processes, and how they lead to the NP shape transformation will be presented and discussed in the following chapters.

## Chapter 4. Experimental technique

In the following sections the laser systems, samples, irradiation as well as spectroscopic techniques used in this work will be briefly discussed.

Irradiation of the samples was done with the commercial laser systems produced by “Spectra Physics”, “Light Conversion Ltd.” as well as by Non-collinear Optical Parametric Amplifier from “Jobin Yvon GmbH”. The usage of these systems gave the possibility to excite the nanoparticles embedded in glass by the strong fs pulses in a broad spectral range.

The samples for experiments prepared as intermediate product for manufacturing of broadband polarizers were provided by CODIXX AG [4.1].

Transmission Electron Microscopy (TEM) and Scanning Electron Microscopy (SEM) of original and modified samples was performed by Dr. H. Hofmeister (Max-Planck-Institute of Microstructure Physics, Halle), Dr. P. Miclea (MLU Halle) and Mr. F.Syrowatka (IWZ Materialwissenschaft, Halle).

### 4.1. Preparation and characterization of glass samples containing silver nanoparticles

In this work the nanocomposites with silver nanoparticles are studied. In turn, samples containing silver clusters were prepared by Ag-Na ion exchange method with following annealing in reduction atmosphere. Modification of ion exchange and reduction conditions (annealing time, temperature and etc.) strongly affects size and distribution of silver nanoparticles in the glass substrate.

The samples were prepared from soda-lime float glass (72.5 SiO<sub>2</sub>, 14.4 Na<sub>2</sub>O, 0.7 K<sub>2</sub>O, 6.1 CaO, 4.0 MgO, 1.5 Al<sub>2</sub>O<sub>3</sub>, 0.1 Fe<sub>2</sub>O<sub>3</sub>, 0.1 MnO, 0.4 SO<sub>3</sub> in wt%) by Ag<sup>+</sup>-Na<sup>+</sup> ion exchange. For the ion exchange process glass substrate is placed in a mixed melt of AgNO<sub>3</sub> and KNO<sub>3</sub> at 400°C [4.2, 4.3]. The thickness of the glass substrate, time of the ion exchange process and weight concentration of AgNO<sub>3</sub> in the melt determine the concentration and distribution of Ag<sup>+</sup> ions in the glass. Following thermal annealing of the ion exchanged glass in H<sub>2</sub> reduction atmosphere, typically at 400-450°C, results in the formation of spherical silver NPs [4.2]. As could be expected, size and distribution of Ag nanoparticles in the depth of the glass sample depend strongly on temperature and time of Na-Ag ion exchange as well as on the annealing time. In our case, the spherical Ag nanoparticles of 30-40 nm mean diameter [Fig. 4.1(a)] are distributed in a thin surface layer of approximately 6 μm

thickness (total thickness of glass plate 1 mm). The fill factor  $f$  of Ag NPs is defined as volume of the inclusions per unit volume of the composite material ( $f=V_{Ag}/V_{total}$ ).

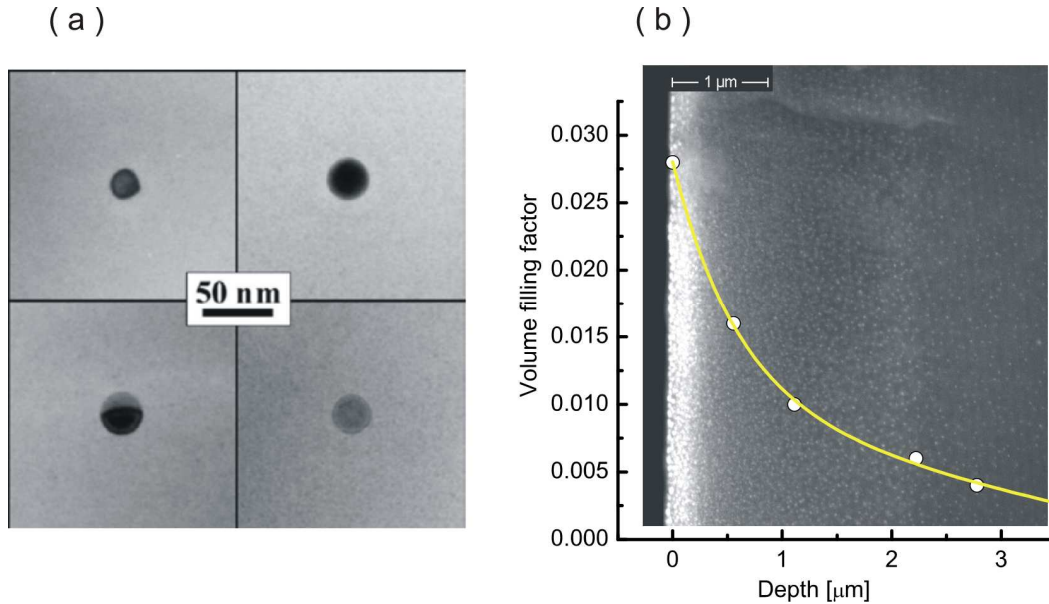


Figure 4.1. (a) TEM picture of typical spherical silver nanoparticles in nanocomposite glass. (b) SEM picture of the cross section of glass sample containing spherical silver nanoparticles (Ag particles are reproduced as white spots). The gradient of the volume filling factor of Ag nanoparticles is shown in superimposition (The x-axis was adjusted to the length scale of the picture).

Figure 4.1(b) shows the SEM picture of the cross section of the sample, where silver particles are reproduced as white spots. To obtain an information about the distribution of silver NPs in the depth of the glass, surface layers of various thicknesses from the sample were removed by etching in 12% HF acid for different retention times. After this procedure SEM images were recorded for all etched surfaces [examples given in Fig. 4.2(a), increasing etching time from (i) to (iv)], as well as optical transmission spectra [see Fig. 4.2(b)]. The area fraction of silver derived from the SEM pictures was then converted to a volume fill factor assuming a typical electron penetration depth of 500 nm. The result is given as superimposed curve in Fig. 4.1(b), showing the highest silver content of  $f = 0.028$  directly below the glass surface. Within a few micrometers the fill factor then decreases strongly with increasing distance from the surface.

Figure 4.2(b) depicts the corresponding transmission spectra with the same lettering as in Fig. 4.2(a). However, it should be noticed that the optical spectra integrate over the whole particle-containing layer. Thus, for the original sample the absorption around SP resonance is very high, discouraging any detailed analysis of the spectral band shape. The same holds for absorption after the shortest etching time [Fig. 4.2(a), curve (i)]; however at least, one can estimate for this case an extinction peak wavelength in the range of 420-440 nm. Further etching of the sample results in fading of the absorption band caused by the decrease of thickness of the silver-



containing layer. Additionally, spectrum (i) indicates that the upper most metal-rich layers are responsible for a shift of the red wing of the SP band towards longer wavelengths.

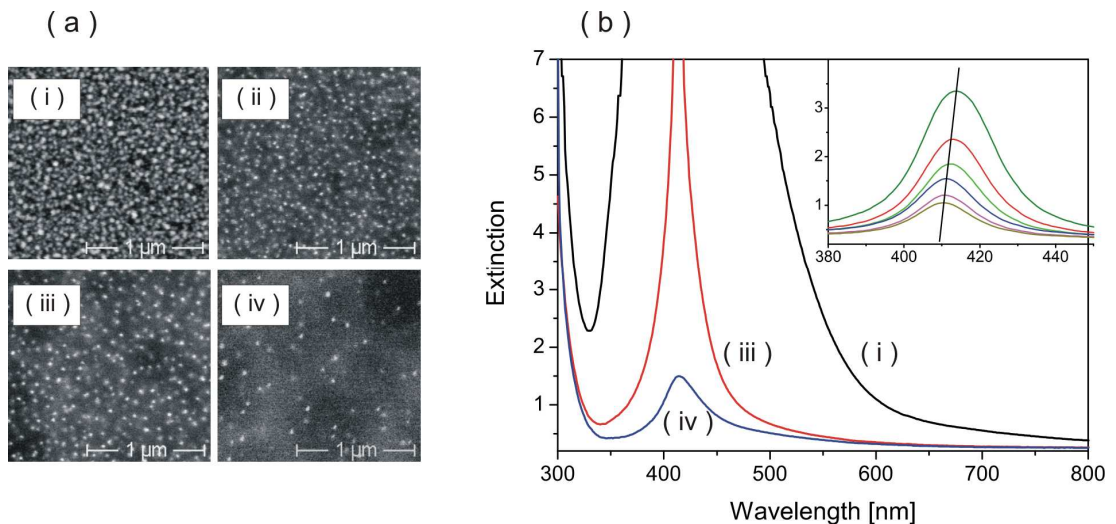


Fig. 4.2. (a) SEM pictures of etched samples with Ag nanoparticles (volume fill factor: i – 0.01; ii – 0.006; iii – 0.004; iv – 0.001). (b) Extinction spectra of samples with spherical silver nanoparticles after different time of etching in 12% HF acid. Lettering of the spectra is according to the SEM pictures shown in Fig. 4.2(a). The samples with lower fill factor have higher transmission.

For samples etched for longer times resulting in maximum residual filling factor of less than 0.004, the evolution of the spectra with etching time is shown in more detail in the inset of Fig. 4.2(b). It is seen that decrease of fill factor (longer time of etching) leads to a slight shift of the SP band maxima to shorter wavelengths. This is well compatible with the Maxwell–Garnett theory (Chapter 2.2), which predicts a red-shift of the SP band for the samples with higher fill factors [4.4, 4.5, 4.6].

It should be mentioned here that for the study of photomodification shape transformation of single nanoparticles presented in the Chapter 5 the etched samples with the fill factor of  $10^{-3}$  were used. However, the experiments presented in Chapter 6 were performed on the samples with high filling factor ( $f \sim 0.01$ ).

## 4.2. Laser systems used for nanoparticles' shape transformation

The experiments presented in this work were mainly carried out using a commercial system of mode-locked Ti-sapphire laser with regenerative amplification produced by “Spectra Physics”. The laser system is schematically shown in Fig. 4.3. The main part of the system consists of the mode-locked Ti:sapphire oscillator “Tsunami” pumped by 5W cw diode-pumped Nd:YVO<sub>4</sub> laser with intercavity doubling at 532 nm. The Ti:Sa has been known as an active media since 80<sup>th</sup> when Moulton demonstrated for the first time the pulse [4.7, 4.8] and cw laser generation [4.9].

The broad amplification band [4.10] allows to achieve in mode-locked operation, pulses as short as ~5 fs [4.11, 4.12, 4.13, 4.14, 4.15] that makes Ti:Sa lasers the most common and commercially available tunable solid-state lasers. In this work, mode-locked Ti:sapphire laser with pulse duration of 80 fs and energy of up to 12 nJ, repetition rate of 82 MHz, tuning range of 720-840 nm was used. The tuning range was only restricted due to set of selective dielectric mirrors used in the laser cavity.

In order to increase the pulse energy from oscillator up to 1 mJ the *regenerative amplifier* “Spitfire” was used. The working principle of the amplifier is based on chirped pulse amplification [4.16]. The regenerative amplifier consists of three parts: namely the stretcher, the amplifier and the compressor. First of all, the seed pulses from the oscillator are stretched in time to ensure a safe amplification process. In other words, the stretching of the pulses decreases the peak pulse intensity and prevents a damage of the laser crystal. Then, these pulses are amplified in the amplifier cavity. An intense pump pulse produces the high population inversion in the laser crystal. Then a seed pulse coming in the system stimulates the electron transitions from the upper laser level, takes off the population inversion and induces stimulated emission. Therefore, whole energy emerged by electron transitions is deposited in the seed pulse. In “Spitfire” in order to enhance the amplification efficiency the seed pulse makes approximately 20 passes through the Ti:sapphire crystal placed in the cavity. In turn, the “Spitfire” was pumped at 527 nm by Q-switched Nd:YLF intercavity doubled laser with pulse energy of 10 mJ, pulse width about of 200 ns and repetition rate 1 kHz. After amplification pulse is compressed again. Stretching and compression were performed using a system of two gratings and mirrors. Such technique allows to obtain pulses with duration of about 150 fs, energy up to 1 mJ (peak power ~6 GW) and pulse repetition rate of 1 kHz.

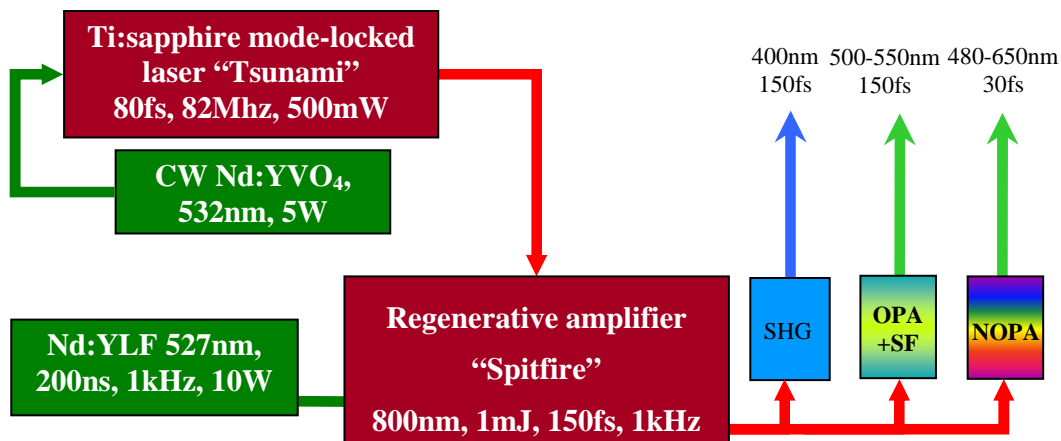


Fig. 4.3. The scheme of the main laser system used in this work. SHG – Second Harmonic Generation; OPA – Optical Parametric Amplifier, namely - Travelling-wave Optical Parametric Amplifier of Superfluorescence (TOPAS); SF – Sum Frequencies Generation; NOPA – Noncollinear Optical Parametric Amplifier.

Using the nonlinear frequency conversion of intense laser pulses derived from Ti:sapphire system the radiation with wavelengths in the spectral range from UV to IR can be achieved.

First, using *second harmonic generation* (SHG) in Type-I Beta Barium Borate (BBO) crystal with 0.5 mm thickness the high energy infrared pulses (centered at  $\lambda = 800$  nm with  $\Delta\lambda \sim 20$  nm) were transformed to the pulses with wavelengths of 380-420 nm and pulse duration of 150 fs.

On other hand, using *optical parametric generation* [as an example 4.17] in BBO crystal [Travelling-wave Optical Parametric Amplifier of Superfluorescence (TOPAS)] by pumping with pulses at 800 nm from Ti:sapphire system the radiation in the spectral range 1.2-1.6  $\mu$ m (signal) and 1.6-2.4  $\mu$ m (idler) was obtained. Following summation of the signal and fundamental (800 nm) frequencies in BBO Type-II crystal allowed to produce the 150 fs pulses tunable in 490-560 nm spectral range.

Additionally, to obtain the pulses in the visible spectral range (470-700 nm) with the shorter pulse duration (around 30 fs), the *Noncollinear Optical Parametric Amplifier* (NOPA) [4.18] was used.

For experiments related to the study of the influence of laser repetition rate on the NP shape transformation, the second harmonic of an Yb:KGW laser (“Pharos”) operating at 1030 nm and generating 300 fs pulses with the repetition frequency of 50-350 kHz was used.

As a result, the usage of above described systems gave the possibility to excite the nanoparticles embedded in glass by the strong fs pulses in a broad spectral range.

To characterize the pulses, a “home-made” Self Diffraction FROG system [basic theory of FROG can be found in Ref. 4.19, 4.20, 4.21] was used. As an example, Fig. 4.4. shows the SD-FROG traces measured from NOPA.

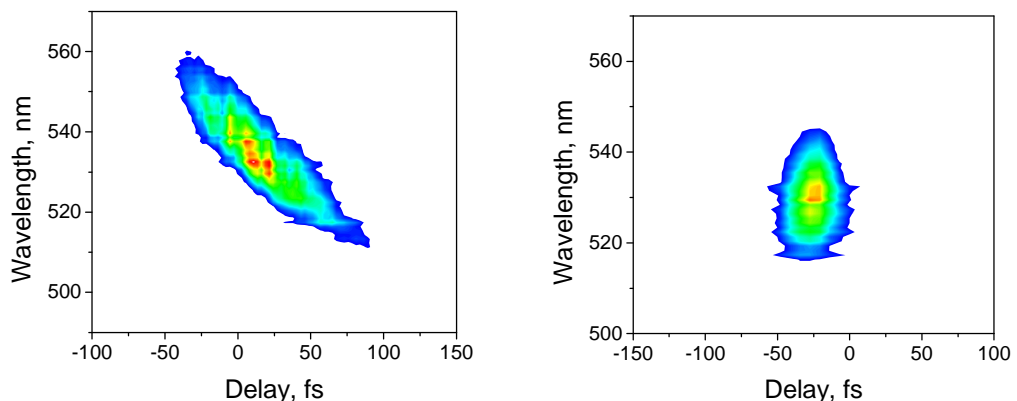


Fig. 4.4. SD-FROG traces of the pulses from NOPA: a) uncompressed pulses at  $\lambda = 535$  nm (pulse duration  $\tau=150$  fs); b) compressed pulses at  $\lambda = 528$  nm ( $\tau=33$  fs).

### 4.3. Irradiation technique

To investigate the laser-induced modifications of Ag nanoparticles embedded in soda-lime glass the laser beam was focused by the lens or objective on the sample placed on the X-Y translation stage driven by computer. The focus of the lens, beam width, writing density (actually pulse number per spot area), as well as wavelength and intensity of the laser pulses have been chosen according to the goals of the experiments. The irradiation was performed in two different modes that allowed to obtain small (few hundred  $\mu\text{m}$ ), separate, single spots on the sample with modified NPs (Fig. 4.5, top-left), as well as the big areas (few mm) which can be seen in Fig. 4.5, top-right). In the first case, X-Y translation stage is not used during irradiation, while to get the big areas, the sample has to be continuously moved as it is shown in Fig. 4.5 (bottom part), so that the squares are written line by line. The vertical distance between horizontal lines have to be chosen so that the lines are overlapped making the square areas homogeneously modified. In such mode, the velocity of the translation stage defines the number of applied pulses. The high velocity results in almost isolated spots (Fig. 4.5, SS), while slower sample movement leads to an overlap of the pulses in space (Fig. 4.5, MS).

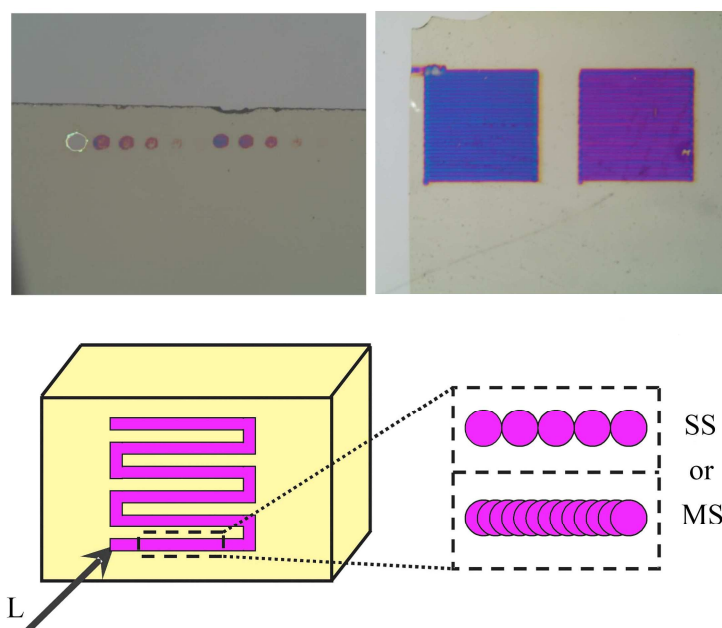


Fig. 4.5. (top) – irradiated by fs laser spots (left), fields (right) on the sample containing Ag nanoparticles; (bottom) – the schemes of the fields irradiation.

### 4.4. Temperature dependent irradiation

To study the effect of temperature on the laser-induced nanoparticles shape transformation, an experiment with pre-heating/cooling of the sample was employed. For this investigation the sample was placed in the vacuum chamber with a heat-sink which can be electrically heated. Cooling of the sample was possible by help of

liquid nitrogen. The temperature  $T$  was controlled by a thermocouple connected to the heat-sink; and was varied between  $-100$  and  $+200^{\circ}\text{C}$ . The vacuum chamber was mounted on a motorized X-Y translation stage and, as it was described above, moved continuously so that square areas of  $1.5 \times 1.5 \text{ mm}^2$  size were written line by line.

#### 4.5. Spectroscopic technique

As it was mentioned above and will be shown in the next chapters, irradiation of glass samples containing Ag nanoparticles by fs laser pulses leads to the modifications of the NPs shape as well as surrounding matrix. These permanent laser induced modifications result in changes of spectral properties of the composite glass with silver nanoparticles. Thus, analyzing the obtained optical spectra, it is possible to characterize the transformations occurring in the sample.

In this work, the transmission spectra measurements were done using several spectrometers (setups). Two beams transmission spectrometer Shimadzu UV-3100 operating in spectral range of 200-1500 nm was used to measure the transmission spectra from the sample area with size more than  $1 \times 1 \text{ mm}^2$ . To polarize the light in spectrometer and thereby measure the polarized transmission spectra, a Glan prisms placed in the spectrometer were employed. In turn, the investigation of the optical changes for smaller areas was done by MSP 400 microscope spectrometer. This spectrometer allows to measure the spectra with  $1 \text{ }\mu\text{m}$  spatial resolution.

#### 4.6. Technique used for investigation of intensity dependence

To study intensity dependences of Ag nanoparticle shape transformation a setup for position resolved transmission spectra measurements (which was proposed by A. Podlipensky [4.22]) has been built [Fig. 4.6 (a)]. In this experiment, the sample was irradiated by the laser beam, which was focused in a single spot of the size of  $\sim 200 \text{ }\mu\text{m}$ . By help of the measured, approximately Gaussian intensity distribution of the laser beam, any position within an irradiated spot can be rescaled to the intensity applied in that place. The principle is shown in Fig. 4.6(b), giving on the left-hand side a projection of the spectrometer entrance slit (rectangle) on the modified spot. Lenses L2 and L3 were chosen so, that the slit width of  $100 \text{ }\mu\text{m}$  was small compared to the size of the (enlarged) spot image, and spectral changes in horizontal direction within the slit are negligible. Since wavelength dispersion is done in the horizontal plane, the (vertical) position in the slit can thus be correlated to the laser beam intensity in the same position [right-hand side of Fig. 4.6(b)]. Recording the transmitted light with a CCD camera in the focal plane of the polychromator, intensity-dependent spectra are obtained simultaneously. The spectrometer (ISP) was a Jobin Yvon imaging spectrograph CP140 coupled with a CCD (TE/CCD-1024-EM/EEV30-11/UV from Roper Scientific). The modified areas on the sample were illuminated by a broadband light source (LS). In order to measure polarized transmission spectra, a polarizing prism P was used. Fig. 4.7 shows an example of the images obtained on CCD for different polarizations. In order to calibrate the

image in real sizes the micro scale with scaling factor of  $50\ \mu\text{m}$  was employed. For the wavelength calibration of the spectrometer a Hg-Cd spectral lamp was used.

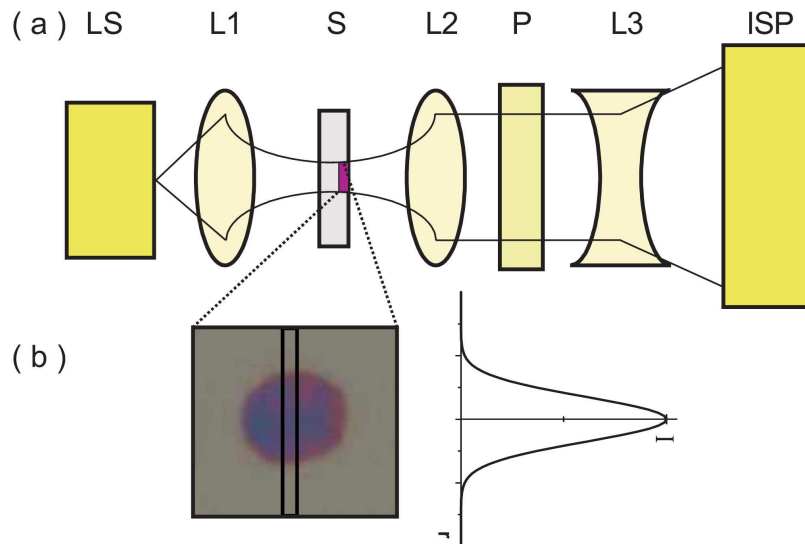


Fig. 4.6. (a) The scheme of the setup for the measurements of spatially resolved transmission spectra. LS – light source, L1, L2, L3 – lenses, S – sample, P – polarizer, ISP – imaging spectrometer; (b) Enlarged image of modified area and Gaussian intensity profile of the laser beam.

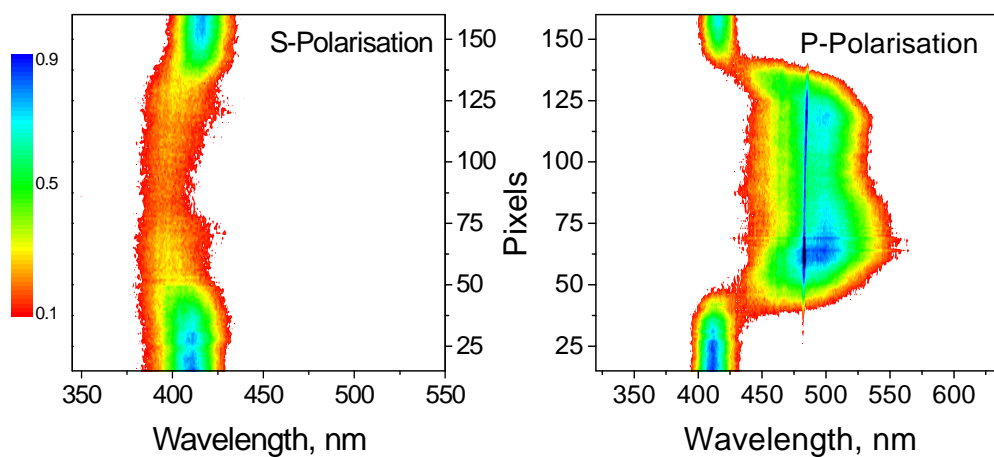


Fig. 4.7. Position (intensity) resolved polarized transmission spectra of silver nanoparticles embedded in glass, which were irradiated by fs laser pulses.

#### 4.7. Technique used for optical determination of NPs shape

To determine 3D shape of nanoparticles one can think that the simplest way is just to look on this NP from all three directions by the eyes [for nanoscale it is of course possible using transmission electron microscopy (TEM)]. However, for the samples used in this work the preparation for TEM is very complicated and the side view TEM is almost impossible, because the sample has only 2  $\mu\text{m}$  thick layer containing nanoparticles from the edge. On the other hand, the solution can be found through the usage of the optical transmission spectra measured from all directions. As it was discussed in Chapter 2.1, the optical properties of nanocomposites with metallic nanoparticles depend on the shape of the latter. It was shown that if the nanoparticles have non-spherical shape, then an optical dichroism appears. Moreover, if the NPs have a spheroidal shape, the spectral gap between polarized extinction spectra is strongly correlated with the aspect ratio of these spheroids. Therefore, carefully analysing the optical transmission spectra measured from three directions, it is possible to determine the shape of nanoparticles.

In this work, in order to determine the 3D shape of nanoparticles after irradiation by fs laser pulses the following procedure was used: The laser beam was propagated in z-direction [Fig. 4.8(a)], and focused on the sample with a spot size of about 200  $\mu\text{m}$ . Moving the sample continuously on a motorized X-Y translation stage (as it was described in Section 4.3),  $3 \times 3 \text{ mm}^2$  areas were written line by line. For the linear polarized pulses two squares with identical irradiation parameters, but different laser polarization  $L_x$  and  $L_y$  (along x and y axes) were produced.

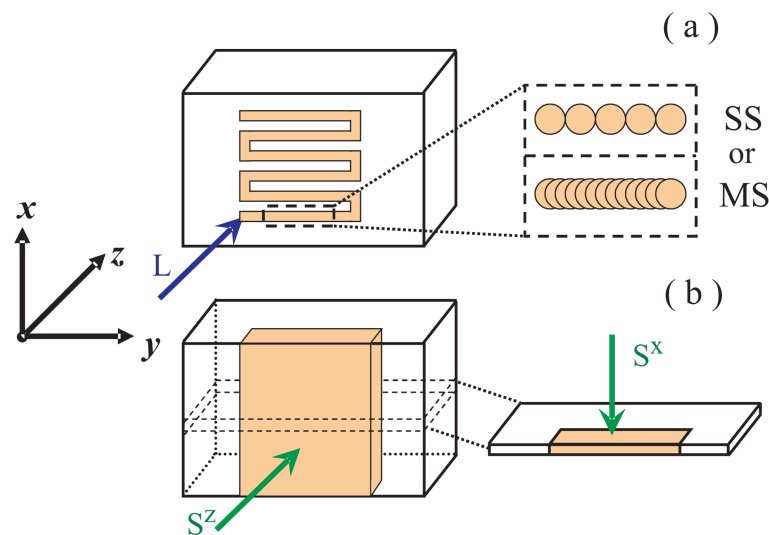


Fig. 4.8. The schemes of experiment: a) geometry of irradiation; b) geometry of transmission spectra measurements.

Then, optical transmission spectra of all irradiated areas were recorded twice, namely with probe light in the direction of the fs laser beam and perpendicular to it. For the later case a thin slice (thickness  $\approx 20 \mu\text{m}$ ) was cut from the sample, as sketched in Fig. 4.8(b), and polished. The spectra were measured with a MSP 400 microscope

spectrometer. The geometry, polarization directions of laser irradiation and recording of transmission spectra will be described later by a notation referring to the coordinate system given in Fig. 4.8. As the ultrashort laser pulses were always propagated in z-direction, we need only one subscript to specify the (linear) laser polarization by  $L_x$  or  $L_y$ , respectively. The optical spectroscopy is described by a two index notation where the subscript defines the polarization direction and the superscript the propagation direction of the probe light. For instance,  $s_y^z$  means y-polarized probe light propagating in z-direction. Over all, by irradiating pairs of areas with orthogonal polarization ( $L_x$  and  $L_y$ ), we gain access to 3 orthogonal projections of the transformed particles, which allows the complete optical analysis of the 3D particle shape (symmetry).



## **Chapter 5. Laser induced shape transformation of Ag nanoparticles embedded in soda-lime glass**

Nowadays the optical properties and structure of numerous solids can readily be modified by making use of vastly different laser sources. In this context irradiation of dielectrics containing metallic nanoparticles (NPs) by pulsed lasers has opened up a promising route towards designing nanocomposite materials with special properties tailored for various applications [5.1, 5.2, 5.3]. The optical properties of such materials are determined by the surface plasmon (SP) resonance of the metal clusters. For a given application, these SP resonances can be tuned within a wide spectral range from visible to near infrared, by correct choice of electronic properties of metal clusters and dielectric matrix. Furthermore, the SP band also strongly depends on size, shape, concentration and distribution of the nanoparticles [5.4, 5.5]. Thus, the laser-induced techniques to modify size, shape and arrangement of the metal clusters [5.6, 5.7, 5.8, 5.9, 5.10, 5.11, 5.12, 5.13, 5.14] provide a very powerful and flexible tool to control and optimize the linear and nonlinear optical properties of metallodielectric composites.

Recently, it was discovered that a permanent transformation of initially spherical metal nanoparticles embedded in soda-lime glass into ellipsoidal (or more general, non-spherical) shapes can be made by irradiation with intense fs laser pulses near to the SP resonance [5.10 - 5.14]. Moreover, the dichroism in the spectra was strongly connected to the laser polarisation and inversely changed by irradiation in “single-short” and “multi-short” regimes [5.14]. However, the mechanism responsible for the anisotropic shape transformations of the spherical Ag nanoparticles seems to be very complicated and still needs detailed investigations.

In this chapter the attention will be focused on the study of processes arising by interactions of intense fs laser pulses with spherical Ag nanoparticles in soda-lime glass and leading to anisotropic shape transformation of the last ones. First, the 3D shape of nanoparticles after laser-induced transformation will be optically analysed. The experimental results presented in this chapter also include the studies of polarization and intensity dependences of laser induced shape transformations of the silver nanoparticles, effect of the excitation wavelength, writing density and the temperature on the laser induced dichroism. Limiting factors of laser-induced NPs shape modification, as well as a technique of irradiation, which prevents the destruction of nanoparticles and leads to increase of the NPs elongation will be discussed too.

## 5.1 Influence of the laser polarization, pulse intensity and number of pulses applied on nanoparticles' shape

As it was mentioned above, the former investigations performed by M. Kaempfe, A. Podlipensky *et al.* [5.10-5.14] demonstrate a dichroism in composite glass with initially spherical Ag nanoparticles induced by irradiation with intense, linearly polarized fs laser pulses at wavelengths near to the SP resonance. Moreover, single-shot (high intensity) and multi-shot (low intensity) irradiations resulted in an inversion of the dichroism in extinction spectra. However, after irradiation of NPs by the pulses with circular polarization, no dichroism was observed [5.11].

To understand the reason of this dichroism inversion (and absence), first in this section, the shapes of laser-transformed nanoparticles will be investigated for each type of irradiation.

In the second subsection, effect of the laser pulse intensity, pulse writing density on the laser-induced dichroism (NPs shape modification) in soda-lime glass containing spherical Ag nanoparticles will be consider. The results presented there will help in understanding comprehensive picture of the physical processes behind the laser-induced shape transformation. In particular, the following questions will be answered: (i) Is there a single pulse intensity threshold for deformation, or can lower intensity be compensated by irradiating more pulses? (ii) At which intensity / number of pulses applied does the transition from prolate to oblate shape occur, and which particle shapes are produced there? (iii) What happens with the particles going to very high irradiation intensity and / or large number of pulses applied to one spot?

### 5.1.1. Optical 3D shape analysis of nanoparticles after laser induced deformation

The method used for nanoparticles 3D shape determination was described in details in Chapter 4.7. The geometries of irradiation and transmission spectra measurements are assigned by the  $L$  and  $S$  notations, respectively; ( $S_y^z$  means y-polarized probe light propagating in z-direction).

#### Shape of nanoparticles after irradiation by linearly polarized pulses

As it was mentioned above, an ultra-short laser pulses can transform initially spherical silver nanoparticles embedded in soda-lime glass into non-spherical shape. Macroscopically, this effect is observed as optical dichroism. The principal axes of this dichroism depend on the laser polarization and on the irradiation conditions: using a series of pulses of relatively low intensity (only slightly above threshold for shape transformation), a red-shifted SP band is observed with light polarized parallel to the fs laser [Fig. 5.1(b)], whereas for single laser shots at higher intensity the dichroism is reversed [Fig. 5.1(a)]. This observation corresponds well to the particle shapes found by TEM. As shown in Fig. 5.1(c-d), we find elliptical central particles (surrounded by a more or less pronounced halo of small particles) oriented with their major axis along the laser polarization at lower intensity [Fig. 5.1(d)], and orthogonal

to it at higher intensity [Fig. 5.1(c)]. Both optical spectra and TEM images, however, do only give information about a projection of the particle shapes in a plane orthogonal to the observation direction. So the real shapes of transformed particles in 3D space could be either prolate or oblate spheroids, or even other shapes without an axis of symmetry are possible.

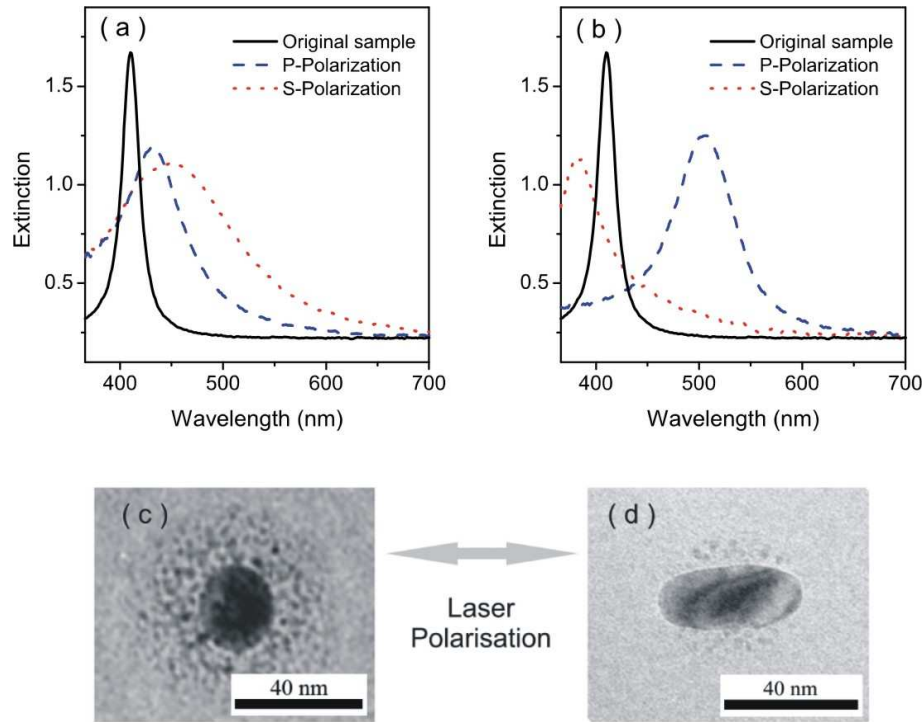


Fig. 5.1. Polarized extinction spectra of original and irradiated samples, and TEM images of deformed nanoparticles: a) single shot regime,  $I_p = 3 \text{ TW/cm}^2$ ; b) multi-shot regime (1000 pulses per spot), peak pulse intensity  $I_p = 0.6 \text{ TW/cm}^2$ ; c) TEM image of nanoparticle irradiated in single-shot regime; d) TEM image of nanoparticle irradiated in multi-shot regime.

To determine the 3D shape one has to compare the optical transmission spectra measured from all three directions. We start the discussion by comparing pairs of spectra  $S^z$  obtained normal to the original surface. The transmission spectra, being similar to ones shown in Fig. 5.1(a-b), are given for multi-shot (left-hand side of Fig. 5.2) or single-shot regime (right-hand side of Fig. 5.2). As expected, spectra referring to the same irradiation conditions are almost identical, except for the reversed dichroism (e.g.  $L_x S_x^z = L_y S_y^z$  and  $L_x S_y^z = L_y S_x^z$ ). The explanation for the dichroism is the anisotropic shape of the silver clusters: as the projection in the x-y plane is approximately an ellipse [Fig. 5.1(c-d)], the spectral separation of the observed SP resonances is correlated with the aspect ratio of the particles, the stronger red-shifted band being associated with the major axis [5.15]. So it is obvious that, qualitatively, nanoparticles irradiated in multi-shot mode are more elongated than in the single-shot regime.

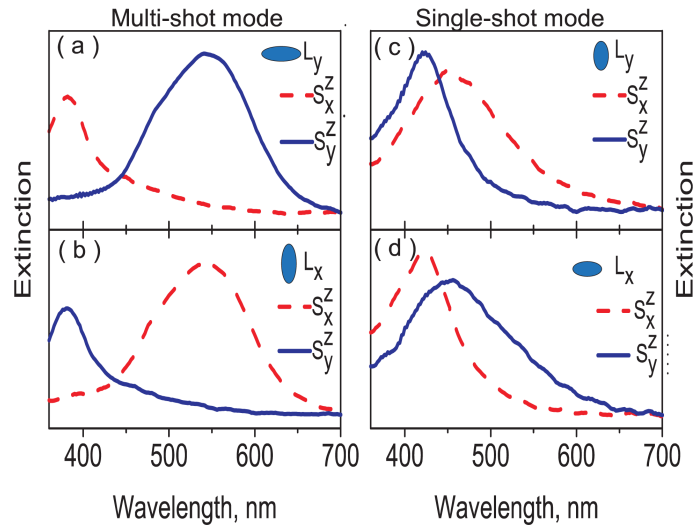


Fig. 5.2. Polarized extinction spectra  $S^c$ . The projection of nanoparticles shape on  $x$ - $y$  plane is schematically shown in inset.

A detailed discussion about the shape of the particles is possible by looking at the third axis. The corresponding spectra  $S^x$  are given in Fig. 5.3. Again the pairs of areas irradiated with different laser polarization  $L_x$  or  $L_y$  are given on the left (right)-hand side for multi- and single-shot regime, respectively. As the spectra in Fig. 5.2(a) and Fig. 5.3(a) are almost identical, and in Fig. 5.3(b) no dichroism is seen ( $S_y^x \approx S_z^x$ ), it is obvious that the particles have a rotational symmetry. More specifically, the spectra clearly indicate that in multi-shot mode prolate spheroids are created with their major (symmetry) axis along the laser polarization [Fig. 5.4(a, b)]. A comparison of the spectra in Fig. 5.2(c), 5.3(c) and 5.3(d) leads to a similar conclusion for the single-shot regime: again a rotational symmetry axis along the laser polarization is proven, while the reversed dichroism (see Fig. 5.2) indicates that for high intensities oblate spheroids are produced [Fig. 5.4(c, d)].

Having elucidated the symmetry and principal shape of the transformed particles, we can now try to get information about the aspect ratio of the particles by a more detailed analysis of the spectra.

If one assumes that the volume of nanoparticles remains constant during shape change, then after transformation into oblate or prolate spheroids the minor axis should be smaller than the radius of initially spherical particles. Theoretical calculations for spheroids [5.15, 5.16] show that in this case the extinction band corresponding to the short axis is blue-shifted with respect to the SP band of spherical particles (peaked at 418 nm). The spectra in Fig. 5.2(a) and 5.2(b) (multi-shot mode) match this expectation, at least qualitatively. In the single-shot regime, however, even the SP band of the minor axis is red-shifted with respect to the SP band of the initially spherical particles [Figs. 5.2(c) and 5.2(d)]. This discrepancy can be solved by dropping the assumption of volume conservation: as Fig. 5.1(c, d) clearly shows, a halo of small silver particles surrounds the particle after shape

change [5.12]. Luminescence studies proved that also Ag ions are in the vicinity of the particles [5.17]. Thus, the halo can modify the dielectric constant of the particles' surroundings, which will in general change the SP resonances. In particular, an increase of the host dielectric constant (which is expected for Ag ions) results in a red-shift of the SP resonance band.

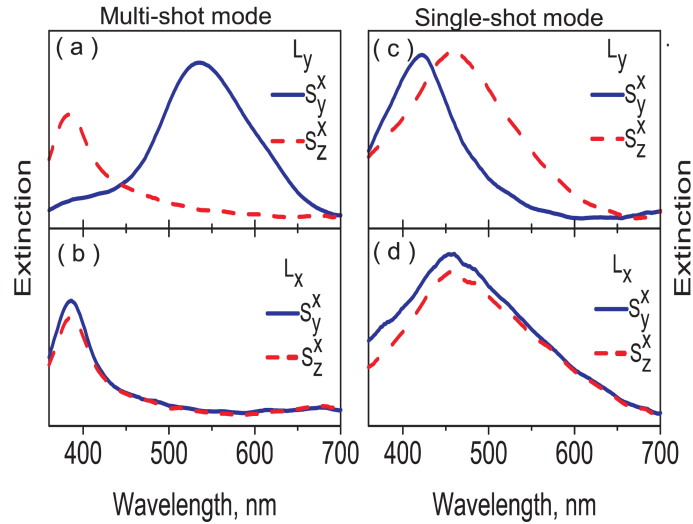


Fig. 5.3. Polarized extinction spectra  $S^x$ .

We have thus tried to predict the spectral positions of the SP bands observed in our experiments by theoretical calculations based on the Modified Long Wavelength Approximation (MLWA) [5.15], where we varied the dielectric constant  $\epsilon$  of the glass and the aspect ratio  $a/c$  of the particles. To account for the loss of silver atoms needed for halo formation, we also included a variable volume reduction  $\Delta V$ . Within the MLWA we could match the experimentally observed SP band positions by using the following parameters: (i)  $\epsilon = 2.7$ ,  $a/c = 1.8$ ,  $\Delta V = 6\%$  in multi-shot mode, and (ii)  $\epsilon = 3.0$ ,  $a/c = 1.1$ ,  $\Delta V = 10\%$  in single-shot mode. The relevance of these best fit parameters is limited, because it is unknown if Ag ions or the small halo clusters dominate the refractive index change; in the latter case strong dispersion (not accounted for in the calculations) would have to be considered. Nonetheless, several interesting qualitative conclusions can be drawn: First, the calculations clearly indicate that the red-shift of both the  $S_x^z$  and  $S_y^z$  spectra in the single-shot irradiation mode can be ascribed mainly to the refractive index increase of the particle surroundings due to the halo. Second, the relative trend of larger volume loss and larger refractive index increase in single-shot mode is compatible with Fig. 5.1(c, d); and it is reasonable that the higher irradiation intensity in single-shot mode ejects more material in the glass matrix. Finally, also the trend of aspect ratios reflects the results of TEM studies at least qualitatively. For more details the size distribution would have to be included in the calculation.

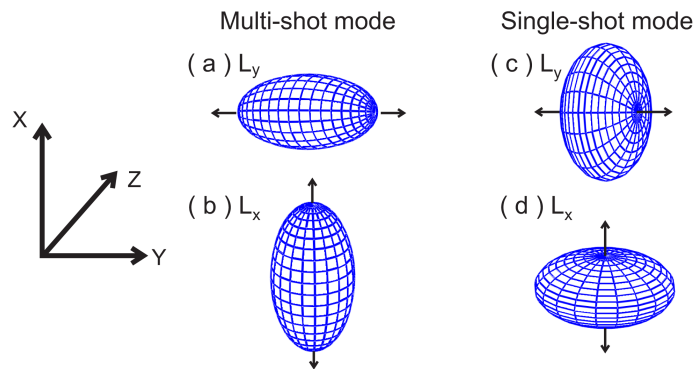


Fig. 5.4. The scheme of deformed nanoparticles shapes.

Summarizing the above given results we found that in multi-shot mode (relatively low intensity) the initial nanospheres are transformed to prolate spheroids, whereas in single-shot regime (higher intensity) oblate spheroids are produced. The symmetry axis of the spheroids is oriented parallel to the (linear) laser polarization for both irradiation modes. Simulations of the optical extinction spectra indicated that the halo of small silver particles and silver ions accompanying the laser induced shape transformation cause the observed red-shift of the surface plasmon resonances via an increase of the host dielectric constant.

#### Shape of nanoparticles after irradiation by circularly polarized pulses

Previous experiments (done by M. Kaempfe *et al.*) using circularly polarized pulses for irradiation of silver nanoparticles in glass show no dichroism in the optical spectra measured with light propagating in the same direction as the laser pulses (i.e., along the surface normal) [5.11]. Also transmission electron microscopy images measured in a plane perpendicular to the laser do not give any hint to anisotropy of the NP shapes. As the examples presented in Fig. 5.5 show, the nanoparticles stay approximately spherical after irradiation, but have the characteristic halo of small silver clusters (particles) being a typical concomitant phenomenon of fs laser induced NP shape transformation.

Comparing Figs. 5.5(a) and (b) one gets the impression that the particle radius after shape change has increased. This could be explained by the assumption of a flattened, oblate NP; of course the TEM images alone discourage this conclusion, since they stem from different locations on the sample (different NPs).

Fig. 5.6(a) shows the extinction spectra  $S_x^z$  and  $S_y^z$  from a sample irradiated by circular polarized pulses and measured normal to the original surface. It is seen that both spectra are nearly identical. The broad SP bands are centered at around 460 nm. The obtained results are comparable to those published earlier [5.11], where no dichroism was observed. At that time, the red shift of the bands was supposed to be a result of halo (very small silver particles and ions in surrounding of the main nanoparticle) formation only, while the main particles were believed to stay

spherical. If this were true the whole spectral change would have to be attributed to changes of host (glass) dielectric constant. Although it is known, in principle, that an increase of the glass dielectric constant leads to a red-shift of the SP bands [5.4, 5.5], such strong effects as observed in Fig. 5.6(a) would require much larger changes ( $\epsilon \sim 4$ ) than have been concluded in previous subsection for nanoparticles irradiated by linearly polarized pulses.

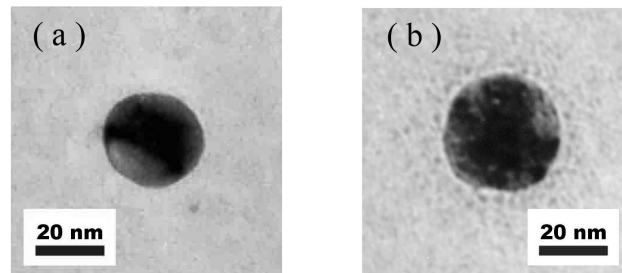


Fig. 5.5. TEM images of (a) original nanoparticles; (b) irradiated by pulses with circular polarization.

An alternative explanation for the red-shifted SP band is the assumption that, roughly spoken, flattened disks are produced upon fs laser irradiation. It is well-known, both from Mie theory [5.16] and experiments on supported NPs on surfaces [5.6] that oblate spheroids show red-shifted (blue-shifted) SP bands for polarization along the major (minor) axes, compared to the SP band of spheres with the same volume. In our case, the long axes of the spheroid should lie within the x-y plane, and the short axis in z-direction, to be compatible with TEM results (Fig. 5.5) and the spectra of Fig. 5.6(a). Then, in y-z (and/or x-z) plane dichroism should be seen. Moreover, the SP band corresponding to the minor axis then must be expected to be blue-shifted with respect to the SP band of the spherical particles (peaked at 413 nm), while the absorption band connected with the major axis should be similar to those measured in x-y plane [5.15, 5.16].

The polarized extinction spectra  $s_y^x$  and  $s_z^x$ , given in Fig. 5.6(b), prove all these predictions. It can be seen that the position and the shape of the  $s_y^x$  spectrum measured 0.5  $\mu\text{m}$  from the surface (short-dashed, blue line) are very similar to the  $s_y^z$  spectrum, while the  $s_z^x$  band has a peak around 370 nm. The  $s_y^z$  spectrum integrates over the whole layer, while  $s_y^x$  only refers to a slice located at some distance below the surface. This is the reason for the slight difference. The  $s^x$  spectra measured further away from the surface [Fig. 5.6(b) dashed and solid lines] show, on average, smaller shifts of both SP bands with respect to the original one. It can be explained by the fact that on its way through the NP layer, the laser pulses intensity is diminished, leading to different degrees of shape transformation in different depths. Furthermore, also size and concentration of the NPs are not constant across the particle-containing layer due to the process of Ag nanoparticle preparation. This may also contribute to the depth variation of the spectra shown in Fig. 5.6(b). We have

also measured the spectra in y-direction and found that they match the  $S^x$  ones very well. This proves the rotational symmetry of the NPs after shape transformation.

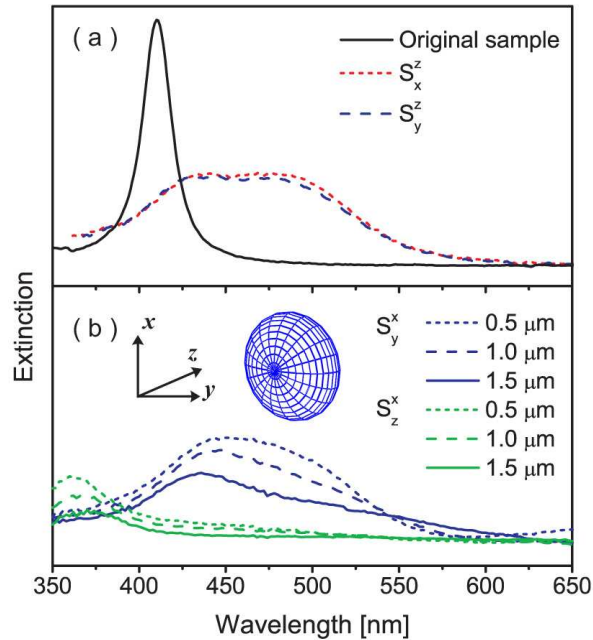


Fig. 5.6. Polarized extinction spectra  $S^z$  and  $S^x$ . Inset: Representation of nanoparticles' shape after transformation.

Over all, our results provide strong evidence that silver nanoparticles have been transformed to oblate spheroids with their symmetry axes parallel to the propagation direction of circularly polarized fs laser pulses [inset of Fig. 5.6(b)]. Using Mie theory for spheroids [5.16] we have estimated the aspect ratio of shape-transformed particles, and found that it varies from 1.6 to 1.9 within the depth of the NPs containing layer.

All these findings, as it will be shown later, strongly support the assumption that the photoionization of NPs by directional electron emission along the electric field vector of the laser light is the one of the most important processes in laser-induced shape transformation of metal nanoparticles in glass.

### 5.1.2. Effect of the laser pulse intensity and writing density on the anisotropic shape modifications

For measurements of the intensity dependences we used a technique of space resolved transmission spectra described in details in the Chapter 4.6. In combination with laser beam profile measurements the space resolved spectra were correlated with local laser pulse intensities (see Chapter 4.6).

We have produced various dichroic areas on the sample by irradiating different numbers of laser pulses (ranging from 1 to 5000) to the same spot. The huge number



of spectra resulting from the described analysis can only be shown here in a parametrized form (see below). Nonetheless, to demonstrate the quality of the spectra and explain the parametrization, a few examples are shown in Fig. 5.7. Figs. 5.7(a, c) represent the case of multi-shot, Figs. 5.7(b, d) that of single shot irradiation. In general, the original SPR band peaked at  $\lambda = 413$  nm splits into two polarization dependent bands upon irradiation, but with significant dependence on peak pulse intensity and number of pulses applied. Fig. 5.7(a) shows multi-shot irradiation (1000 pulses at  $0.6 \text{ TW/cm}^2$ ), which produces bands on different sides of the original SPR band: for polarization parallel to that of the laser (p-polarized, blue line), the peak position is shifted to longer wavelengths, while for perpendicular polarization (s-polarized, red line) the band is observed at a shorter wavelength.

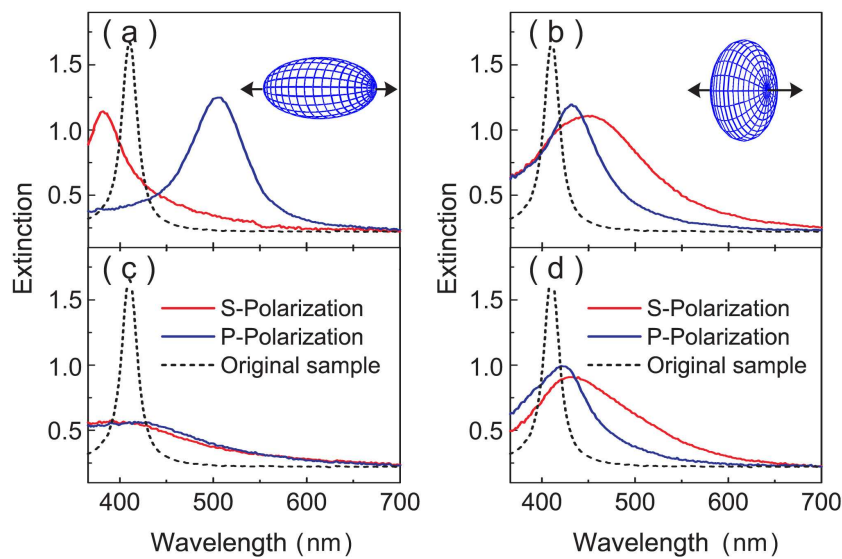


Fig. 5.7. Polarized extinction spectra of original and irradiated samples: a) multi-shot regime (1000 pulses per spot), peak pulse intensity  $I_p = 0.6 \text{ TW/cm}^2$ ; b) single shot regime,  $I_p = 3 \text{ TW/cm}^2$ ; c) multi-shot (5000 pulses per spot),  $I_p = 1.2 \text{ TW/cm}^2$ ; d) single shot,  $I_p = 3.5 \text{ TW/cm}^2$ .

This can be explained on the nanoscale by prolate silver spheroids with their symmetry axes oriented along the laser polarization (see previous section) [inset in Fig. 5.7(a)]. In the single-shot case [Fig. 5.7(b), referring to  $3 \text{ TW/cm}^2$ ], the s-polarized band has a larger red-shift than the p-polarized band. Additionally, both bands are red-shifted in this case. These spectra are due to oblate Ag particles [inset in Fig. 2(b)], again with their symmetry axes oriented along the (horizontal) laser polarization [5.18]. At even higher intensities and, in particular, in the multi-shot regime, the spectral shifts are becoming smaller and the band integrals decrease. These effects, which are obviously indicating – at least partial – destruction of the silver nanoparticles, are most clearly seen in Fig. 5.7(c) (representing 5000 pulses at  $1.2 \text{ TW/cm}^2$ ), but tentatively also in the single-shot regime [Fig. 5.7(d),  $3.5 \text{ TW/cm}^2$ ].

In general, the examples of Fig. 5.7 show clearly that the laser-induced shape transformations of Ag nanoparticles and the observable spectral parameters connected with it (orientation of dichroism, peak position and integrated extinction of the SPR bands) are strongly depending on the peak pulse intensity and the number of pulses irradiated to one spot. In order to elucidate the key parameters for the obviously different reshaping mechanisms, we have determined the SP peak central wavelengths as a function of local intensity from various spots irradiated with different number of laser pulses.

These results, a selection of which is presented in parametrized form in Fig. 5.8, show that laser-induced spectral changes start at intensities of 0.2-0.3 TW/cm<sup>2</sup>. For single-shot irradiation [Fig. 5.8(a)], increase of pulse intensity above this threshold leads to shift of both SP bands towards longer wavelengths. First, in the region of ~0.32 TW/cm<sup>2</sup> one observes a rather weak dichroism, where the p-polarized SP band has the stronger red-shift. At approximately 2 TW/cm<sup>2</sup> the extinction is becoming isotropic again, seen as crossing of the curves for s- and p-polarization at  $\lambda = 427$  nm. Above 2 TW/cm<sup>2</sup> a reversed dichroism is observed, i.e. the s-polarization band is now more red-shifted than the p-band. The maximum spectral gap between p- and s-polarized SP bands (peaks at 430 nm and 450 nm, respectively) is found at ~3.2 TW/cm<sup>2</sup>. At still higher intensity beyond 3.2 TW/cm<sup>2</sup> (not shown on the Fig. 5.8) the SP bands move back toward shorter wavelengths, and the integrated band extinction decreases, indicating (partial) destruction of the silver nanoparticles.

Irradiating 25 pulses to one spot [Fig. 5.8(b)] we find in general a similar peak pulse intensity dependence of the induced dichroism with the two characteristic intensity ranges. There are, however, some important differences compared to the single-shot case: (i) the dichroism (spectral spacing between the polarization dependent bands) is much larger in the low intensity range (below 2 TW/cm<sup>2</sup>); (ii) between 0.3 and 1.3 TW/cm<sup>2</sup> the s-polarized SP band is blue-shifted relative to the original SP peak at 413 nm; (iii) the region of reversed dichroism has shrunk considerably, because already from ~2.3 TW/cm<sup>2</sup> on bleaching of the extinction (particle destruction) starts. In such cases the analysis of the SP peak central wavelengths was halted (grey regions in Fig. 5.8).

If the number of pulses irradiated to one spot is further increased one observes that the maximum dichroism grows and is reached at lower peak pulse intensity [Figs. 5.8(c-f); note the scales change from Fig. 5.8(c) to 5.8(d)]. The crossing point of the curves for the p- and s-band, however, remains approximately constant around 2 TW/cm<sup>2</sup>, while the region of beginning particle destruction comes down to lower intensity step by step to finally ~0.7 TW/cm<sup>2</sup> at 5000 pulses per spot [Fig. 5.8(f)]. Thus, for 100 or more pulses per spot we can only observe the low intensity region of spectral changes with the corresponding dichroism, because following increase of intensity leads to destruction of nanoparticles and results in a bleaching of SP bands. The maximum dichroism recognized in our experiments was found in the case of 5000 pulses, where, at the pulse intensity of 0.65 TW/cm<sup>2</sup>, the p- and s-bands are peaked at 525 nm and 390 nm, respectively. It should be mentioned here that even more than 5000 pulses per spot do not increase the induced dichroism further.

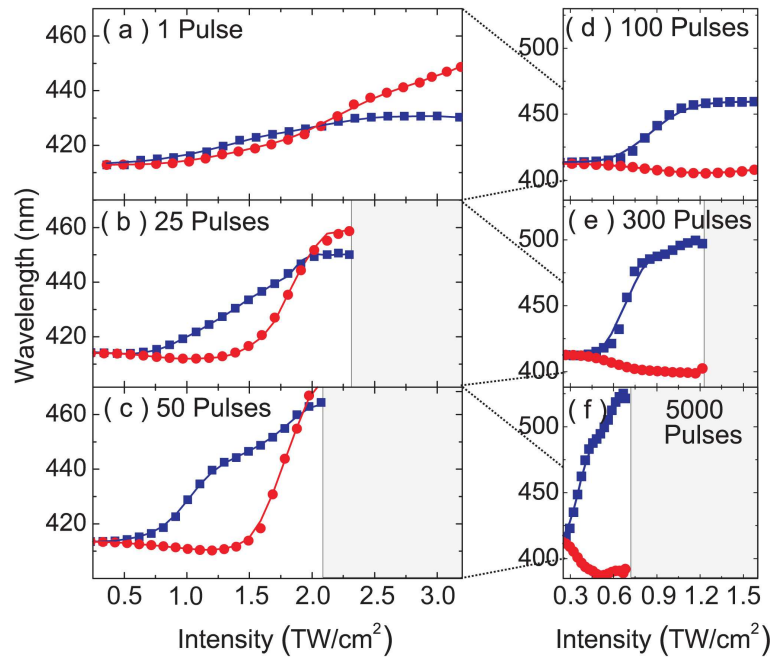


Fig. 5.8. Dependences of the SP maximum in polarized extinction spectra of soda-lime glass with spherical Ag nanoparticles on laser pulse intensity by irradiation at 400 nm. Red circles – s-polarization, blue squares – p-polarization, light gray area – region of the SP bleaching.

As was shown previously and also in ref. 5.10, 5.11, 5.12, 5.13, 5.17, the principal persistent modifications induced by fs laser pulses do not only comprise the transformation of nanoparticle shapes, but also the generation of a surrounding region of small Ag particles ('halo'). While the first effect explains the splitting of the SP band (dichroism), the second one causes, in a first approximation, a modified matrix refractive index which may lead to isotropic spectral shift of the SP bands [5.18]. In this work we have observed both band splitting and spectral shifts as a function of both peak intensity of the fs laser pulses and irradiation density (number of pulses per spot). The first important result was that, independent of the number of pulses applied, there exist two special intensities  $I_1 \approx 0.2 \text{ TW/cm}^2$  and  $I_2 \approx 2 \text{ TW/cm}^2$ . For intensities  $I < I_1$  there is no spectral change at all, and at  $I = I_2$  only spectral shift of the SP band to long wavelengths is observed. In the intensity region  $I_1 < I < I_2$ , dichroism is found with the larger red-shift for the p-polarized SP band, while for  $I > I_2$  a reversed dichroism is seen. This indicates that the processes of shape transformation are controlled by the laser pulse intensity (energy density per pulse), while the number of pulses applied mainly accumulates the changes caused by each single pulse.

Looking in more detail to the low-intensity region  $I_1 < I < I_2$  first, the dichroism observed there could be associated with a transformation of the original silver nanoparticles to prolate spheroids with their long axis oriented parallel to the laser polarization (see previous section). Anticipating volume conservation for the silver, Mie theory predicts for this case blue- (red-) shift of the SPR of the short (long)

particle axis, the spectral spacing between the two bands being correlated to the aspect ratio of the nanoparticle. So the growth of dichroism with increasing number of pulses can be explained by successive increase of the particles' aspect ratio. A red-shift of both bands however, as observed for 1 pulse for all intensities or at  $I > 1.5 \text{ TW/cm}^2$  at 25 or 50 pulses, can only be explained by additional modification of the host matrix in the vicinity of the nanoparticle which was shown in ref. 5.17. So it is obvious to assign the increasing general red-shift for higher pulse intensities to a growing influence of the halo.

In the high-intensity region  $I > I_2$ , oblate spheroids with their symmetry axes (short axis) along the laser polarization are produced (Chapter 5.1.1). Again the fact that both SP bands are red-shifted indicates significant modification of the particle surroundings, because otherwise the short axis should show a blue-shifted SP band.

To get an idea about the nanoscopic modifications in the region around  $I_2 \approx 2 \text{ TW/cm}^2$ , and in the region of beginning particle destruction (where SP band extinction starts to decrease again), transmission electron microscopy is quite instructive. It should be mentioned however that it is not possible to assign an exact local irradiation intensity to a special TEM image. Fig. 5.9 shows two examples for particle shapes found after single-shot irradiation in the high intensity regime; Fig. 5.9(a) refers to intermediate intensity (around  $I_2$ ), Fig. 5.9(b) to very high intensity (significantly above  $I_2$ ). In the first case, a fairly spherical particle with a limited halo region is seen. In contrast, at very high intensity there is on one hand a non-spherical central Ag particle, but a much larger region of small silver fragments. Considering that this image was taken after one laser pulse only, it is quite plausible that after several pulses of sufficiently high intensity the particles are destroyed completely and the pertinent SPR band vanishes. In our experiments, total bleaching of the samples has been observed at intensities higher than  $1.2 \text{ TW/cm}^2$  applying at least 5000 pulses per spot. We interpret this finding as complete destruction of the Ag nanoparticles into small fragments without distinct SPR.

On the low-intensity side, in particular if one irradiates the sample with many pulses only slightly above the modification threshold ( $0.2 - 0.3 \text{ TW/cm}^2$ ), the maximum spectral shift (and thus the maximum particle aspect ratio) achievable is limited [5.13], because due to successive particle deformation the SP band polarized along the laser polarization moves out of resonance decreasing the interaction with the laser pulses.

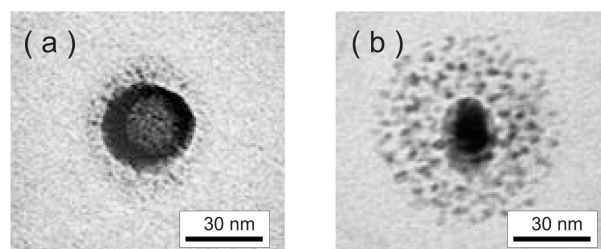


Fig. 5.9. TEM of Ag nanoparticles in soda-lime glass after irradiation: (a) in the region around  $I_2 \approx 2 \text{ TW/cm}^2$ , (b) partially destructed nanoparticle.

### *5.1.3. Summary*

In this subchapter we have shown that laser induced shape transformation of silver nanoparticles embedded in glass can only be achieved using fs pulses of a minimum peak pulse intensity of  $0.2 \text{ TW/cm}^2$ . In the case of linearly polarized pulses, above this threshold, two main intensity ranges can be distinguished macroscopically by a reversal of the observed dichroism, which is caused by different shapes of the nanoparticles: in the low intensity range (between  $0.2 \text{ TW/cm}^2$  and  $2 \text{ TW/cm}^2$ ) uniformly oriented, prolate spheroids with different aspect ratios are produced, while applying intensities above  $2 \text{ TW/cm}^2$  results in oblate spheroids. Directly at  $2 \text{ TW/cm}^2$  no dichroism, but only red-shift of the surface plasmon bands is seen, plausibly explained by spherical particles with halo, which have been recognized in TEM images. Increasing the number of pulses increases the induced dichroism for the low intensities and leads to total destruction of the silver nanoparticles for high intensities.

In the case of irradiation by fs laser pulses with circular polarization (in multi-shot, low intensity mode), the results show however that the particles have a shape of oblate spheroids with the major axes lying in the plane of laser polarization.

As one can see, the observed anisotropic shape modifications are strongly correlated with the laser polarisation indicating obviously nonlinear interaction of the SP with intense laser electromagnetic fields. In other words, the processes, which define a preferable orientation of the nanoparticles, should occur at time scales about of the laser pulse duration. At the same time, the thermal effects induced by the laser excitation of spherical Ag nanoparticles can only result in isotropic changes. Therefore, taking into account these finding and the discussion given in Chapter 3, one can suggest that the main process responsible for the NP shape modification have to be the directed (pulse-enhanced) electron emission from nanoparticle. In turn, depending on irradiation conditions, this electron emission can trigger some other processes, which at the end lead to the different shapes of nanoparticles.

## **5.2. “Off-resonant” excitation: irradiation wavelength dependence**

In this section, we will consider the excitation of silver nanoparticles embedded in soda lime glass at different wavelengths and how it is affected on the induced dichroism. As it was shown in previous section, resonant irradiation close to the initial SP band in the multi shot regime can induce spectral gaps of up to 180 nm, and the position of p-polarized SP band (observed with light polarized parallel to the laser polarization) can be varied in the region of 420-530 nm. Larger dichroism or larger induced red-shift of the p-polarized SP band is not possible by near-resonant excitation: any further increase of intensity or number of pulses applied to one sample position leads to bleaching of the SP bands, which can be explained by (partial) nanoparticle destruction [5.19]. As many possible applications for optical elements prepared by proposed technique require polarization contrast at larger wavelengths in the visible and near IR spectral range, it is attractive to look for ways to meet this needs.

We will show that tuning of the irradiation wavelength is a very powerful parameter for reshaping Ag nanoparticles to large aspect ratios. First, we have found that even rather strongly red-shifted excitation (with respect to the initial SP band) can, in spite of the low remaining SP absorption in this region, still very effectively induce a nanoparticle shape transformation to spheroids; in particular, such 'off-resonant' irradiation can create an even larger dichroism than resonant excitation. Second, we will demonstrate that subsequent irradiation by increasing laser wavelengths increases the particles' aspect ratio and thus the induced dichroism further, allowing to shift the p-polarized SP band down to the near infrared region. At the end, we will show the results of simultaneous irradiation of the sample by the pulses with different wavelengths, which results in a similar elongation of nanoparticles as it is obtained by subsequent irradiation.

### 5.2.1. Long wavelength irradiation

It should be mentioned here that all experimental results shown below have been conducted in the multi shot regime (Chapter 5.1). Figure 5.10 gives a first example for "off-resonant" excitation. We will use this notion in the following to characterize a situation where the laser wavelength is considerably larger than the maximum of the SP resonance. The polarized extinction spectra in Fig. 5.10 were measured on a sample containing Ag nanoparticles which was irradiated by 1000 pulses per spot at  $\lambda = 550$  nm with a peak pulse intensity of  $1.2 \text{ TW/cm}^2$ . The effect of this irradiation is similar to the one obtained by resonance excitation, namely, the original SP band of the spherical Ag nanoparticles peaked at  $\lambda = 413$  nm splits into two polarization dependent bands. However, in this case, the p-polarized SP band (seen with light polarized parallel to the laser polarization) is peaked at 620 nm, while the s-polarization (perpendicular to laser) is shifted to shorter wavelengths, overlapped by a small residual absorption at 413 nm. This large spectral gap of p- and s-polarized bands leads to a good polarization contrast at 620 nm, i.e., low and high transmission for p- and s-polarization, respectively. In analogy to previous experiments, we can easily conclude that also in case of "off-resonant excitation" the nanoparticles are transformed into prolate spheroids (Chapter 5.1.1). From the spectral gap between the maxima of polarized extinction bands being significantly larger than in case of resonant excitation, it is obvious that the aspect ratio of the reshaped nanoparticles is also larger than for resonant excitation.

Additionally, similar to the case of resonant irradiation, the particle elongation and the corresponding magnitude of induced dichroism can be tuned by variation of the peak pulse intensity and/or by number of pulses per spot. Figure 5.11 illustrates the effect of different writing densities for samples irradiated at 550 nm with peak pulse intensity of  $1.3 \text{ TW/cm}^2$ . Only the p-polarized extinction spectra are shown. It is clearly seen that, increasing the number of applied pulses from 200 to 1000, both peak wavelength and integrated extinction of the p-polarized band are increasing, while the absorption peak in s-polarization moves slightly to shorter wavelengths (not shown in Fig. 5.11). For further increase of the writing density, however, the p-polarized SP band starts to shift back towards shorter wavelengths, accompanied by decrease of amplitude and increase of bandwidth. This bleaching, which was

interpreted in previous section as partial destruction of the silver nanoparticles is clearly seen in the spectrum obtained after shining 4000 pulses per spot on the sample. Again the off-resonant irradiation behaves very similar to the resonant case: up to a certain amount of pulses per spot, the dichroism can be increased by applying a larger number of pulses to the sample, but beyond this value (in the range of 1000 pulses/spot) the maximal spectral shift is limited by beginning destruction of the nanoparticles.

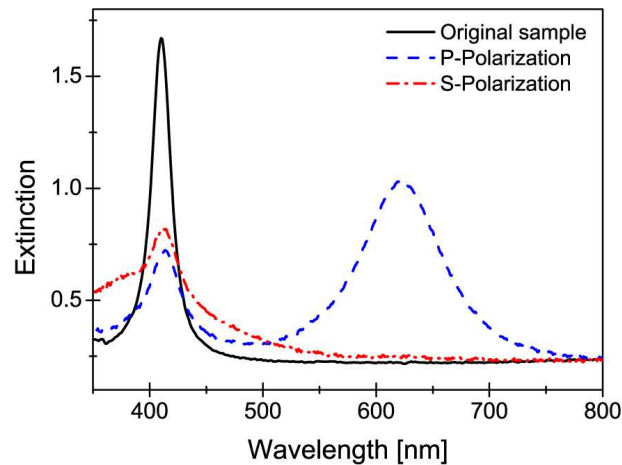


Fig. 5.10. Polarized extinction spectra of samples with Ag nanoparticles irradiated at 550 nm in multi-shot regime (1000 pulses in single spot), peak pulse intensity was  $1.2 \text{ TW/cm}^2$ .

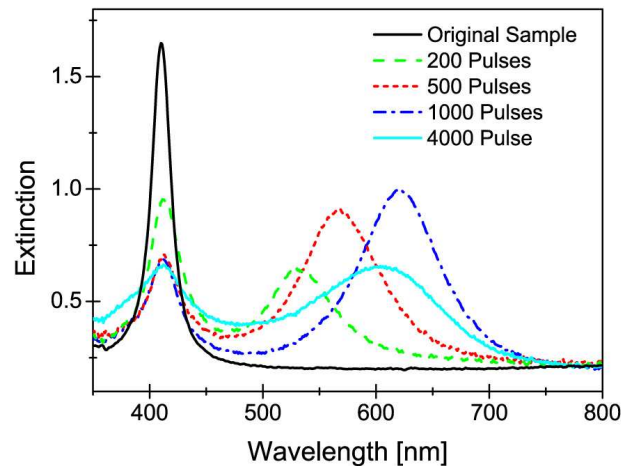


Fig. 5.11. P-polarized extinction spectra of original and irradiated sample with Ag nanoparticles; irradiation at 550 nm with different number of pulses applied, peak pulse intensity was  $1.3 \text{ TW/cm}^2$ .

The results discussed so far showed that irradiation of the samples at  $\lambda = 550 \text{ nm}$  with optimum laser intensity and number of pulses leads to a larger spectral gap between the SP bands than resonant excitation at  $\lambda = 400 \text{ nm}$  can do. Therefore, one

should expect a further increase of the induced dichroism when samples are being irradiated with even more off-resonant, longer wavelengths. We have also looked into this effect. Figure 5.12 shows three examples for p-polarized extinction spectra of samples irradiated at different wavelengths, here  $\lambda = 490$  nm, 560 nm, and 610 nm. The parameters of irradiation (laser intensity and number of pulses per spot) were chosen so that for each laser wavelength the maximal spectral shift was reached. It is clearly seen that in fact irradiation with the longer wavelengths leads to a larger red-shift of the p-polarized SP band. However, moving the irradiation wavelength further beyond 610 nm, the efficiency of nanoparticle shape transformation decreases more and more, and finally the laser pulses do not evoke any measurable extinction changes anymore. For our samples this was the case for  $\lambda \geq 670$  nm; for instance, even the very strong laser fundamental at 800 nm does not cause dichroism when irradiated on a sample with original, spherical Ag nanoparticles.

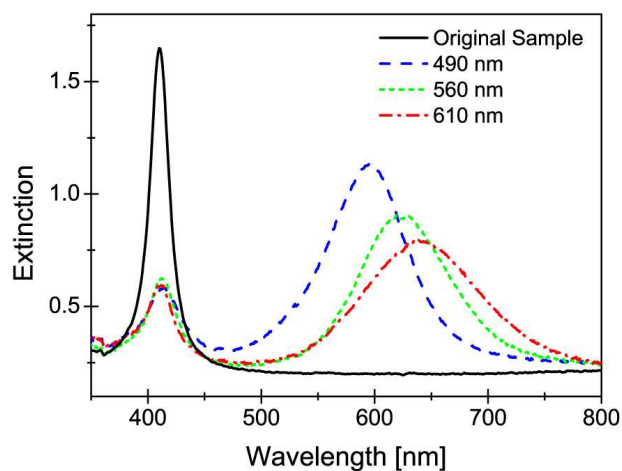


Fig. 5.12. P-polarized extinction spectra of original and irradiated sample with Ag nanoparticles by different wavelengths irradiation. Intensity and number of pulses are optimized to achieve the best dichroism.

The obvious conclusion from the above results is that there is a threshold in absorption efficiency, which limits the long wavelength irradiation. This and all other findings are in a good agreement with theory. As it was shown, the extinction efficiency decreases rapidly for wavelengths longer than SP resonance and at 800 nm it becomes almost zero (see for example Fig. 3.9). At the same time, the E-field enhancement, which is present in the long wavelength region (Fig. 3.9 and Fig. 3.10), increases the probability of direct electron emission and makes the shape transformation of nanoparticles possible even for off-resonant excitation. And, as long as absorption efficiency and laser intensity are high enough to emit ions from the particles and transform their shape at least a little bit after the first pulse, the process is expected to work, because even very minor changes per pulse shift the p-polarized SP band closer to resonance with the irradiation wavelength and so, step by step, increase the efficiency of shape transformation for the next pulse. The process then will go on until the excitation wavelength is located considerably far in the blue wing of the p-polarized SP band. From then on the same mechanisms like in



the case of resonant excitation lead to particle destruction and limit the spectral gap achievable by single-wavelength irradiation.

### 5.2.2. Subsequent irradiation

As one could see in previous section, the long wavelength irradiation leads to the higher elongation of nanoparticles. However, this type of irradiation has also the limit as in the case of resonance excitation. Nevertheless, we have found that this limitation can be overcome by multi-wavelength irradiation, i.e. subsequent irradiations of the same sample area by different laser wavelengths. In particular after the first step the laser is tuned to another off-resonant position on the long-wavelength side of the already modified SP resonance, much larger dichroism compared to single-wavelength irradiation can be prepared. As an example, Fig. 5.13 shows the extinction spectra of a sample which was first irradiated at 535 nm, then at 670 nm with polarization parallel to the long axis of the already modified particles. It is clearly seen that the p-polarized band shifts in the second step further from peak position 560 nm to 760 nm. At the same time, the absorption peak in s-polarization shifts to shorter wavelengths. This large spectral gap between s- and p-polarized bands corresponds to an aspect ratio of  $(a/c) > 3$  of the nanoparticles, which is proven by the TEM image shown in the inset of Fig. 5.13. Clearly, subsequent irradiation with increasing laser wavelength leads to very high dichroism, and because of the minimal losses for s-polarized light at 760 nm, the polarization contrast is also high. It should be mentioned here that further red-shift of the p-polarized SP band can be done by further irradiations with successively longer laser wavelengths at each step. We have performed preliminary experiments with a third irradiation at  $\lambda = 800$  nm, which proved this idea. It is obvious that, by proper choice of the irradiation sequence and optimization of the pertinent laser parameters, the range of dichroism induced by this technique can be extended into the IR region.

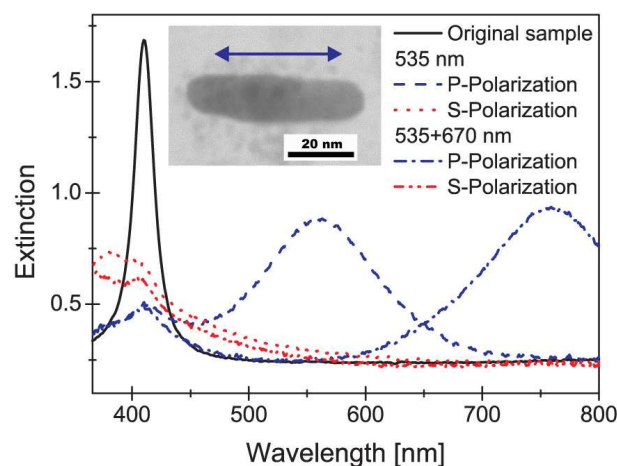


Fig. 5.13. Polarized extinction spectra of samples with Ag nanoparticles irradiated firstly at 535 nm and subsequently at 670 nm laser pulses, 1000 pulses per spot, peak pulse intensity was  $1.5 \text{ TW/cm}^2$ . Inset: TEM image of deformed nanoparticles. Laser polarization is given as an arrow.

### 5.2.3. “Residual” peak observed by long wavelength irradiation

Looking again at Figs. 5.10 to 5.13, one can see the already mentioned small residual peak in the region of 413 nm, being present in both polarized spectra in all cases. The central wavelength of these isotropic bands, which can be undesirable for some potential applications, is equal to the central wavelength of the SP band for spherical particles. Therefore we can surmise that not all nanoparticles are being reshaped by the irradiation. If this is correct, the application of higher intensity should reduce the residual peaks. Insofar the spectra in Fig. 5.13 referring to the first irradiation (at 535 nm) confirm this assumption. Because of the higher peak intensity of  $1.5 \text{ TW/cm}^2$  compared to the other experiments the lower amplitudes of the residual peaks is observed. At the same time, as it has been observed in previously, the laser pulse intensity higher than needed for maximal dichroism leads to partial destruction of already modified nanoparticles, resulting in a smaller spectral gap than in the optimal case.

Searching for means to remove or at least minimize these isotropic absorptions, it has to be analyzed if the non-deformed particles are distributed more or less homogeneously throughout the whole particle-containing layer or if they are mainly concentrated in a special depth, for instance at the top or bottom of the nanoparticle layer. In the first case, the desired removal of the isotropic peak requires either special irradiation techniques or initial samples with special particle size distribution, while in the second case one could possibly remove the layer containing non-deformed particles mechanically.

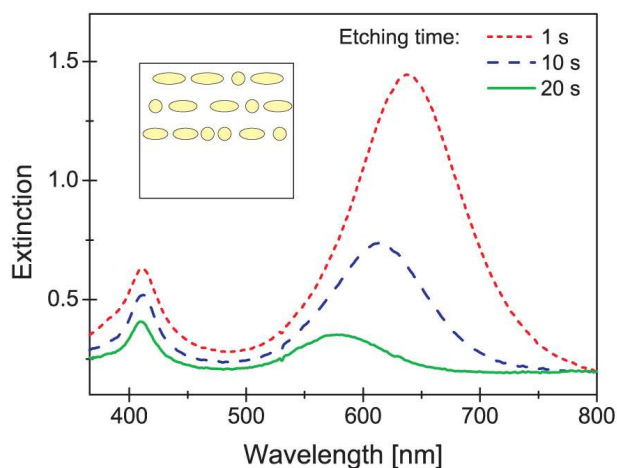


Fig.5.14. P-polarized extinction spectra of samples with Ag nanoparticles measured after different etching time (see text).

To look for the location of non-transformed silver nanoparticles in the glass, we have etched an irradiated sample stepwise in HF acid, and recorded the optical transmission spectra after each etching step. Figure 5.14 shows the p-polarized extinction spectra obtained after different etching times. It is easily seen that the amplitudes of the bands corresponding to both transformed and not transformed nanoparticles are decreasing simultaneously with etching time, but with two

important differences: first, the peak extinction of the transformed particles' SP band decreases much faster than the 413 nm absorption; second, the peak position of the SP band caused by the spheroidal nanoparticles shifts from 620 nm to 585 nm upon etching. These observations indicate that (i) non-deformed particles are present to some extent throughout the whole particle layer, but with higher concentration in the depth, and (ii) the aspect ratio of the shape-transformed particles is highest directly at the surface and decreases with distance from the sample surface (see inset of Fig. 5.14). So obviously, these effects are governed mainly by the decreasing intensity of the laser pulses on their way through the particle layer.

Therefore, an increase of irradiation intensity or number of pulses is not the best way to remove the residual peak, because then the already transformed particles will partially be destroyed, decreasing the prepared polarization contrast again. Instead, it seems favourable to apply subsequent irradiation to the samples, for instance first with the wavelength close to SP resonance (and ideally from the backside of the sample) and then by pulses with longer wavelengths as described above.

#### 5.2.4. Two wavelengths irradiation

In Chapter 5.2.2, we have shown that subsequent irradiation of the nanoparticles embedded in glass by tuning the wavelength of the pulses between irradiations to the already modified SP resonance leads to the following elongation of the particles. In this experiment the intensities of the pulses for every next subsequent irradiation was in the same order of magnitude to the intensity needed for NP shape transformation (around 0.5-1.5 TW/cm<sup>2</sup>). In this section, we will show the experiment, which was performed on the sample simultaneously irradiated by the pulses at different wavelengths; namely 532 and 800 nm. Moreover, the intensity of the green pulses was around 1.4 TW/cm<sup>2</sup>, while 800 nm pulses had the intensity of few orders of magnitude lower. Figure 5.15 shows the spectrum of the laser pulses used in experiment.

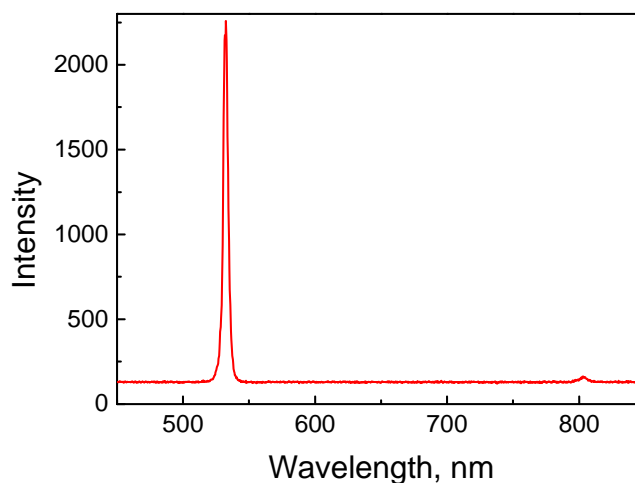


Fig. 5.15. Spectrum of the laser pulses used in experiment of simultaneous two wavelength irradiation.

The obtained results are presented in Fig. 5.16. Applying 1000 pulses (for every wavelength) leads to the similar results presented above for the case of long wavelength irradiation (Fig. 5.16, red curve). P-polarization band is peaked at ~570 nm, while s-polarized SP band is shifted to UV region (not shown in Fig. 5.16). At the same time, residual absorption at 410-420 nm (discussed in Chapter 5.2.3) is present. However, increasing the number of pulses to the value of 2000 results in a bleaching (amplitude decrease) of p-polarized SP band at ~570 nm and an appearance of additional band in the region of 750 nm (Fig. 5.19, blue, dashed curve). Following rise of the writing density amplifies the obtained results. Namely, the amplitude of the band located in yellow region is decreasing with simultaneous shift of the SP resonance to the shorter wavelength, while the band located in the red region has an inverse behavior (increase of the amplitude and shift to the IR region) (Fig. 5.16).

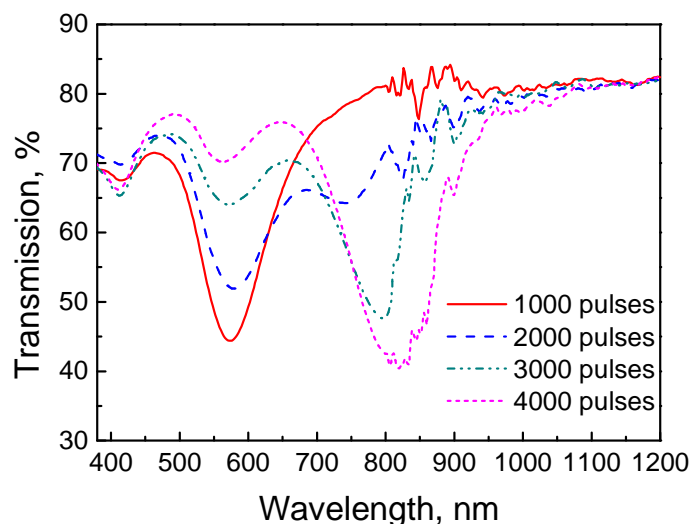


Fig.5.16. P-polarized transmission spectra of the sample with Ag nanoparticles irradiated simultaneously by the pulses at 532 and 800 nm. The noise in the spectra in the region of 800-900 nm is due to the edge of the working grating region in spectrometer.

The obtained results can be explained in the following way. First 1000 pulses lead to the transformation of initially spherical particles to the prolate spheroids with aspect ratio varying in the region of 2-2.5. Then, increasing the number of pulses, some number of nanoparticles with the highest aspect ratio starts to elongate further. As a result, the sample contains lower (with respect to the case of 1000 pulses irradiation) number of particles with the aspect ratio of 2.5 and additionally some number of nanoparticles, which have the higher elongation. Spectroscopically, we see the amplitude decrease of the band corresponded to the NPs with  $a/c \sim 2.5$  and additional band for higher elongated particles. Following increase of the writing density leads to decrease of the number of nanoparticles with aspect ratio of 2.5 (therefore, decrease in amplitude) and the further rise of the amount of longer NPs with simultaneous increase of elongation (increase of amplitude and red-shift). Residual absorption at

550 nm for the case of irradiation by 4000 pulses is due to the NPs with the lowest aspect ratio, which can not be transformed further (see as an example Chapter 5.2.3).

However, the question “how is it possible?” is still open. One of the possible and most probable effects, which can explain the obtained results, is the electric field enhancement and its dependence on the wavelength. During the irradiation of the first 1000 pulses, the electric field enhancement created by the green pulses, enhances the directed photoionization of NP and the existed processes are similar to ones going by the usual irradiation (will be discussed later), while the enhancement for the 800 nm pulses is very weak. This irradiation shifts the SP resonance and band of electric field enhancement factor more close to the wavelength of irradiation (Fig. 2.6, Fig. 3.10 and Ref. 5.20, 5.21). When both bands (SPR and EFE) are on the right side from the irradiation wavelength (after 1000 pulses), the electric field enhancement factor is very weak for the green pulses, while its value is high enough for the pulses at 800 nm. Thus, the pulses at 532 nm are not very efficient for directed photoionization, but they are strong enough to excite the electrons of nanoparticle. In turn, the weak pulses at 800 nm can not excite the nanoparticle, but the high EFE factor enhances the directional ionization of excited by the green pulses nanoparticle. As a result, the further elongation of NPs is happening.

It is also obviously that increasing the intensity of the IR pulses to the modification threshold can lead to the over-excitation of NP, which will result in destruction of the last one. At the same time, if the intensities of both pulses will be lower that the modification threshold, then the shape transformation will not be achieved.

At present, we perform the calculations of the spectra of electric field enhancement for prolate spheroids (in our case), which preliminarily confirm our assumptions.

### *5.2.5. Summary*

In summary, we have found that laser induced shape transformation of Ag nanoparticles is strongly dependent on the wavelength of fs laser pulses used for irradiation. The first striking observation is that considerably off-resonant excitation, i.e. irradiation with a laser wavelength shifted more than 100 nm to the long wavelength side of the SP resonance absorption of spherical nanoparticles (at 413 nm) can even more effectively transform the shapes of the nanoparticles to spheroids with large aspect ratios than near resonant interaction, in spite of the very weak coupling to the SPR in this region. The spectral gap between the polarized SP bands follows the increasing irradiation wavelengths up to  $\lambda \approx 650\text{nm}$ , and then the efficiency drops due to the finally vanishing coupling to the SPR and the decrease of the electric field enhancement. This limit can be overcome by subsequent irradiation with longer wavelengths, which were shown to shift the p-polarized SP band further to longer wavelengths. A band at 760 nm corresponding to Ag nanoparticles with aspect ratio  $a/c > 3$  was prepared by subsequent irradiation with 150 fs pulses at 535 nm and 670 nm. Additionally, we have found that the similar elongation of the nanoparticles can be obtained by simultaneous irradiation of the sample by the pulses at two wavelengths (532 and 800 nm in our case). Moreover, the intensity of the pulses at longer wavelength can (should) be much smaller than the modification

threshold. It was explained by the effect of EFE, which determines the directional ionisation of nanoparticle. We have also found that a residual absorption at 413 nm observed after off-resonant irradiation indicates a small fraction of non-deformed particles; an analysis of their spatial distribution suggests that they can be removed by an intermediate irradiation step with laser pulses resonant to the SPR of the non-transformed particles.

In general, the proposed technique of subsequent (or simultaneous) multi-wavelength, off-resonant irradiation of metal-glass nanocomposites has a huge potential for preparing polarizing elements with high polarization contrast at any desired spectral position in the visible and near IR spectral range.

### **5.3. Effects of temperature on the laser induced modifications of Ag nanoparticles**

In previous sections we have investigated the influence of irradiation laser parameters on the nanoparticles shape transformation. The studies presented in this section will be focused on the effects of temperature on the reshaping processes. As it was discussed in Chapter 3, upon absorbing the energy of the laser pulse, the oscillating conduction electrons of the NP heat up the silver lattice through electron-phonon (e-ph) couplings. The lattice gets to a very hot state within a short time (temperatures up to 2000 K) and it starts to heat up the surrounding glass matrix gradually. In this sense, the softening of the glass matrix around the NP is crucial for the NP to have some degrees of freedom for the necessary shape changes. On the other hand, it is known that heating of the sample exposed by fs laser up to 600°C corresponding to the transition temperature in soda-lime glass causes a restoration of spherical shape of the modified Ag nanoparticles [5.13, 5.22]. This allows us to assume that the fs laser assisted modification have to be occur in the nearest shells where large transient, localized heating is present, while the further shells of surrounding glass should be cold enough to keep the anisotropic shape of nanoparticle.

Additionally to these effects, it has also been shown in previous work [5.17], that annealing at moderate temperatures after fs irradiation may cause modification of the SPR bands (and thus also of NP shape and surrounding matrix). So, quite obviously the continuous global sample temperature as well as the transient local heating and cooling have considerable influence on the laser induced shape modification of metallic NPs embedded in glass.

In this section we will address these questions in a combined approach: first the transient energy/heat flow in the NP-Glass system after fs laser excitation will be discussed, then experimental studies varying sample temperature and laser repetition rate (heat accumulation in the focal volume) will be presented. Together these results will demonstrate that, on one hand, the laser-induced modification of NPs does occur only when the local transient temperature in the vicinity of the nanoparticle is sufficiently high (typically exceeding the glass transition temperature), while on the other hand even relatively small global constant temperature increase of the matrix

limits the anisotropy of reshaped nanoparticles, or even causes their (partial) dissolution.

### 5.3.1. Modelling of the heat flow from a laser-excited nanoparticle into the glass matrix (including ejection of ions)

As it was shown in Chapter 3, following the absorption of an intense femtosecond laser pulse, the excited electrons of the NP relax into a quasi-equilibrated hot electronic system via electron-electron scatterings. After establishing a thermal system, the hot electrons cool down by sharing their energy with the lattice via electron-phonon coupling, thereby heating up the NP. The heat gained by the NP lattice can be calculated from the heat lost by the electrons using a 2TM compatible with the strong excitation regime, the details of which were described previously (Chapter 3).

The electronic temperature of a single silver NP (having a radius of  $R = 15$  nm) reaches around  $10^4$  K upon absorption of a 100 fs pulse with  $0.5$  TW/cm<sup>2</sup> of intensity, which corresponds to an absorbed energy of around  $3 \times 10^{-13}$  J. Such a high electronic temperature is enough to heat up the Ag lattice to 2000 K. Afterwards, the electronic and lattice temperatures cool down together as the NP loses its energy to the surrounding “cold” glass matrix. To account for the NP-glass thermodynamics, we need to consider the cooling of the NP together with the heating of the glass in the frame of the mentioned 3TM. On the NP-glass interface, the heat flow from the hot NP to the glass can be estimated step by step through concentrated spherical shells. After the first shell of the glass is heated, the following heat transfer deep into the glass can be described by the radial heat conduction (Eq. 3.19).

However, it is known for our strong excitation regime that the NP gets ionized by the emission of electrons, which consequently forces the NP to eject Ag<sup>+</sup> ions to the glass matrix [5.17]. Therefore, the NP loses a part of its volume within 20 ps after the absorption of the laser pulse [5.23]. Compared to the usual heat conduction, ion emissions are definitely more effective channels of rapid energy transfer from the NP, so that after the ion emissions one would expect high temperature values for the glass in a broader range. Therefore, the above described 3TM calculations are valid only for a “closed system,” and we have to modify the 3TM by taking the fast contributions of ion emissions into account.

As the ions are distinguishable classical particles, we can employ the Boltzmann distribution to designate the amount of energy carried by each emitted ion. In other words, the distribution plots the fractional number of emitted particles  $N_i$  with respect to their corresponding energy  $E_i$ . It is known from the results of ion implantation experiments that Ag<sup>+</sup> ions having 7-10 keV of energy can penetrate up to 10 nm deep in the glass [5.24, 5.25], if the glass is initially at room temperature. Additionally, the ionic penetration depths increase with the increasing glass temperature [5.24, 5.26]. Therefore, we assume here that the emitted ions possess energy values from  $E_i = 0$  to 10 keV ( $i$  denotes a continuous set of energy states between these two values) with a maximum penetration depth of  $d = 10$  nm in glass. According to the exponential nature of the Boltzmann distribution, it is clear that a

high fraction of ions will possess very less energies, and only very few of the ions will have the maximum energy values. Additionally, the total number of ions  $N = \sum_i N_i$  emitted from the NP depends on the strength of the laser irradiation. The area under the Boltzmann distribution for each energy state  $E_i$  gives a part of the total energy taken out by the ions. As the penetration depths of the ions depend on their initial energies, we can simply match these partial energy values with the spatial range  $d = 0-10$  nm of the emitted ions. Therefore, we arrive at the spatial distribution of the energy that is transferred into the glass matrix. This energy distribution indicates that the highest amount of the energy emitted from the NP is located close to the surface of the NP; however, only small portions of the energy are transferred to the further spherical shells of the glass. At the end, we can convert the ionic energy into the glass temperature together with the calculation of the heat conduction in the glass.

Comprising these aspects, we can now calculate the spatial temperature distributions in the glass for different scenarios of heat transfer from the NP. Figure 5.17(a) shows the numerical calculations for several different scenarios. The dashed curve corresponds to the usual heat conduction from the NP at a time of  $t = 30$  ps after the NP lattice reaches its maximum temperature ( $T_{lattice}$ ). Because of the huge difference in thermal diffusivities of Ag ( $123 \text{ nm}^2/\text{ps}$ ) and glass ( $0.5 \text{ nm}^2/\text{ps}$ ), any temperature gradient within the NP can be neglected. As the heat diffusivity of glass is very low, the heat transfer is observed to affect only a very narrow volume of glass surrounding the NP. This means that the cooling of the NP happens rather slowly by the heat conduction alone.

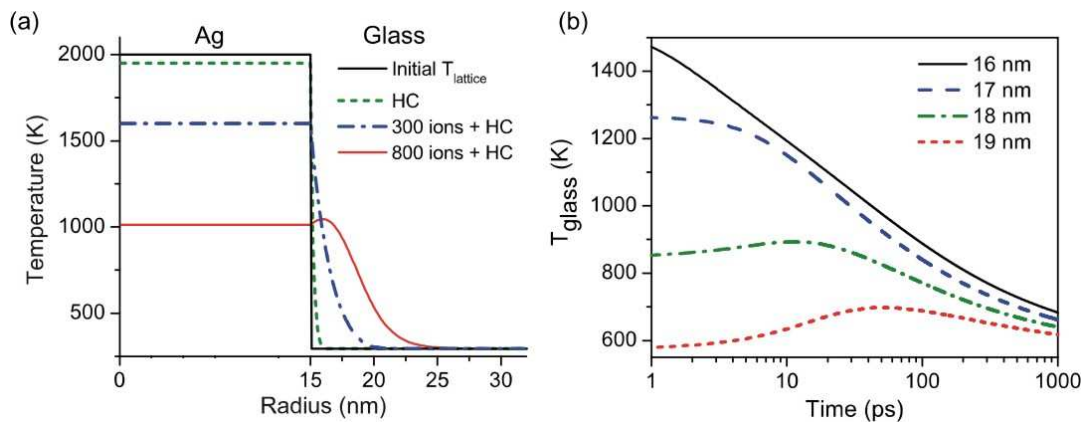


Fig. 5.17. (a) Temperature distribution in the NP-glass system for different scenarios: pure heat conduction (HC) at 30 ps after the initial  $T_{lattice}$  is established, HC together with the emission of 300 ions and 800 ions again at the same time. (b) Temporal evolution of glass temperature for different spherical shells surrounding the NP ( $R = 15$  nm) for the above case of 800 ions + HC.

On the other hand, one can estimate from the above mentioned Boltzmann distribution that 400 keV of energy will be taken out from the NP if approximately 300 ions are emitted by a single pulse irradiation. This energy corresponds around



20% of the absorbed laser pulse energy, which is transferred to a broad volume of glass by the ions within a short time. The radial temperature distribution of the NP-glass system for this case of ion emissions is given by the dash-dotted curve of Fig. 5.17(a), again at a time of 30 ps after the maximum  $T_{lattice}$  is established. Comparing with the case of the pure heat conduction, it is clearly seen that ion emissions cool down the NP and heat up the glass much more effectively.

In this context, it is reasonable to expect that the temperature values of the glass matrix will depend strongly on the number of emitted ions  $N$ . As an illustration, we consider a stronger laser irradiation case that triggers higher number of ion emissions from the NP. It is estimated, for instance, that 50% of the absorbed laser pulse energy is taken out from the NP when 800 ions are emitted into the glass. The radial temperature distribution in the glass for this case [the solid curve starting from 1000 K in Fig. 5.17(a)] shows that the NP loses half of its temperature, and the glass a few nm away from the NP surface reaches transiently higher temperatures than the NP itself. It is observed that a broad spherical zone of glass, up to 10 nm from the NP surface, is heated within a very short time owing to the high number of emitted ions.

Figure 5.17(b) shows the temporal evolution of glass temperatures in different spherical radii away from the center of the NP for the case of 800 ion emissions with heat conduction. The temperature of the glass at  $R = 16$  and 17 nm are observed to have high temperature values for short times because of the accumulation of a high number of emitted ions around these spherical shells. The temperature values decrease as the heat diffuses deep in the glass over time. The glass temperatures at  $R = 18$  and 19 nm start from lower values, as comparably less number of ions are located there. It is observed that these shells reach their maximum temperature values later in time as the heat from inner shells arrives.

Summarizing this part we can say that ion emissions are fast cooling mechanisms for the NP and they extend the heated glass volume considerably compared with the ordinary heat conduction. The temperatures of the glass 3 nm around the NP surface exceed the glass transition temperature of  $\approx 850$  K for the first 100 ps of time interval. This enables the softening of the glass, which is indeed necessary for the NP shape transformations to take place.

### 5.3.2. Irradiation of preheated samples

Here, we will show the experimental results obtained by irradiation of preheated samples.

As was discussed above, the irradiation of silver NPs by fs laser pulses leads to changes in extinction spectra and results in a splitting of the SP band of spherical Ag nanoparticles (peaked at 413 nm) into two polarization dependent bands [Fig. 5.18(a)]. The observed dichroism is associated with formation of prolate Ag NPs uniformly oriented parallel to the laser polarization (Chapter 5.1.1). The spectral gap between these SP bands is defined by the aspect ratio between the principal NP's axes.

Figure 5.18(a) shows polarized extinction spectra of a sample irradiated by 300 pulses per spot with a peak pulse intensity  $I_p = 0.8 \text{ TW/cm}^2$  at laser wavelength  $\lambda = 400 \text{ nm}$  at room temperature. In this case, the p-polarized SP band is centered at 507 nm while the s-polarization band is peaked in the UV region at 383 nm. However, irradiation of a preheated sample using the same laser parameters changes the extinction spectra [Fig. 5.18(b)]. At a temperature of 125°C, both SP bands are a little shifted towards longer wavelength and, in particular, are broadened and show considerably decreased amplitudes. A further increase of the global sample temperature to 200°C results in almost complete bleaching of the plasmon bands [solid lines in Fig. 5.18(b)]. Concomitantly, the residual SP bands are further broadened, nearly making the induced dichroism disappear. So the first important experimental finding is that already relatively low temperature increase (with respect to the glass transition temperature) dramatically changes the results of the laser-induced NP shape modification.

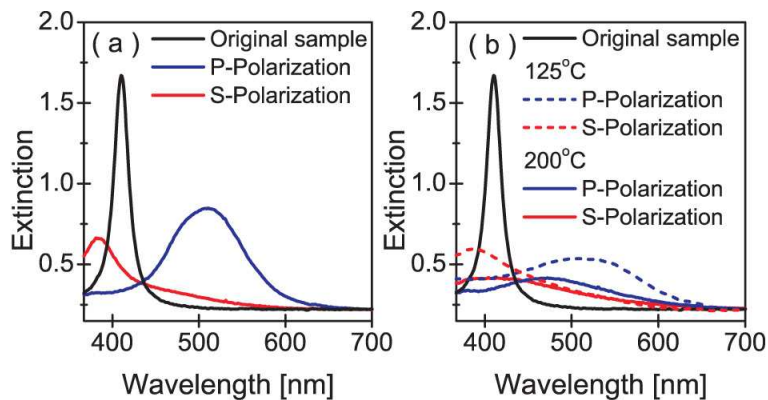


Fig. 5.18. Polarized extinction spectra of original and irradiated samples ( $\lambda=400 \text{ nm}$ , 300 pulses per spot, repetition rate 1 kHz, peak pulse intensity  $I_p = 0.8 \text{ TW/cm}^2$ ): (a) room temperature; (b) 125 and 200°C.

To better understand the influence of temperature on the laser-induced modification of Ag NPs embedded in glass, we have measured the polarized spectra of samples irradiated at various temperatures from 100°C to 170°C in steps of 5-10°C. The results in parametrized form are presented in Fig. 5.19. The spectral gap between maxima of polarized SP bands can be used as an approximate measure of the NPs' aspect ratio. The changes of the band integrals, which include the amplitudes and bandwidths changes, are directly proportional the absorption changes of the system.

Looking at Fig. 5.19(a) first, one can recognize three temperature intervals with different behaviour of the SP band center positions. In the first interval from 100°C to +80°C the positions of the bands are nearly constant at  $\approx 508 \text{ nm}$  and  $\approx 384 \text{ nm}$  for the p- and s-polarization bands, respectively. Then, towards higher temperature (here up to  $\approx 130^\circ\text{C}$ ), the p-polarized SP band occurs at a red-shifted position ( $\Delta\lambda_{max} \approx 20 \text{ nm}$ ), while almost no shift of the s-polarized band is seen. Further increase of the sample temperature leads to a blue-shift of the p-polarized band with respect to the low-temperature limit. The behavior of the band integrals is given in

Fig. 5.18(b). Here again almost no temperature dependence is observed in the above defined first interval (100°C to +80°C), similar to the behavior of the band centers. At higher temperatures >80°C, however, the band integrals of p-polarized SP bands start to decrease very rapidly, mainly due to decreasing amplitude. The amplitudes of the s-polarization bands decrease very similarly, but at temperatures above  $\approx 120^\circ\text{C}$  this effect is partially compensated by spectral broadening (compare Fig. 5.18), which results in no further decrease of the band integrals above this temperature.

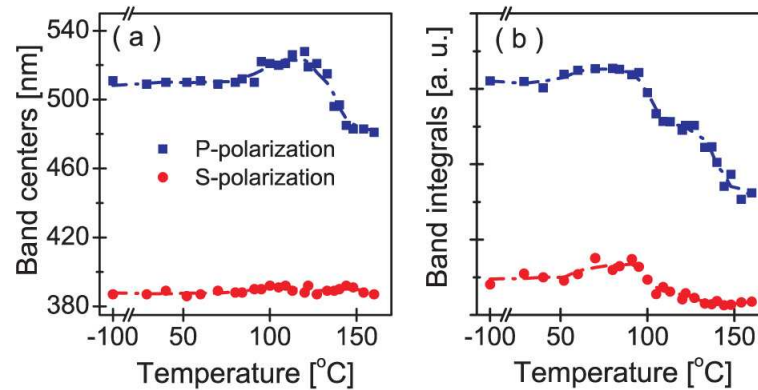


Fig. 5.19. (a) Temperature dependence of polarized extinction spectra band centers; (b) The corresponding temperature dependence of band integrals.

It should be mentioned here that we have also done similar series of irradiations with modified laser parameters (intensity and number of pulses applied); the results were comparable to those given above, i.e. the temperature dependence does not depend on the actual irradiation conditions.

### 5.3.3. Irradiation with different laser repetition rates

Behaviour analogous to the spectral changes shown in Fig. 5.19 has been observed also in a series of totally different experiments: the sample was irradiated at room temperature by fs pulses of different temporal separation, which was achieved by varying the laser repetition rate. Figure 5.20 shows selected results in parametrized form, i.e. the band centers [Fig. 5.20(a)] and the band integrals [Fig. 5.20(b)] derived from the polarized extinction spectra band as a function of laser repetition rate. In Fig. 5.20(a) it is clearly seen that increasing the laser repetition rate from 1 kHz to 10 kHz first leads to a small red shift of the p-polarized band, but for rates  $\geq 20$  kHz both polarized SP bands are shifting back towards the original band of spherical nanoparticles. The corresponding band integrals are decreasing monotonously with increasing repetition rates. At 100 kHz we have observed complete bleaching of the bands.

If we increased the writing density, i.e. the number of pulses applied on average per sample position, the observed decreases of absorption and spectral gap occurred already at lower repetition rates. For instance, doubling the writing density to

600 pulses per spot, already at  $\approx 20$  kHz repetition rate the bands were bleached so strongly that the analysis of SP bands was discouraged. Still, however, the spectra obtained by irradiation at 1 kHz were very similar to those observed for 300 pulses per spot.

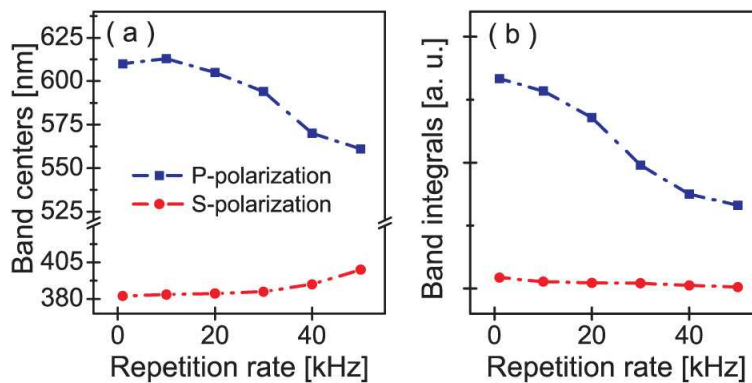


Fig. 5.20. (a) Dependence of polarized extinction spectra band centers on repetition rate; (b) The corresponding dependence of band integrals.

#### 5.3.4. Interpretation of the experimental data and summary

To find an explanation for the experimental findings of this work, we have to combine some of the proposed in Chapter 3 possible mechanisms which can lead to NP shape transformation by laser irradiation. Irradiation of nanoparticles by ultrashort laser pulses leads first to field-driven electron emission from the metal particles; these ejected electrons are trapped in the matrix (forming, e.g., color centers) close to the poles of the sphere. Then, the ionized nanoparticles can emit Ag ions in statistical directions. As the glass matrix is still cold (at ambient temperature) at this time, the mobility of silver cations will be restricted; so a dense cationic shell in the vicinity of the distorted silver NP will be formed. Within this positively charged shell, the silver cations can meet trapped electrons which are mostly concentrated at the poles. This can lead to  $\text{Ag}^+$  reduction and precipitation of silver atoms at the poles of the main particle, resulting in a prolate shape of the NP. Silver atoms which are situated relatively far away from the main nanoparticle may locally precipitate to each other forming a region of very small clusters around NP (halo).

Having in mind this (proposed, possible) picture, the effect of heating the sample before irradiation becomes obvious: for an increased matrix temperature the diffusion mobility of silver ions increases also, leading to an enlarged radius of the cationic shell. Accordingly, the concentration of silver cations in the immediate surroundings of a NP will decrease resulting in a lower precipitation rate. These processes are well-suited to understand the spectral changes observed when irradiating preheated samples.

Apparently, in the temperature range from  $-100$  to  $80^\circ\text{C}$  the ionic mobility is too low to cause significant diffusion of the emitted ions. Therefore, both the produced shapes of the nanoparticles [as an example see TEM image on Fig. 5.21(a)] and the

pertinent SP bands are fairly constant in this regime. At slightly higher temperature, i.e. in the range of 100-120°C, the optical extinction spectra start to show characteristic changes: the more prominent effect is decrease of the band integrals. This can be understood assuming that now the mobility of Ag ions has increased so far that the radius of the cationic shell grows; then consequently the precipitation rate of silver atoms or clusters to the main particle goes down, and the reduced volume of the resulting reshaped NP leads to smaller optical absorption. The second effect, moderate red shift of both polarized SPR bands, can in this case be attributed to those Ag cations which are a little further away from the main NP, but still close enough to each other to precipitate as small clusters. These clusters will form an extended halo region which, via increasing the effective refractive index around the NP, can explain the observed small red-shift (Chapter 5.1.1). Rising the temperature further, the again increased mobility of the silver cations allows them to diffuse so far away from the nanoparticle that reduction and precipitation rates are diminished more and more. Concomitantly, partial and finally total dissolution of the Ag NPs will occur instead of shape transformation to prolate spheroids. Fig. 5.21(b) proves this assumption and shows an example of partially dissolved NP. Additionally, this figure confirms that roughly 50% of the NP volume is dissolved by ion emissions after applying 300 laser pulses. These experimental findings urge us to consider the effect of ion emissions on the NP-glass system as it was introduced in section 5.3.1 [see Fig. 5.17(a) for 800 emitted ions and Fig. 5.17(b)].

Considering the above given calculations on the dynamics of heat flow, we can conclude that transient heating and cooling within a shell of 5-10 nm around the NP are crucial for the question if shape change or dissolution occurs: the results of heat conduction calculations show that, starting from  $T = 300$  K, the temperature in distances of  $\geq 6-7$  nm from the NP surface remains below 500 K at any time, while in the nearest shells of the matrix (distance from NP  $< 6-7$  nm) high temperatures up to  $>1000$  K can be reached. Apparently this situation is required to promote the NP shape transformation on one hand, but protect the nanoparticles from total dissolution on the other hand. Any change of parameters extending the spatial range around the NPs where temperatures clearly above 500K occur, at least transiently, seems to enable particle dissolution. This holds for the temperature-dependent studies in this work as well as for experiments with considerably higher laser intensity, which also resulted in partial dissolution of the NPs, as shown in Chapter 5.1.2.

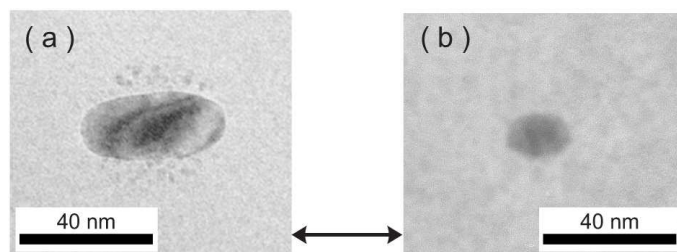


Fig. 5.21. TEM images of nanoparticles irradiated: (a) at room temperature; (b) at 150 °C. Polarization of laser light is show as an arrow.

If this picture is correct, it should also provide an explanation for the results observed by irradiation of NPs by laser pulses with different repetition rates, i.e. we have to look for a connection between the temporal separation of the laser pulses and the local sample temperature. The connection can be found considering the heat flow from the focal volume (which in beam direction is limited by the thickness of  $\approx 2 \mu\text{m}$  of the layer containing NPs) to the cold parts of the sample. The total thickness of the glass substrate is 1 mm. Using these parameters and Eq. 3.9 (equation describing heat transfer), we have calculated the temperature accumulation in the focal volume as a function of pulse repetition rate and number of pulses applied. The pertinent temperature rise  $\Delta T$  in the focal volume as a function of number of pulses is shown in Fig. 5.22(a). It is clearly seen that every pulse increases the temperature in the focal volume. Applying 300 pulses to one spot with temporal separation of 1 ms (1 kHz repetition rate) result in a temperature rise of about 50-60 K, while the same number of pulses at 100 kHz repetition rate increases the temperature by more than 300 K. Figure 5.22(b) shows the dependence on the laser repetition rate of  $\Delta T$  after 300 pulses.

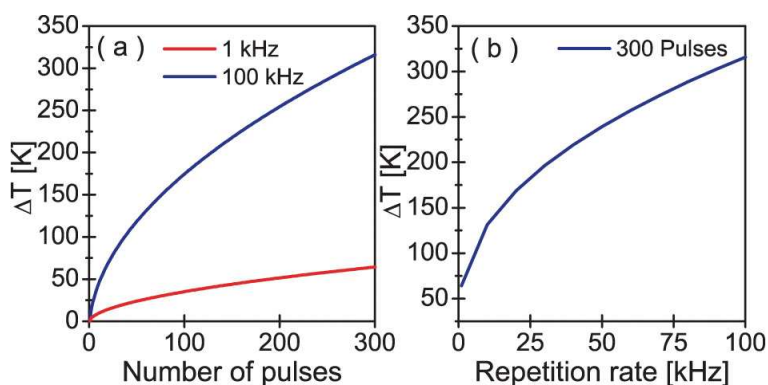


Fig. 5.22. (a) Increase of the temperature in focal volume as a function of applied number of pulses for the cases of irradiation at 1 and 100 kHz. (b) Increase of the temperature in focal volume applying 300 pulses at different repetition rates.

These simulations are in very good agreement with our experimental results: Fig. 5.22(b) tells that irradiation of nanoparticles by 300 pulses at repetition rates below 10 kHz leads to relatively small increase of temperature in the focal volume ( $< 130 \text{ K}$  for 300th pulse). As shown in Fig. 5.19 this is typically the constant temperature where NP dissolution begins. For repetition rates above 10 kHz this region of  $\Delta T > 100 \text{ K}$  is reached increasingly earlier, which should cause a reduced spectral gap and higher degree of NP dissolution. Exactly behaviour of this type is seen in the experimentally obtained dependence on the laser repetition rate shown in Fig. 5.20. Finally, also the observation that a higher number of pulses let the dissolution process appear already at lower repetition rates is nicely compatible with this calculations, since, e.g., in the case of 600 pulses the first 300 prepare a considerable temperature rise  $\Delta T$  which enables dissolution by the ‘second half’ of the pulse train.

In conclusion, in this subchapter we have investigated the thermal processes arising by interaction of intense fs laser pulses with silver nanoparticles in soda-lime glass. We used an extended three temperature model to estimate radial temperature profiles of a NP and the surrounding glass as a function of time after excitation by a laser pulse of sufficient intensity to cause NP shape transformation by successive irradiation with  $\approx 300$  pulses. Our calculations show that a single pulse causes a temperature increase exceeding  $\Delta T = 200$  K only in a limited shell of less than 7 nm distance around the NP. Experimentally, we found that irradiating samples preheated to 150-200°C results in dissolution of Ag nanoparticles and complete bleaching of SP resonance. A similar effect was observed for irradiation at room temperature at higher repetition rate, which can be explained by heat accumulation in the focal volume.

Putting all findings together, we conclude that the intended transformation of initially spherical NPs to prolate shapes with high aspect ratio by irradiation with a few hundred laser pulses requires a special spatio-temporal evolution of the matrix temperature: the heat-affected zone reaching transiently temperatures above  $\approx 500$  K around a nanoparticle should apparently be limited to a few nanometers. Then the increased mobility of emitted Ag ions enables the processes of shape transformation within that shell, while the cooler outer shells prevent the ions from drifting farther away from the NP. The latter obviously happens when the initial sample temperature lies above 100°C, which can also be reached by accumulation of the absorbed energy in the focal volume applying high laser repetition rates. In this case the emitted Ag cations seem to drift so far away from the NP that they can not diffuse back to a NP and recombine with it, but rather precipitate where they are, forming an enlarged halo region. This process readily explains the observed dissolution of the NPs after irradiation with some hundred fs laser pulses.

#### **5.4. Limiting factors of laser-induced dichroism in composite glasses with silver nanoparticles**

In this section, we want to point out all possible reasons, which are limiting the laser-induced dichroism in composite glasses with silver nanoparticles and lead to destruction of the last ones.

As it was shown in the previous section the main factor resulting in NPs destruction (dissolution) is the temperature of the surrounding glass matrix. Therefore, it is obvious that all processes leading to the heating of the glass make influence on the nanoparticle shape transformation and destruction.

From the results obtained by the study of intensity dependence and the calculations given above it is evident that the first factor is the intensity of the laser pulses, or more correctly, the amount of absorbed energy. Increase of this parameter leads to the rise of the shell with high temperature, which in turn, results in enlarged radius of cationic shell and following dissolution. It should be mentioned here, that this argument is correct only in multi-shot, relatively low intensity case. The high intensity, single shot mode will be considered in the next chapter.

It is also known that the irradiation of the composite glasses with nanoparticles leads to the formation of many different “colour centers” and defects in the glass, such as trapped electrons and holes [5.14], silver ions and small positively charged silver clusters [5.14, 5.17], as well as the neutral clusters and very small particles (halo) [5.10, 5.14, 5.18, 5.22] etc. All of them, in principal, have the absorption bands in the UV and visible regions [5.4, 5.14, 5.27], as a result they can absorb the irradiation laser light and thereby heat the glass matrix. To find the most critical one (or at least to exclude some of them) we performed the following experiment. The sample was irradiated by the pulses at 600 nm having such intensity that applying 1000 pulses the maximal dichroism is observed [Fig. 5.23(a), green curve], while 2000 pulses lead already to the partial destruction of the NPs [Fig. 5.23(a), black curve]. Then, the area, which was irradiated by 1000 pulses, was again exposed to irradiation by 1000 pulses. So, one can say that this area was irradiated with the same parameters like the second area with partial destruction of nanoparticles. However, the measured spectrum shows that further elongation is present, the band is little bit more red-shifted [Fig. 5.23(a), red curve]. Increasing the time between irradiations (1000+1000 pulses) to 180 min resulted in an even larger shape transformation [Fig. 5.23(a), blue curve]. Therefore, one can conclude that these defects, which lead to destruction of NPs, are not stable and disappearing in the time. To determine the time, in which it is happening, we have measured the extinction spectra in different time after irradiation [Fig. 5.23(b)]. It is seen that the spectra are not changing so much, however carefully looking to the maximum of SP band one can see that the amplitude of the band is increasing and SPR is little moving to the blue. After ~1 h we have not observed any difference in spectra. Therefore, because of the much longer “life” time of the silver ions and small clusters we can exclude them from the list of the main factors leading to destruction (dissolution) of nanoparticles.

Additionally, it should be noted here that the shorter time annealing of the sample at 200-400°C also remove these meta-stable defects [5.17] and the following irradiation dose not lead to destruction of nanoparticles.

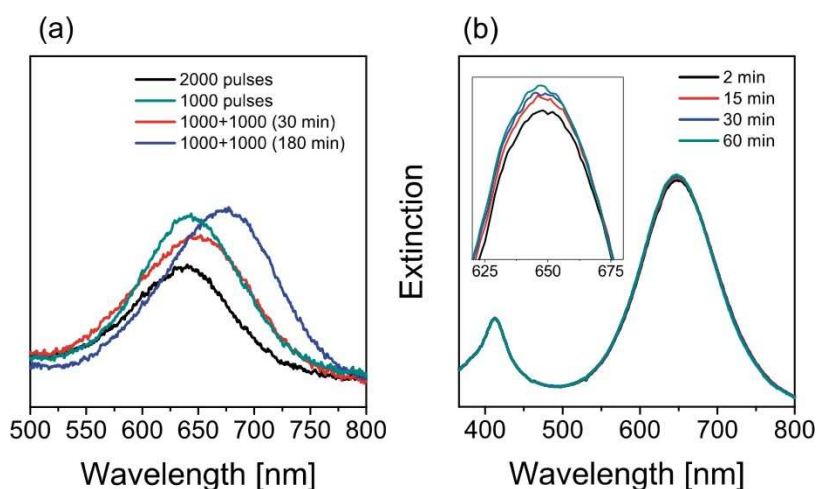


Fig. 5.23. (a) P-polarized extinction spectra of the samples irradiated by the pulses at 600 nm under different irradiation conditions (see text). (b) P-polarized extinction spectra measured in different time after irradiation.



At the end of this section, we want to consider one additional factor, which also limits the laser induced dichroism in composite glass with silver nanoparticles, namely, the directional ionisation of NPs. It is obvious that if the ejection of electrons will be isotropic, then the elongation of nanoparticles is impossible. Such a case can take place when the electric field will not enhance the hot electrons to fly in the direction of the laser polarisation. As it was already briefly discussed, the EFE factor depends on the wavelength (Chapter 3.5.2). For the case of (prolate) spheroids, the spectrum of EFE factor shifts to the red region (Fig. 3.10) like SPR. Therefore, when the wavelength of irradiation is lying in the blue wing of electric field enhancement band, then the coupling of them damps dramatically by the following elongation of nanoparticle; and at the end (when EFE factor is very small at the laser wavelength), it results in the strong quenching of the directional ionisation. As one could see from the results in our case, the elongation of nanoparticles always stops, when the wavelength of irradiation is lying in the blue wing of SPR (EFE). Therefore, it allows us to conclude that the very weak electric field enhancement at a wavelength of irradiation can be the main factor limiting the laser-induced dichroism.

## **5.5. Mechanism of the anisotropic shape modifications of spherical Ag nanoparticles in soda-lime glass upon fs laser irradiation**

The aim of this last section of the current chapter is to summarize experimental data and to propose the mechanism of the SP assisted shape modifications of spherical Ag nanoparticles embedded in soda-lime glass by excitation with intense ultra-shot laser pulses. Performed investigations of the effects accompanying the anisotropic modifications in the composite glass allow us to manifest the following experimental facts:

- The laser assisted modifications occur only by appropriate laser pulse intensity (higher than 0.2-0.3 TW/cm<sup>2</sup> by excitation at 400 nm);
- The shape of transformed silver particle (prolate or oblate) is defined by the laser pulse intensity used for irradiation; the number of laser pulses plays mostly accumulative role;
- The anisotropic shape modifications are strongly correlated with the laser polarisation indicating obviously that the processes, which define a preferable orientation of the nanoparticles, should occur at time scales about of the laser pulse duration. Therefore, one can suggest that the main process responsible for the NPs shape have to be the directed (pulse-enhanced) electron emission from nanoparticle;
- Fading and following total disappearance of the SP band in extinction spectra at higher peak pulse intensities or high number of pulses indicate that the partial destruction or dissolution of silver NPs is involved in modification mechanism;
- Modification of the NPs shape stops when the wavelength of irradiation is lying in the blue wing of SPR (EFE). However, subsequent irradiation by the

pulses at longer wavelength (or simultaneous two wavelengths irradiation) leads to the further shape transformation. All these findings allow us to presume that the electric field enhancement determines the directional ionisation and plays a key role in a mechanism of NPs shape transformation;

- Positive charged shell of the silver cation (result of ion emission) is playing apparently also a key role in the shape modifications; preheating of the sample up to 150-200°C increases the mobility of the silver cations and prevents formation of the cation shell in the vicinity of the cluster leading to total dissolution of the Ag nanoparticles upon laser irradiation.

As one can see, the experimental data testify rather complex mechanism of the fs laser assisted modifications of Ag nanoparticles incorporated in glass. Therefore, before discussion of this mechanisms leading to the different, intensity dependent shape transformations, it is useful to briefly remind the physical processes, which can occur by the interaction of the laser light with nanoparticles.

A first point is the temperature rise caused by one laser pulse. Following the intense and resonant laser irradiation, the energy absorbed by the nanoparticles conduction electrons causes a rapid increase in the electronic temperature. Electrons rapidly relax into a quasi-equilibrated hot electron system within several hundreds of femtoseconds [5.28, 5.29] via electron-electron scattering. After establishing a thermal electron system, the hot electrons cool down by sharing their energy with the nanoparticles lattice via electron-phonon (e-ph) couplings [5.29], thereby heating up the particle. The estimations of maximal electronic and lattice temperature, based on the 2TM (Chapter 3.3), give values in the range of  $10^4$  K for the electron system and a lattice temperature close to the vaporization temperature for bulk silver. Although the real temperature of a nanoparticle is expected to be much lower (because of the nanoparticle energy losses caused by the electron and ion emission, see Chapter 5.3.1), one can conclude that in the course of dissipation of the absorbed laser energy the nanoparticles and as a result its immediate surroundings experience a strong transient 'temperature' increase, which is at least connected with strongly enhanced local mobility of electrons, ions and atoms.

Another important effect is the photoionization of the silver nanoparticles during exposure to intense fs laser pulses. The physical idea is that the SPR enhances the electric field of the laser pulse close to an Ag particle by a few orders of magnitude, with the highest fields located at the poles (with respect to laser polarization) of the nanospheres [5.15]. This can lead to enhanced directed already hot electron emission from the particle surface [5.30, 5.31], preferentially parallel to the laser polarization. But also an isotropic, thermal electron emission has to be regarded in the time of the electron-phonon system thermalization. The anisotropy of the direct, laser-driven electron ejection is thought to provide the preferential direction for the following particle shape transformation. Possibly the high electric field in the vicinity of the metal nanoparticle can even exceed the breakdown threshold of glass resulting in high-density electron plasma formation and even ablation of the glass matrix on the poles of the nanosphere. Regardless whether this happens, the free electrons in the matrix will lead to formation of colour centers (trapped electrons) in the surroundings of the Ag nanoparticle [5.17], which should also play an important role for the particle shape modifications. The free electrons as well as the colour centers

have strong absorption at SP resonance [5.14] which might result in resonant coupling of SP oscillations to the matrix [5.32]. Finally, the ionized positively charged core of the Ag nanoparticles is unstable and the Coulomb forces will eject silver cations, which form a cationic shell in the vicinity of the nanoparticle [5.17]. Clearly the radius of such a cationic shell is determined by the diffusion length of the silver cations and thus strongly depends on the local temperature.

All the effects mentioned above are transient phenomena which are controlled either directly by the electric field of the laser pulse or indirectly by the temperature rise induced by it. Thus the pulse intensity is doubtless the decisive parameter for the shape transformation of the metal nanoparticles, and it is obvious to assume that the prevalence of individual processes, due to their different intensity dependence, leads to the characteristic intensity regions found in Chapter 5.1.2. Based on these qualitative conclusions and the experimental results presented above, we suggest the following mechanisms to be mainly responsible for the different shape transformation of silver nanoparticles in soda-lime glass in the different intensity regions.

In the low intensity region (i.e. between  $I_1 \approx 0.2 \text{ TW/cm}^2$  and  $I_2 \approx 2 \text{ TW/cm}^2$  in Chapter 5.1.2) SP field enhancement stimulates the fastest process, field-driven electron emission from the surface of the metal particles [Fig. 5.24(a)]. The emission process happens within a few fs [5.33], i.e. without delay against the laser pulse. The ejected electrons will then be trapped in the matrix forming colour centers close to the poles of the sphere (for linear polarized pulses). The ionized nanoparticles are likely to emit Ag ions in statistical directions, in particular when after a few picoseconds electron thermalization and heat transfer to the silver lattice is finished. The resulting positively charged shell of silver cations [5.17] around the particle meets trapped electrons which are mostly concentrated at the poles. After some picoseconds they can recombine to Ag atoms [Fig. 5.24(b)] which finally diffuse back to the nanoparticle and precipitate mainly at the poles. Silver atoms which are situated relatively far away from the main nanoparticle can locally precipitate to each other forming very small clusters (halo). In multi-shot mode, remaining silver ions may also act as trapping centers for the electrons being emitted by the next laser pulse [Fig. 5.24(c)]. Possibly also the fact that electrons are favourably being trapped close to the poles, while ions which are mostly concentrated around equator (because the purely thermal emission of electrons leads to less electrons available for ion annihilation there), may cause local electric field distributions which influence the directional properties of electron and ion emission for following laser pulses. All these processes lead obviously to a step-by-step growth of the Ag particles along the laser polarization, explaining the observed prolate spheroidal shape [Fig. 5.24(d)]. Especially, in the growing process most of the very small silver clusters having precipitated above the poles (defined by the laser polarization) become closer to the main nanoparticle and can be incorporated in it again, while the clusters situated around equator contribute only to the halo formation [5.18]. At the same time, it is obvious that in the case of circular polarization the rotating electric field should lead to precipitation around the equator of a NP rather than at the (no longer defined) poles and the halo is forming in perpendicular direction (direction of propagation).

With increasing peak pulse intensity we expect higher temperature, thus larger radius of the cationic shell. In this case, the farthest clusters located even in direction of

laser polarization can not diffuse back to the main nanoparticle, and in consequence a larger halo region is observed. This is perfectly compatible with the observed intensity dependence: from typically  $1.5 \text{ TW/cm}^2$  on, we observed decreasing dichroism and increasing isotropic red-shift, which can be attributed to the growing influence of the halo (via refractive index increase). It should be mentioned that all the processes discussed require the presence of a rigid, ionic matrix. This may explain why up to now the laser-induced transformation of metal nanoparticles has only been observed in glass nanocomposites.

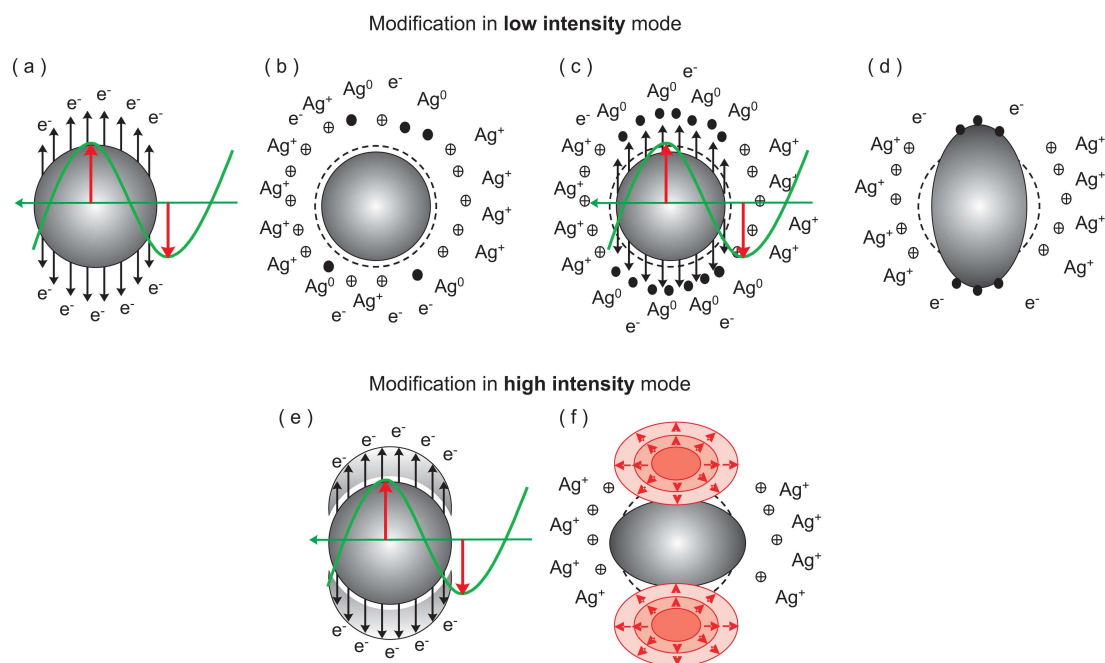


Fig. 5.24. Laser assisted shape transformation of the metal nanospheres in the case of irradiation by linearly polarized laser pulses.

For the high intensity range (above  $2 \text{ TW/cm}^2$ , Chapter 5.1.2) we suggest that, in addition to the processes already discussed, the very high local electric field at the poles of the sphere along the laser polarization can accelerate the free electrons so strongly that they induce a high density plasma by avalanche ionization of the glass [Fig. 5.24(e)]. The following plasma relaxation transfers energy from electrons to the lattice (e-ph interaction) on a time scale much faster than the thermal diffusion time. This can finally result in ablation of the material on the interface between glass and metal inclusion leading to partial destruction of the nanoparticle on the poles [Fig. 5.24(f)], or direct emission of the plasma components further away into the matrix. In any case that process produces oblate rather than prolate particle shapes (for linear polarization). It seems very plausible to anticipate that the characteristic intensity producing isotropic spectral changes only ( $I_2 \approx 2 \text{ TW/cm}^2$ ) marks the balance between (i) the processes leading to particle growth along the laser polarization and (ii) the beginning plasma formation at the particle / matrix interface counteracting this growth.

In conclusion, in this section we discussed possible mechanism of the laser induced shape modifications of spherical Ag nanoparticles embedded in soda-lime glass. The main point of the proposed scenario is the SP assisted (field-driven) photoelectron emission of the electrons from the metal surface upon excitation with 150 fs laser pulses. The following development of the processes strongly depends on the applied laser pulse intensity: slightly above the modification threshold the Coulomb explosion and anisotropic ripening of the Ag nanoparticles results in shape transformation of the particles parallel to the laser polarisation; intense laser pulses evoke the dense electron plasma on the glass-metal interface, which leads to ablation and compression of silver nanosphere resulting in orientation of the NP perpendicular to the laser polarisation.



## **Chapter 6. Towards the production of sub-micron polarizing structures**

As it was shown in previous chapters the shapes of the initially spherical Ag NPs in glass can be permanently modified by femtosecond laser irradiation; that in turn leads to the optical dichroism induced in the composite glass. The amount of dichroism (spectral gap between the two polarized resonances), being correlated with the aspect ratio (ratio of long and short axis) of the NPs, depends on the irradiation parameters such as wavelength, peak intensity and number of laser pulses applied. Varying these parameters, quite different optical dichroism can be achieved, which lets this technique of ultrashort laser pulse irradiation appear as very attractive for the production of polarization and wavelength selective micro-devices. To achieve considerably high polarization contrast for such polarizing elements, the total extinction of the shape-transformed NPs must be correspondingly high. This obviously requires the initial nanocomposite materials to have high concentration of NPs. So far, however, it has not been studied systematically how the shape transformation and the resulting optical properties behave as a function of increasing NP content.

Therefore, in the first section of this chapter we will present a detailed analysis of the influence of NP concentration on the optical properties of composite materials after irradiation. Based on the findings of this analysis, we propose a modified technique of several repeated irradiation and annealing steps, which enables the production of high polarization contrast polarizers using initial glass-metal nanocomposites containing spherical NPs with high volume filling factor.

And in the second section, the examples of (sub)micro-polarizing structures will be presented. Such structures open up the possibility of production of micro-devices, where the wavelength and polarization of the light is important. As an example, it can be used in spectrometers that will allow getting not only the spectrum of transmitted (reflected) light, but also information about the polarization of the light at each wavelength.

### **6.1. Influence of nanoparticles concentration on laser-induced dichroism in composite glasses**

The first goal of this work is to understand how the laser-induced shape transformation of Ag nanoparticles and the resulting spectral gap between polarized

SP bands depend on the volume content of the NPs. The aforementioned theoretical considerations (Chapter 2.2) suggest a slight decrease of absorption, and increase of reflectivity at 400 nm (wavelength of irradiation) towards higher filling factor. These effects alone would imply that the interaction of light with the silver NPs is somewhat stronger in samples with lower filling factor, which should lead to larger separation between S- and P-Polarized SP bands [6.1]. Taking into account the measured gradient of Ag content (Chapter 4.1), one would anticipate an – at least slightly – larger dichroism in deeper sample layers along with the decrease of filling factor. However, it is also obvious that because of the absorption by nanoparticles located in the upper layers (close to the surface), the laser pulse energy is decreasing on its way in the depth of the sample. Hence, NPs situated in deeper layers will be exposed to considerably weaker pulses resulting in less effective shape transformation and thus smaller separation between polarized SP bands.

To clarify which process is dominating, we prepared a sample by pre-etching, to have a limited maximum absorption, approximately as in case (iii) shown in Fig. 4.2, then we irradiated it for maximum dichroism, and finally removed the upper layers of that sample successively by the etching procedure described in chapter 4.1. After each etching step, the polarized transmission spectra and a reference spectrum from a non-irradiated area on the sample were recorded. The position of the transmission minima of the latter can be used as a measure for the average filling factor in the respective depth. The resulting spectra directly after irradiation and after the first etching are presented in Fig. 6.1. It is seen that after etching the amplitudes of both SP bands decrease by 7-10%. This fading of the absorption bands is expected due to the decrease of thickness of the NP-containing layer; the same effect was already shown before for spherical nanoparticles [Fig. 4.2(b)]. However, the positions of SP bands are also changed. The p-polarization band shifts by roughly 6 nm to shorter wavelengths (peak at 494 nm), while the central wavelength of the s-polarization band shifts by a smaller amount of  $\approx 1$  nm to the red.

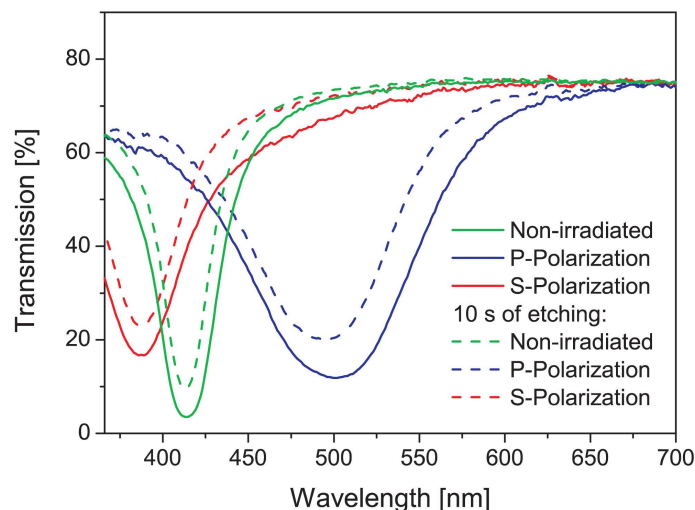


Fig. 6.1. Polarized transmission spectra of irradiated samples. The spectra were measured from the same irradiated area: solid lines – directly after irradiation; dashed lines – after 10 s of etching.



To make the complete series of data better visible, we show in Fig. 6.2 only the values of band centers for p- and s-polarization (solid squares and circles, respectively), and the band integrals for p-polarization (open rhombs); the latter was normalized by the integrals of the SP bands from the non-irradiated regions. For comparison, also the peak transmission value of the reference band is given (triangles). Clearly the spectral gap between s- and p-polarized bands decreases with increasing time of etching, mainly due to the blue-shift of the p-polarized band. Removing the upper layers until the reference SP band has a minimum transmission of  $\approx 26\%$  shift the central wavelength of the p-polarized band from 500 to 480 nm, while the changes for s-polarized band are less than 5 nm. The p-polarized band integrals are observed to be more or less constant. From these results we can conclude that the decrease of laser pulse intensity upon travelling through the particle layer has the dominant influence on the magnitude of NP shape transformation.

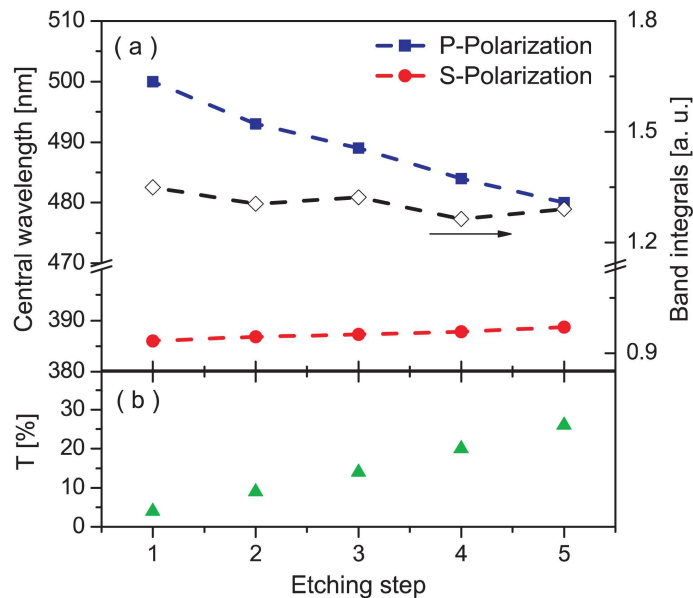


Fig. 6.2. (a) SP band positions and p-polarization band integrals of irradiated sample measured after different times of etching; (b) the values of sample transmission minima from a non-irradiated area after every etching.

To investigate the influence of the volume filling factor separately, we had to use a different approach: we prepared 6 samples with different concentration of nanoparticles and irradiated them all with the same laser parameters. The initial transmission spectra of these samples are those presented in the inset of Fig. 4.2(b). The behaviour of the same parameters as discussed in Fig. 6.2 is illustrated in Fig. 6.3. As one can see, the p-polarization band for the sample with highest filling factor is peaked at 501 nm, while the central wavelength of the s-polarized SP band is located around 386 nm. For the next two samples with lower NP concentration the distance between polarized bands increases a little. However, for the next three samples with successively lower Ag filling factor, the spectral gap and band integrals decrease considerably.

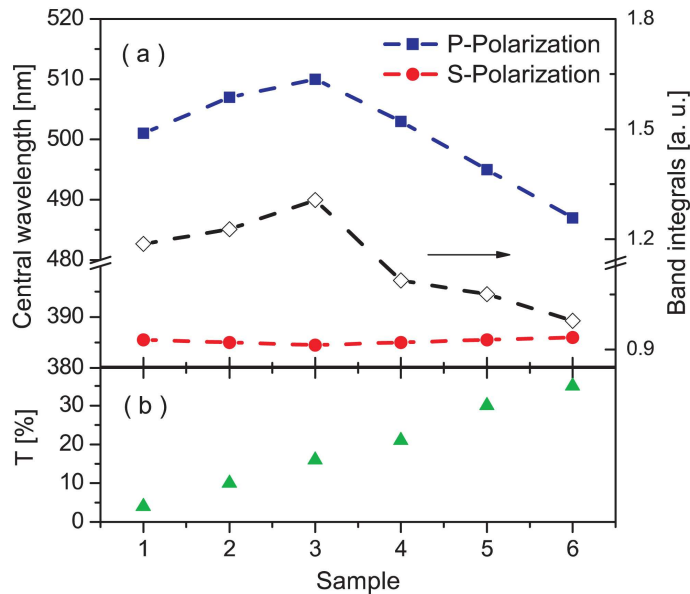


Fig. 6.3. (a) The central wavelengths of polarized SP bands and p-polarization band integrals for six samples having different filling factors and irradiated with the same laser parameters; (b) the values of sample transmission minima from non-irradiated areas.

The last finding is in contrast to the expectation from Maxwell Garnett theory (Chapter 2.2), where we predicted a stronger laser – NP interaction and thus an increase of the spectral gap between polarized SP bands for decreasing fill factor. However, as it was shown above, the laser induced shape transformation of NPs is limited. When the highest aspect ratio of nanoparticles is achieved, a further increase of interaction strength between laser light and NP leads to their partial destruction. Spectroscopically this destruction is seen in the transmission spectra as a shift of both polarized SP bands back towards the original band, accompanied by bleaching and broadening [see for example Fig. 5.7(c)].

Collecting all arguments given above, we can describe the observed results as follows. Since the laser irradiation parameters were the same for all samples, the behaviour of the spectra demonstrated in Fig. 6.3 is obviously due to the changes in absorption (and/or reflection) caused by changes of the NPs' filling factor. For the first three samples (highest concentrations of nanoparticles) the increase of absorption in fact leads to the expected higher aspect ratios of NPs, enlarging also the spectral gap between the polarized SP bands. For the three samples with lower filling factor the interaction strength between laser pulses and NPs is becoming too high that results in a partial destruction of the nanoparticles, which is seen as decrease of dichroism with simultaneous bleaching of SP bands.

Overall, the results discussed so far make clear that irradiating composite glasses with high content of metal NPs with the goal to achieve a good dichroism with the high polarization contrast is a difficult task. On one hand, the laser pulses should be strong enough to modify the nanoparticles in deeper layers; on the other hand, too

high intensity irradiation leads to partial destruction of NPs. However, we have found that this destruction can be annulled or at least reduced utilizing repeated irradiation, where the sample is heated for 1 h at 200°C between subsequent irradiations. This annealing of the sample removes colour centers and other meta-stable laser-induced defects in the glass [6.2], which otherwise would absorb part of the laser pulse energy [6.3], thereby heat the sample, increasing the mobility of electrons and silver ions, and as a result lead to dissolution of NPs [6.4]. At the same time, because of successive particle deformation the SP band polarized along the laser polarization moves out of resonance decreasing the NPs interaction with the laser pulses. By combination of these two processes (reduction of meta-stable defects and shift of the p-polarized band out of resonance) the destruction of nanoparticles in the upper layers is strongly reduced, while the average energy interacting with the NPs located in deeper layers increases. The resulting effect is illustrated by Fig. 6.4, which shows polarized transmission spectra of a sample with high filling factor measured after only one and after six successive irradiations (from both sides of the sample): after the first irradiation the p-polarization band is only shifted to center wavelength < 450 nm, while repeated irradiations and heating the sample in between causes a much larger spectral gap.

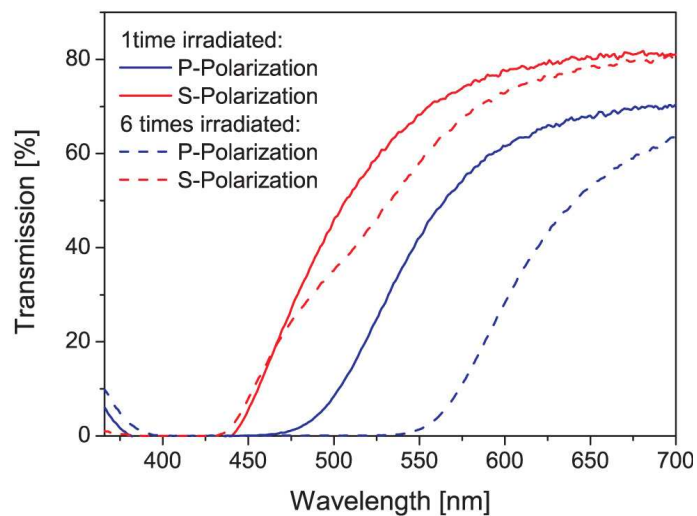


Fig. 6.4. Polarized transmission spectra of irradiated sample having high filling factor: (solid lines) – measured after first irradiation; (dashed lines) – measured after sixth irradiation.

Finally we can make use of the finding that multi-wavelength irradiation of the same sample area by pulses with successively longer wavelengths (as it was shown in Chapter 5.2.2 and Ref. 6.5, 6.6) can shift the p-polarized band much farther leading to considerably increased dichroism or high polarization contrast, respectively. As an example, Fig. 6.5 shows polarized transmission spectra of the same sample as already discussed in Fig. 6.4. After the first irradiation series at a wavelength of 400 nm, a second irradiation step at 550 nm, with polarization parallel to the long axis of the already modified particles, was performed. Clearly the p-polarized band

shifts further to a peak position of 600 nm, resulting in high polarization contrast at this wavelength: in the region of 550-650 nm, the transmission for p-polarized light is close to zero, while for s-polarization it is around 60%. It should be mentioned here also that we have tested the effect of further irradiation steps at longer wavelength (e.g. 800 nm), which shift the p-polarized SP band further into the IR region; because of the minimal losses for s-polarized light, these subsequent irradiation also increase the polarization contrast further.

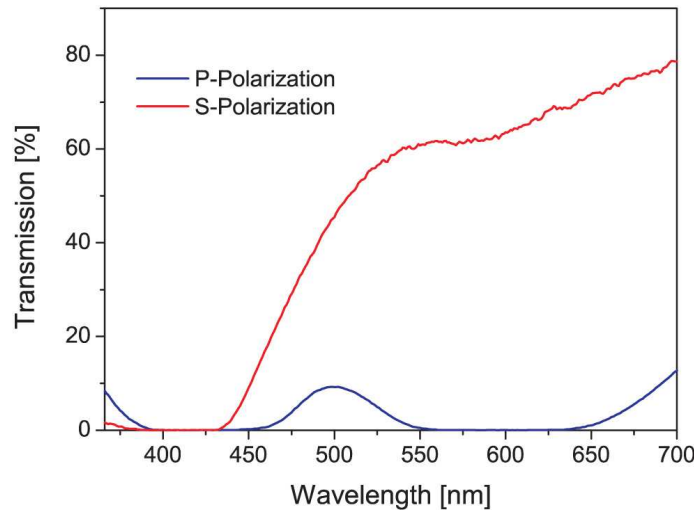


Fig. 6.5. Polarized transmission spectra of the sample having high filling factor subsequently irradiated by pulses at 400 and 550 nm.

## 6.2. Micro-polarized matrixes

Considering all observations discussed above, we have tried to produce micro-polarizing structures on the nanocomposite glass containing silver nanoparticles. To achieve spots with the size of few micrometers requires focusing with sufficiently high numerical aperture. In this experiment the beam size was enlarged to 15 mm and then focused with lenses with 55 or 80 mm focal length, respectively. We have irradiated the sample by pulses at  $\lambda = 515$  nm; the laser parameters were chosen so that the maximum dichroism is obtained. The result of irradiation is presented in Fig. 6.6. The matrix consists of spots (modified area) with a size of around  $3 \mu\text{m}$  and a distance of  $15 \mu\text{m}$  between them. The spots are seen when polarization of the light (in microscope) is parallel to the laser polarization. If the light is polarized perpendicularly to the laser polarization, the spots disappear. The irradiated areas have a green colour in p-polarisation because of extinction at around 600 nm [see for example Fig. 5.10].

The next example is shown in Fig. 6.7. Here, again parameters of irradiation were the same for every spot. However, the pattern of the structure, in this case, consists of three irradiated and one non-irradiated spots (Fig. 6.7 marked by red square) and the laser polarization is rotated on  $45^\circ$  and  $90^\circ$  for every next irradiated spot in pattern. The four photos shown in Fig. 6.7 are taken from the same area on the sample. The

only difference is the polarization of light in the microscope, which for every case is shown as an arrow. The colour of the spots is darker than in previous case, because the irradiated sample had a higher filling factor, which leads to the broader extinction (see for example Fig. 6.5).

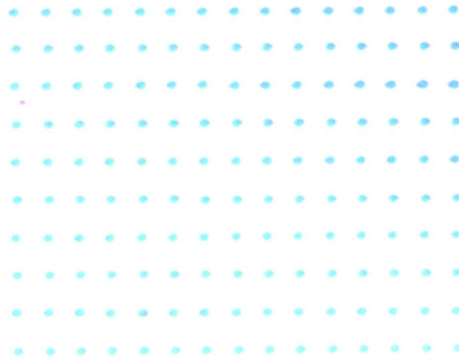


Fig. 6.6. Polarized matrix made by laser irradiation of silver nanoparticles embedded in glass. Polarization of the light is parallel to the laser polarization. If the light is polarized perpendicularly to the laser polarization, the spots are disappearing. The size of one spot is around  $3 \mu\text{m}$ .

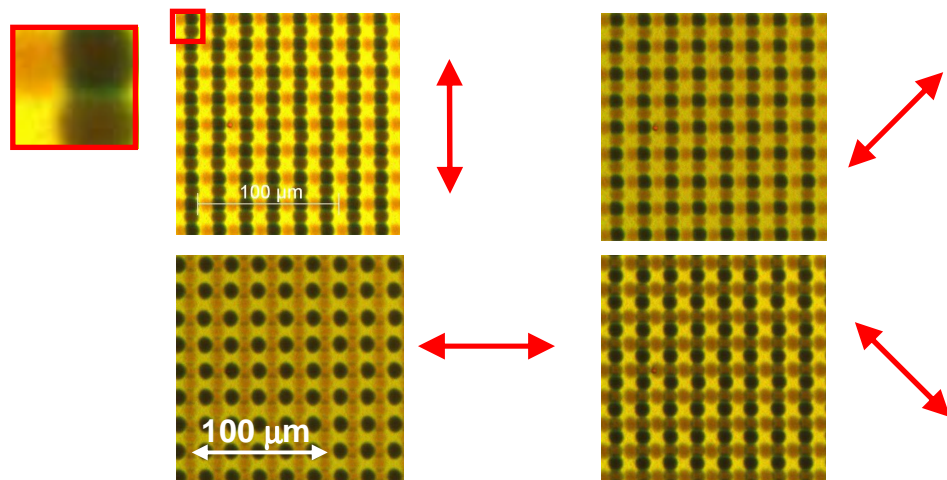


Fig. 6.7. Polarized microstructure made by laser irradiation of silver nanoparticles embedded in glass. Parameters of irradiation (except laser polarization) are the same for every spot. The pattern of the structure (marked by red quadrat) consists of three spots irradiated with laser polarization rotated on  $45^\circ$  for every next spot and one non-irradiated area. Polarization of the light in microscope is shown as an arrow.

The last example presented in Fig. 6.8 shows similar structure as was shown in Fig. 6.7. Again, the pattern consists of three irradiated and one non-irradiated spots and the laser polarization is rotated on  $45^\circ$  and  $90^\circ$  for every next irradiated spot in pattern. However, in this case parameters of irradiation for every spot were different.

The rise in number of pulses leads to the red shift of p-polarized SP band and as a result the colour is changed from brown to green (Chapter 5.1.2). On the other hand, rotation of the probe light polarization leads to the changes of spots' colours, so that the spot which has red colour in one polarization becomes yellow-brown for the light polarized in perpendicular direction.

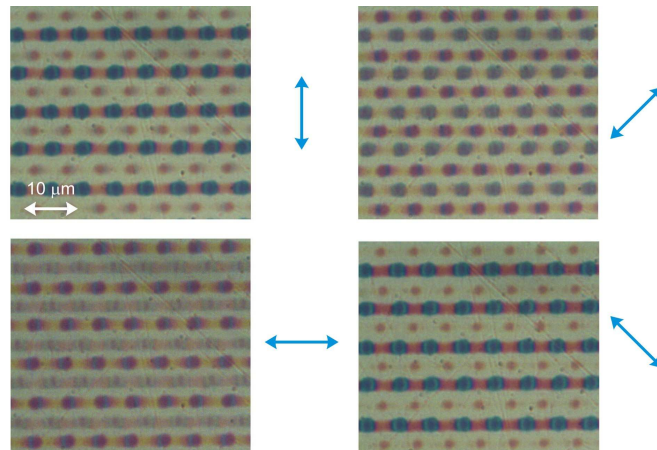


Fig. 6.8. Polarized microstructure made by laser irradiation of silver nanoparticles embedded in glass. Parameters of irradiation are different for every spot in the pattern. The pattern of the structure again consists of three spots irradiated with laser polarization rotated on  $45^\circ$  for every next spot and one non-irradiated area. Polarization of the light in microscope is shown as an arrow.

### 6.3. Summary

In this chapter we presented first a detailed study on the question, how polarizing areas with large dichroism and high polarization contrast can best be prepared with the method of laser-induced shape transformation of metal nanoparticles at high concentration in glass. Several experiments were employed to understand the limiting factors on the observed amount of dichroism in this case. The obtained experimental results showed that the glasses with silver NPs with high volume fraction behave different compared with the samples with low metal content. Namely, it was shown that the rise of NPs concentration results in decrease of interaction strength between NP and laser pulses (400 nm). Furthermore, the absorption of the laser light by NPs located in upper layers prevents the shape modification of nanoparticles in deeper layers. Comprising these and previous findings, we identified that a multiple irradiation procedure with increasing wavelength, interrupted by annealing in between two irradiation cycles is the best method to achieve large dichroism and high polarization constant in composite glasses with silver nanoparticles. Such technique permits production of micro-polarizing structures in visible and near IR spectral regions. At the end, we have shown few examples of such micro-polarizing structures (with the spot size of about  $3 \mu\text{m}$ ) made by laser irradiation on nanocomposite glass with silver nanoparticles, which can be used in polarization and wavelength selective micro-devices.

## Chapter 7. Summary of the work

The experimental results presented in this thesis are mostly concentrated on the investigation of the laser-induced shape modification of initially spherical silver nanoparticles incorporated in glass and the processes leading to the different NPs shapes. A detailed understanding of all these processes helps to optimize the technique of NPs shape transformation based on laser irradiation, and as a result, to modify the optical properties of composite glasses with metal nanoparticles as it is needed for every special application.

At the first, the dependence of the nanoparticles shapes on the laser polarization was studied. It was found, that irradiation of the NPs by the laser pulses with circular polarization leads to the transformation of initially spherical particles to oblate spheroids with the symmetry axis parallel to the propagation direction. In the case of linearly polarized light, however, the NPs shape can be modified to either prolate or oblate spheroid with symmetry axis parallel to the laser polarization. The shape in this case is defined by the laser peak pulse intensity used for irradiation. Pulse intensities slightly above the modification threshold lead to elongation of the silver nanoparticle parallel to the laser polarization (prolate spheroid). On the other hand, increase in the peak pulse intensity in one order of magnitude results in oblate spheroids, but in this case, with the short axis parallel to the laser polarization. These results allowed us to conclude that the main process responsible for the different NPs shape transformation is the directional photoionization.

We have also found that laser induced shape transformation of Ag nanoparticles is strongly dependent on the wavelength of fs laser pulses used for irradiation. The first striking observation is that, considerably off-resonant excitation (i.e. irradiation with a laser wavelength shifted more than 100 nm to the long wavelength side of the SP resonance absorption of spherical nanoparticles (at 413 nm)) can even more effectively transform the shapes of the nanoparticles to spheroids with large aspect ratios than near resonant interaction, in spite of the very weak coupling to the SPR in this region.

The fact that the laser assisted elongation of nanoparticles stops when the excitation wavelength is located considerably far in the blue wing of the p-polarized SP band together with results obtained in experiment with simultaneous irradiation of the sample by two wavelengths allowed us to conclude that the very weak electric field enhancement at a wavelength of irradiation can be the main factor limiting the laser-induced dichroism. This limit can be overcome by subsequent irradiation tuning the irradiation pulses to the longer wavelengths.

Taking into account the theoretical estimations and experimental results observed by the study on temperature dependence we can conclude that the intended transformation of initially spherical NPs to prolate shapes with high aspect ratio by irradiation with a few hundred laser pulses requires a special spatio-temporal evolution of the matrix temperature: the heat-affected zone reaching transiently temperatures above  $\approx 500$  K around a nanoparticle should apparently be limited to a few nanometers.

According to the all acquired experimental results and calculations we also proposed the possible deformation mechanisms based on the transient phenomena which are controlled either directly by the electric field of the laser pulse or indirectly by the temperature rise induced by it. Formation of the prolate spheroids with the long axis parallel to the laser polarization in the low intensity range for multi-shot irradiation could be explained by combination of the photoionization and metal particle precipitation on the poles of the nanosphere. The intensity-dependent extension of the cationic shell around the nanoparticle and the photoelectron emission in direction of the laser polarization play a key role here. In the case of high intensities (above  $2 \text{ TW/cm}^2$ ) and low number of pulses (less than 40), dense electron plasma formation at the poles of the sphere and following thermal expansion or even ablation of the glass matrix dominate, leading to transformation of nano-spheres to oblate spheroids.

All these findings allowed us to optimize the technique of laser-induced modification of optical properties of the nanocomposite glasses with silver nanoparticles and to show that this technique is a very good tool for production of micro-polarizing structures (polarization and wavelength selective devices) with high polarization contrast and broad tunable range of dichroism; some of the examples of which were presented in Chapter 6.



## References

### Chapter 1

- 1.1. U. Kreibig and M. Vollmer, *Optical Properties of Metal Clusters* (Springer, Berlin, 1995).
- 1.2. V.M. Shalaev, S. Kawata, *Nanophotonics with surface plasmons* (Elsevier, 2007).
- 1.3. K. L. Kelly, E. Coronado, L. L. Zhao, and G. C. Schatz, *J. of Phys. Chem. B* **107**, 668 (2003).
- 1.4. R. Jin, Y. C. Cao, E. Hao, G. S. Merraux, G. C. Schatz, C. A. Mirkin, *Nature* **425**, 487 (2003).
- 1.5. M. S. Gudiksen, L. J. Lauhon, J. Wang, D. C. Smith, C. M. Lieber, *Nature* **415**, 617 (2002).
- 1.6. P. Chakaraborty, *J. Mat. Sci.* **33**, 2235 (1998).
- 1.7. F. Gonella, P. Mazzoldi, *Handbook of Nanostructured Materials and Nanotechnology*, Vol. 4, (Academic Press, San Diego, 2000).
- 1.8. G. Seifert, M. Kaempfe, K.-J. Berg, H. Graener, *Appl. Phys. B.* **73**, 355 (2001).
- 1.9. J. R. Krenn, *Nature Mater.* **2**, 210 (2003).
- 1.10. S. A. Maier, P. R. G. Kik, H. A. Atwater, S. Meltzer, E. Harel, B. Koel, A. G. Requicha, *Nature Mater.* **2**, 229 (2003).
- 1.11. T. Wenzel, J. Bosbach, A. Goldmann, F. Stietz, F. Trager: *Appl. Phys. B* **69**, 513 (1999).
- 1.12. F. Stietz: *Appl. Phys. A* **72**, 381 (2001).
- 1.13. A. L. Stepanov, D. E. Hole, A. A. Bukharaev, P. D. Townsend, N. I. Nurgazizov, *Appl. Surf. Sci.* **136**, 298 (1998).
- 1.14. Y. Shimotsuma, T. Yuasa, H. Homma, M. Sakakura, A. Nakao, K. Miura, K. Hirao, M. Kawasaki, J. Qiu and P. G. Kazansky, *Chem. Mater.* **19**, 1206 (2007).
- 1.15. M. Kaempfe, T. Rainer K.-J. Berg, G. Seifert, H. Graener. *Appl. Phys. Lett.* **74**, 1200 (1999).
- 1.16. M. Kaempfe, G. Seifert, K.-J. Berg, H. Hofmeister H. Graener. *Eur. Phys. J. D* **16**, 237 (2001).
- 1.17. G. Seifert, M. Kaempfe, K.-J. Berg, H. Graener. *Appl. Phys. B* **73**, 355 (2001).
- 1.18. A. Podlipensky, A. Abdolvand, G. Seifert, H. Graener. *Appl. Phys. A* **80**, 1647 (2005).
- 1.19. A. V. Podlipensky, “*Laser assisted modification of optical and structural properties of composite glass with silver nanoparticles*” Ph.D. Thesis, Martin-Luther-Universität Halle-Wittenberg (2005).

Chapter 2

- 2.1. G. Mie, Ann. Phys. **330**, 377 (1908).
- 2.2. V.M. Shalaev, S. Kawata, *Nanophotonics with surface plasmons* (Elsevier, 2007).
- 2.3. M L. Brongersma, P G. Kik, *Surface Plasmon Nanophotonics* (Springer, Berlin, 2007).
- 2.4. Chakraborty, P. J. Mater. Sci. **33**, 2235 (1998).
- 2.5. J. Tominaga, D.P. Tsai, *The Manipulation of Surface and Local Plasmons*, Topics in Applied Physics (Springer, Berlin, 2003).
- 2.6. M. Righini, C. Girard, and R. Quidant, J. Opt. A: Pure Appl. Opt. **10**, 093001 (2008).
- 2.7. J. Wang, and W. J. Blau, J. Opt. A: Pure Appl. Opt. **11** 024001 (2009).
- 2.8. U. Kreibig and M. Vollmer, *Optical Properties of Metal Clusters* (Springer, Berlin, 1995).
- 2.9. V. M. Shalaev, *Optical Properties of Nanostructured Random Media* (Springer, Berlin, 2002).
- 2.10. C. F. Bohren, and D. R. Huffman, *Absorption and Scattering by Small Particles* (Wiley, New York, 1983).
- 2.11. S. A. Maier, *Plasmonics* (Springer, Berlin, 2007).
- 2.12. V. V. Kresin, Phys. Rev. B **51**, 1844 (1995).
- 2.13. K.-J. Berg, A. Berger, and H. Hofmeister, Z. Physik D **20**, 309 (1991).
- 2.14. A. Hilger, M. Tenfelde, and U. Kreibig, Appl. Phys. B **73**, 361 (2001).
- 2.15. S. Link and M. A. El-Sayed, Ann. Rev. Phys. Chem. **54**, 331 (2003).
- 2.16. S. Berciaud, L. Cognet, P. Tamarat, and B. Lounis, Nano Lett. **5**, 515 (2005).
- 2.17. M. P. Seah and W. A. Dench, Surface and Interface Analysis **1**, 1 (1979).
- 2.18. L. Genzel, T. P. Martin, and U. Kreibig, Z. Phys. B **21**, 339 (1975).
- 2.19. U. Kreibig and L. Genzel, Surface Science **156**, 678 (1985).
- 2.20. V. Amendola and M. Meneghetti, J. Phys. Chem. C **113**, 4277 (2009).
- 2.21. J. Postendorfer, “*Numerische Berechnung von Extinktions- und Streuspektren spharoidaler Metallpartikel beliebiger Größe in dielektrischer Matrix*”, Dissertation, Martin-Luther University Halle-Wittenberg, 1997.
- 2.22. N. V. Voshchinnikov, and V. G. Farafonov, Astrophys. Space Sci. **204**, 19 (1993).
- 2.23. See for example the following link: <http://www.codixx.de/>
- 2.24. C. F. Bohren, and D. R. Huffman, *Absorption and Scattering of Light by Small Particles* (Wiley, 1998).
- 2.25. J. P. Marton, and J. R. Lemon, Phys. Rev. B **4**, 271 (1971).
- 2.26. G. Xu, M. Tazawa, P. Jin, and S. Nakao, Appl. Phys. A **80**, 1535 (2005).
- 2.27. V. A. Markel, L. S. Muratov, M. I. Stockman, and T. F. George, Phys. Rev. B **43**, 8183 (1991).
- 2.28. V. A. Markel, V. Shalaev, E. B. Stechel, W. Kim, and R. L. Armstrong, Phys. Rev. B **53**, 2425 (1996).
- 2.29. B. Lamprecht, A. Leitner, and F. G. Ausseneg, Appl. Phys. B **64**, 269 (1997).

*Chapter 3*

- 3.1. J. Y. Bigot, V. Halte, J. C. Merle, and A. Daunois, *Chem. Phys.* **251**, 181 (2000).
- 3.2. S. Link and M. A. El-Sayed, *Int. Rev. Phys. Chem.* **19**, 409 (2000).
- 3.3. A. Arbouet, et al., *Phys. Rev. Lett.* **90**, 177401 (2003).
- 3.4. C. Voisin, et al., *Phys. Rev. B* **69**, 195416 (2004).
- 3.5. N. Del Fatti, C. Voisin, M. Achermann, S. Tzortzakis, D. Christofilos, and F. Vallee, *Phys. Rev. B* **61**, 16956 (2000).
- 3.6. N. Del Fatti, A. Arbouet, F. Vallee, *Appl. Phys. B* **84**, 175 (2006).
- 3.7. F. Stietz, *Appl. Phys. A* **72**, 381 (2001).
- 3.8. P. Kamat, M. Flumiani, and G. V. Hartland, *J. Phys. Chem. B* **102**, 3123 (1998).
- 3.9. W. Pfeifer, C. Kennerknecht, M. Merschdorf, *Appl. Phys. A* **78**, 1011 (2004).
- 3.10. F. Calvayrac, P. G. Reinhard, E. Suraud, and C. A. Ullrich, *Phys. Rep.* **337**, 493 (2000).
- 3.11. W. S. Fann, R. Storz, H. W. K. Tom, and J. Bokor. *Phys. Rev. Lett.* **68**, 2834 (1992).
- 3.12. W. S. Fann, R. Storz, H. W. K. Tom, and J. Bokor. *Phys. Rev. B* **46**, 13592 (1992).
- 3.13. M. Perner, P. Bost, U. Lemmer, G. von Plessen, J. Feldmann, U. Becker, M. Mennig, M. Schmitt, and H. Schmidt. *Phys. Rev. Lett.* **78**, 2192 (1997).
- 3.14. M. Aeschlimann, M. Bauer, and S. Pawlik. *Chem. Phys.* **205**, 127 (1996).
- 3.15. J. Cao, Y. Gao, H. E. Elsayed-Ali, R. J. D. Miller, and D. A. Mantell. *Phys. Rev. B* **58**, 10948, (1998).
- 3.16. E. Knoesel, A. Hoetzel, and M. Wolf. *Phys. Rev. B* **57**, 12812 (1997).
- 3.17. S. Ogawa, H. Nagano, and H. Petek. *Phys. Rev. B* **55**, 10869 (1997).
- 3.18. C. Voisin et al., *Phys. Rev. Lett.* **85**, 2200 (2000).
- 3.19. N. Del Fatti, C. Voisin, M. Achermann, S. Tzortzakis, D. Christofilos, and F. Vallee, *Phys. Rev. B* **61**, 16956 (2000).
- 3.20. C. Voisin, N. Del Fatti, D. Christofilos, and F. Vallee, *J. Phys. Chem. B* **105**, 2264 (2001).
- 3.21. J. Hodak, I. Martini, and G.V. Hartland. *Chem. Phys. Lett.* **284**, 135 (1998).
- 3.22. T. S. Ahmadi, S. L. Logunov, and M. A. El-Sayed. *J. Phys. Chem.* **100**, 8053 (1996).
- 3.23. T. W. Roberti, B. A. Smith, and J. Z. Zhang. *J. Chem. Phys.* **102**, 3860 (1995).
- 3.24. J. W. Haus, N. Kalyaniwalla, R. Inguva, M. Bloemer, and C. M. Bowden. *J. Opt. Soc. Am. B* **6**, 797 (1989).
- 3.25. K. Uchida, S. Kaneka, S. Omi, C. Hata, H. Tanji, Y. Asahara, A. J. Ikushima, T. Tokizaki, and A. Nakamara. *J. Opt. Soc. Am. B* **11**, 1236 (1994).
- 3.26. A. Stella, M. Nisoli, S. De Silvestri, O. Svelto, G. Lanzani, O. Cheyssac, and R. Kofman. *Phys. Rev. B* **53**, 15497 (1996).
- 3.27. U. Kreibig, G. Bour, A. Hilger, and M. Gartz. *Phys. stat. solid.* **175**, 351 (1999).
- 3.28. J. Y. Bigot, J. C. Merle, O. Cregut, and A. Daunois, *Phys. Rev. Lett.* **75**, 4702 (1995).
- 3.29. J. H. Hodak, I. Martini, and G.V. Hartland. *J. Phys. Chem. B* **102**, 6958 (1998).

- 3.30. S. I. Anisimov, B. L. Kapeliovich, and T. L. Perelman, Zh. Eksp. Teor. Fiz. **66**, 776 (1974) [Sov. Phys. JETP **39**, 375 (1974)].
- 3.31. O. L. Muskens, N. Del Fatti, and F. Vallee, Nano Lett. **6**, 552 (2006).
- 3.32. X. Y. Wang, D. M. Riffe, Y. S. Lee, and M. C. Downer, Phys. Rev. B **50**, 8016 (1994).
- 3.33. Z. Lin, and L. V. Zhigilei, Proc. SPIE **6261**, 62610U (2006).
- 3.34. R. Hultgren, P. D. Desai, D. T. Hawkins, M. Gleiser, K. K. Kelley, and D. D. Wagman, “*Selected Values of the Thermodynamic Properties of the Elements*” American Society for Metals, Ohio, (1973).
- 3.35. N. W. Ashcroft and N. D. Mermin, “*Solid State Physics*” Saunders College (1976).
- 3.36. M. I. Kaganov, I. M. Lifshitz, and L. V. Tanatorov, Zh. Eksp. Teor. Fiz. **31**, 232 (1956) [Sov. Phys. JETP **4**, 173 (1957)].
- 3.37. Y. Hamanaka, N. Hayashi, A. Nakamura, and S. Omi, J. Lumin. **76**, 221 (1998).
- 3.38. S. Lysenko, J. Jimenez, G. Zhang, and H. Liu, J. Elect. Mat. **35**, 1715 (2006).
- 3.39. Z. Lin, L. V. Zhigilei, and V. Celli, Phys. Rev. B **77**, 075133 (2008).
- 3.40. G. Kresse and J. Hafner, Phys. Rev. B **47**, 558 (1993); **49**, 14251 (1994).
- 3.41. American Institute of Physics Handbook, 3rd ed. McGraw-Hill, New York (1972).
- 3.42. T. S. Ahmadi, S. L. Logunov, and M. A. El-Sayed, J. Phys. Chem. **100**, 8053 (1996).
- 3.43. J. K. Hodak, I. Martini, and G. V. Hartland, J. Phys. Chem. B **102**, 6958 (1998).
- 3.44. A. Stalmashonak, A. Podlipensky, G. Seifert, and H. Graener, Appl. Phys. B **94**, 459 (2009).
- 3.45. A. Plech, V. Kotaidis, S. Gresillon, C. Dahmen, and G. von Plessen, Phys. Rev. B **70**, 195423 (2004).
- 3.46. A. Plech, V. Kotaidis, M. Lorenc, J. Boneberg, Nature Physics **2**, 44 (2006).
- 3.47. H. Inouye, K. Tanaka, I. Tanahashi, and K. Hirao, Phys. Rev. B **57**, 11334 (1998).
- 3.48. A. Plech et. al., Europhys. Lett. **61**, 762 (2003).
- 3.49. M. Hu and G. V. Hartland, J. Phys. Chem. B **106**, 7029 (2002).
- 3.50. A. Podlipensky, A. Abdolvand, G. Seifert, and H. Graener, Appl. Phys. A **80**, 1647 (2005).
- 3.51. C. B. Schaffer, “*Interaction of Femtosecond Laser Pulses with Transparent Materials*,” PhD thesis, Harvard University (2001).
- 3.52. H. A. H. Boot, and R. B. R. S. Harvie, Nature **180**, 1187 (1957).
- 3.53. L. V. Keldysh, Sov. Phys. JETP **20**, 1018 (1965).
- 3.54. V. S. Popov, Physics – Uspekhi **47**, 855 (2004).
- 3.55. U. Busolt, E. Cottancin, H. Rohr, L. Socaciu, T. Leisner, L. Woste, Eur. Phys. J D **9**, 523 (1999).
- 3.56. M. Fierz, K. Siegmann, M. Scharte, M. Aeschlimann, Appl. Phys. B **68**, 415 (1999).
- 3.57. K. Ertel, U. Kohl, J. Lehmann, M. Merschdorf, W. Pfeiffer, A. Thon, S. Voll, G. Gerber, Appl. Phys. B **68**, 439 (1999).
- 3.58. L. Koller, M. Schumacher, J. Kohn, S. Teuber, J. Tiggesbaumker, K.H. Meiwes-Broer, Phys. Rev. Lett. **82**, 3783 (1999).

- 3.59. J. Lehmann, M. Merschdorf, W. Pfeiffer, A. Thon, S. Voll, G. Gerber, Phys. Rev. Lett. **85**, 2921 (2000).
- 3.60. J. Lehmann, M. Merschdorf, W. Pfeiffer, A. Thon, S. Voll, G. Gerber, J. Chem. Phys. **112**, 5428 (2000).
- 3.61. M. Merschdorf, W. Pfeiffer, A. Thon, S. Voll, G. Gerber, Appl. Phys. A **71**, 547 (2000).
- 3.62. W. Pfeifer, C. Kennerknecht, M. Merschdorf, Appl. Phys. A **78**, 1011-1028 (2004).
- 3.63. U. Kreibig and M. Vollmer, "Optical Properties of Metal Clusters" Springer (1995).
- 3.64. A. V. Podlipensky, "Laser assisted modification of optical and structural properties of composite glass with silver nanoparticles" Ph.D. Thesis, Martin-Luther-Universität Halle-Wittenberg (2005).
- 3.65. A. Akella, T. Honda, A. Y. Liu, L. Hesselink, Opt. Lett. **22**, 967 (1997).
- 3.66. K. L. Kelly, E. Coronado, L. L. Zhao, and G. C. Schatz, J. of Phys. Chem. B **107**, 668 (2003).
- 3.67. E. Hao and G. C. Schatz, J. Chem. Phys. **120**, 357 (2004).
- 3.68. E. Hao, G. C. Schatz, and J. T. Hupp, J. Fluoresc. **14**, 331 (2004).
- 3.69. V. M. Shalaev, S. Kawata, *Nanophotonics with surface plasmons* (Elsevier, 2007).
- 3.70. W. H. Yang, G. C. Schatz, and R. P. Van Duyne, J. Chem. Phys. **103**, 869 (1995).
- 3.71. A. A. Unal, A. Stalmashonak, G. Seifert, and H. Graener, Phys. Rev. B **79**, 115411 (2009).
- 3.72. T. Doppner, T. Fennel, T. Diederich, J. Tiggesbaumker, and K. H. Meiwes-Broer, Phys. Rev. Lett. **94**, 013401 (2005).
- 3.73. A. V. Podlipensky, V. Grebenev, G. Seifert, and H. Graener, J. Lumin. **109**, 135 (2004).
- 3.74. M. Kaempfe, G. Seifert, K. J. Berg, H. Hofmeister, and H. Graener, Eur. Phys. J. D **16**, 237 (2001).
- 3.75. A. Stalmashonak, G. Seifert, and H. Graener, Opt. Lett. **32**, 3215 (2007).

#### Chapter 4

- 4.1. <http://www.codixx.de/>
- 4.2. K. J. Berg, A. Berger, and H. Hofmeister, Z. Phys. D. **20**, 309 (1991).
- 4.3. H. Hofmeister, W. G. Drost, and A. Berger, Nanostruct. Mater. **12**, 207 (1999).
- 4.4. U. Kreibig and M. Vollmer, Optical Properties of Metal Clusters (Springer, 1995).
- 4.5. V.M. Shalaev, Optical Properties of Nanostructured Random Media (Springer, 2001).
- 4.6. J. I. Gittleman and B. Abeles, Phys. Rev. B **15**, 3273 (1977).
- 4.7. P. F. Moulton, Opt. News **8**, 9 (1982).
- 4.8. P. F. Moulton, J. Opt. Soc. Am. B **3**, 125 (1986).
- 4.9. P. F. Moulton, *Tunable Solid-State Lasers*, ed. by P. Hammerling, A. B. Budgor, A. A. Pinto (Springer Ser. Opt. Sci. **47**) (Springer, Berlin, Heidelberg 1985) 4–10.

- 4.10. R. Rao, G. Vaillancourt, H.S. Kwok, C.P. Khattak, *Tunable Solid-State Lasers* ed. by M.L. Shand, H.P. Jenssen (OSA Proceedings Series **5**), (Optical Society of America, Washington, DC 1989) 39–41.
- 4.11. M. S. Pshenichnikov, A. Baltuska, R. Szipocz, D. A. Wiersma, *Ultrafast Phenomena XI* (Springer, Berlin 1998) pp. 3–7; Z. Cheng, G. Tempea, T. Brabec, K. Ferenc, C. Spielmann, F. Krausz., p. 8.
- 4.12. A. Baltuska, Z. Wei, M.S. Pshenichnikov, D. A. Wiersma, *Opt. Lett.* **22**, 102 (1997).
- 4.13. M. Nisoli, S. De Silvestri, O. Svelto, R. Szipocs, K. Ferenc, C. Spielmann, S. Sartania, F. Krausz, *Opt. Lett.* **22**, 522 (1997).
- 4.14. M. T. Asaki et al., *Opt. Lett.* **18**, 977 (1993).
- 4.15. U. Morgner et al., *Opt. Lett.* **24**, 411 (1999).
- 4.16. G. Mourou, *Chirped-pulse-amplification*.
- 4.17. <http://physics.nist.gov/Divisions/Div844/facilities/cprad/cprad.html>
- 4.18. [http://www.bmo.physik.uni-muenchen.de/~wwwriedle/projects/NOPA\\_overview/](http://www.bmo.physik.uni-muenchen.de/~wwwriedle/projects/NOPA_overview/)
- 4.19. Rick Trebino, FROG: Measurement of ultrashort laser pulses, [http://www.swampoptics.com/tutorials\\_FROG.htm](http://www.swampoptics.com/tutorials_FROG.htm)
- 4.20. D. J. Kane and R. Trebino, *IEEE J. Quantum Electron.* **29** (2), 571 (1993).
- 4.21. R. Trebino and D. J. Kane, *J. Opt. Soc. Am. A* **11**, 2429 (1993); K. W. DeLong et al., *Opt. Lett.* **19**, 2152 (1994).
- 4.22. A. V. Podlipensky, “*Laser assisted modification of optical and structural properties of composite glass with silver nanoparticles*” Ph.D. Thesis, Martin-Luther-Universität Halle-Wittenberg (2005).

## Chapter 5

- 5.1. V. M. Shalaev, S. Kawata, *Nanophotonics with surface plasmons* (Elsevier, 2007).
- 5.2. M. L. Brongersma, P. G. Kik, *Surface Plasmon Nanophotonics* (Springer, 2007).
- 5.3. Chakraborty, P. J. *Mater. Sci.* **33**, 2235 (1998).
- 5.4. U. Kreibig, M. Vollmer: *Optical Properties of Metal Clusters*, *Springer Series in Materials Science*, **25** (Springer, Berlin 1995).
- 5.5. V. M. Shalaev: *Optical Properties of Nanostructured Random Media* (Springer, Berlin 2001).
- 5.6. T. Wenzel, J. Bosbach, A. Goldmann, F. Stietz, F. Trager: *Appl. Phys. B* **69**, 513 (1999).
- 5.7. F. Stietz: *Appl. Phys. A* **72**, 381 (2001).
- 5.8. A. L. Stepanov, D. E. Hole, A. A. Bukharaev, P. D. Townsend, N. I. Nurgazizov, *Appl. Surf. Sci.* **136**, 298 (1998).
- 5.9. Y. Shimotsuma, T. Yuasa, H. Homma, M. Sakakura, A. Nakao, K. Miura, K. Hirao, M. Kawasaki, J. Qiu and P. G. Kazansky, *Chem. Mater.* **19**, 1206 (2007).
- 5.10. M. Kaempfe, T. Rainer K.-J. Berg, G. Seifert, H. Graener, *Appl. Phys. Lett.* **74**, 1200 (1999).
- 5.11. M. Kaempfe, G. Seifert, K.-J. Berg, H. Hofmeister H. Graener, *Eur. Phys. J. D*

- 16**, 237 (2001).
- 5.12. G. Seifert, M. Kaempfe, K.-J. Berg, H. Graener, Appl. Phys. B **73**, 355 (2001).
- 5.13. A. Podlipensky, A. Abdolvand, G. Seifert, H. Graener, Appl. Phys. A **80**, 1647 (2005).
- 5.14. A. V. Podlipensky, “*Laser assisted modification of optical and structural properties of composite glass with silver nanoparticles*” Ph.D. Thesis, Martin-Luther-Universität Halle-Wittenberg (2005).
- 5.15. K.L. Kelly, E. Coronado, L.L. Zhao, G.C. Schatz, J. Phys. Chem. B **107**, 668 (2003).
- 5.16. Voshchinnikov, N. V.; Farafonov, V. G. Astrophys. Space Sci. **204**, 19 (1993).
- 5.17. A. Podlipensky, V. Grebenev, G. Seifert, H. Graener, J. Luminesc **109**, 135-142 (2004).
- 5.18. A. Stalmashonak, G. Seifert, H. Graener. Opt. Lett. **32**, 3215 (2007).
- 5.19. A. Stalmashonak, A. Podlipensky, G. Seifert, and H. Graener, Appl. Phys. B **94**, 459 (2009).
- 5.20. W. H. Yang, G. C. Schatz, and R. P. Van Duyne, J. Chem. Phys. **103**, 869 (1995).
- 5.21. M. Futamata, Y. Maruyama, and M. Ishikawa, J. Phys. Chem. B **107**, 7607 (2003).
- 5.22. M. Kaempfe, “*Laserinduzierte deformation metalischer Nanopartikel in Glaeser*”, Ph.D Thesis, Martin-Luther University Halle-Wittenberg, 2000.
- 5.23. A. A. Unal, A. Stalmashonak, G. Seifert, and H. Graener, Phys. Rev. B **79**, 115411 (2009).
- 5.24. N. D. Skelland, J. Sharp and P. D. Townsend, Nucl. Instrum. Meth. B **90**, 446 (1994).
- 5.25. M. Dubiel, H. Hofmeister, E. Schurig, E. Wendler, and W. Wesch, Nucl. Instrum. Meth. B **166-167**, 871 (2000).
- 5.26. N. D. Skelland and P. D. Townsend, J. Non-Cryst. Solids **188**, 243 (1995).
- 5.27. E. Borsella, G. Battaglin, M. A. Garcia, F. Gonella, P. Mazzoldi, R. Polloni, A. Quaranta, Appl. Phys. A **71**, 125 (2000).
- 5.28. N. Del Fatti, C. Voisin, M. Achermann, S. Tzortzakis, D. Christofilos, F. Vallee, Phys. Rev. B **61**, 16956 (2000).
- 5.29. J. Y. Bigot, V. Halte, J. C. Merle, A. Daunois, Chem. Phys. **251**, **181** (2000).
- 5.30. A. Akella, T. Honda, A.Y. Liu, L. Hesselink, Opt. Lett. **22**, 967 (1997).
- 5.31. W. Pfeifer, C. Kennerknecht, M. Merschorf, Appl. Phys. A **78**, 1011 (2004).
- 5.32. A. Melikyan, H. Minassian, Appl. Phys. B **78**, 453 (2004).
- 5.33. F. Calvayrac, P.G. Reinhard, E. Suraud, C.A. Ullrich, Phys. Rep. **337**, 493 (2000).

## Chapter 6

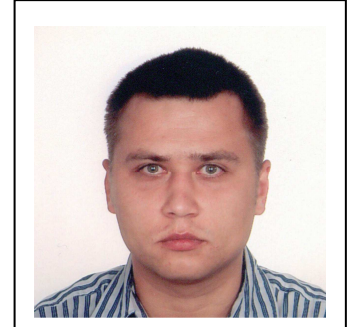
- 6.1. K.L. Kelly, E. Coronado, L.L. Zhao, G.C. Schatz, J. Phys. Chem. B **107**, 668 (2003).
- 6.2. A. Podlipensky, V. Grebenev, G. Seifert, H. Graener, J. Luminesc **109**, 135-142 (2004).

- 6.3. A. V. Podlipensky, “*Laser assisted modification of optical and structural properties of composite glass with silver nanoparticles*” Ph.D. Thesis, Martin-Luther-Universität Halle-Wittenberg (2005).
- 6.4. A. Stalmashonak, A. Podlipensky, G. Seifert, and H. Graener, *Appl. Phys. B* **94**, 459 (2009).
- 6.5. A. Stalmashonak, A. A. Unal, G. Seifert, and H. Graener, *Proc. SPIE* **7033**, 70331Z (2008).
- 6.6. A. Stalmashonak, G. Seifert, and H. Graener, *J. Opt. A: Pure Appl. Opt.* **11**, 065001 (2009).



# Lebenslauf

## Andrei Stalmashonak



25. Mai 1980 in Minsk,  
Weißrussland

Barfüßerstrasse 15  
06108 Halle (Saale)

### **Familienstand**

Verheiratet, keine Kinder

### **Schule**

1986-1997

Dubovlyanskaya Schule No. 1, Weißrussland  
Fachrichtung Mathematik- Physik

### **Studium**

1997-2002

Studium an der Weißrussische Staatliche Universität (BSU), Minsk, Fakultät für Physik, Fach: Atomphysik und physikalische Informatik.

Diplomarbeit mit dem Thema: „Diode-pumped cw tunable two-frequency YAG:Nd<sup>3+</sup> laser with coupled resonators“.

Abschluss: Diplom-Physiker

### **Promotion**

2006-2009

Promotion im Fachbereich Physik, an der Martin-Luther-Universität Halle-Wittenberg.

Leiter der Promotionsarbeit: Prof. Dr. Heinrich Graener.

Promotionsarbeit: „Laser-induced shape transformation of silver nanoparticles embedded in glass“

Verteidigt am 4. Dezember 2009

## **Berufliche Tätigkeit**

- 07.2002-11.2002** Internationales Laser-Zentrum, Minsk, Weißrussland, Wissenschaftlicher Mitarbeiter
- 11.2002-07.2006** Wissenschaftlicher Mitarbeiter im Max-Born-Institut für Nichtlineare Optik und Kurzzeitspektroskopie, Berlin.
- Seit 2006** Wissenschaftlicher Mitarbeiter an der Martin-Luther-Universität Halle-Wittenberg, Fachbereich Physik, Fachgruppe Optik

## **Forschungsbereiche (auf Englisch)**

- 2001-2002** Mode selection of YAG:Nd<sup>3+</sup> laser with coupled resonators
- 2003** The methods for measuring and characterisation of ultrashort laser pulses (Auto- and Cross- Correlation, FROG, Spider)
- 2003-2005** The hollow wave guide technique and pulse shortening by self phase modulation (SPM) and molecular phase modulation (MPM)
- 2003-2004** Laser beam position control with submicroradian precision
- 2003-2005** Femtosecond pulse shaping
- 2005-2006** Hollow waveguides spectroscopy of gases and vapours
- Seit 2006** Interaction of ultrashort laser pulses with metal nanoparticles embedded in dielectric media. Spectroscopic characterization of nanoparticles shape modification.

## **Sprachkenntnisse**

Englisch (gut)  
Deutsch (gut)  
Russisch (Muttersprache)

## **EDV-Kenntnisse**

Windows  
Microsoft Office  
Origin  
CorelDraw  
Labview  
MathCad  
C++, Pascal, Basic

## Publikationen

1. V. G. Gudelev, V. V. Mashko, N. K. Nikeenko, G. I. Ryabtsev, **A. B. Stalmashonak**, and L. L. Teplyashin, "Diode-pumped cw tunable two-frequency YAG : Nd<sup>3+</sup> laser with coupled resonators," *Appl. Phys. B* **76**, 249-252 (2003).
2. I. Shchatsinin, T. Laarmann, G. Stibenz, G. Steinmeyer, **A. Stalmashonak**, N. Zhavoronkov, C. P. Schulz, and I. V. Hertel, "C-60 in intense short pulse laser fields down to 9 fs: Excitation on time scales below e-e and e-phonon coupling," *J. Chem. Phys.* **125**, 194320-15 (2006).
3. **A. Stalmashonak**, N. Zhavoronkov, I. V. Hertel, S. Vetrov, and K. Schmid, "Spatial control of femtosecond laser system output with submicroradian accuracy," *Appl. Opt.* **45**, 1271-1274 (2006), *Virtual Journal of Ultrafast Science* 5(6) (2006).
4. T. Laarmann, I. Shchatsinin, **A. Stalmashonak**, M. Boyle, N. Zhavoronkov, J. Handt, R. Schmidt, C. P. Schulz, and I. V. Hertel, "Control of giant breathing motion in C-60 with temporally shaped laser pulses," *Phys. Rev. Lett.* **98**, 058302-4 (2007), *Virtual Journal of Ultrafast Science* 6(3) (2007), *Virtual Journal of Nanoscale Science & Technology* 15(6) (2007).
5. **A. Stalmashonak**, G. Seifert, H. Graener, A. Podlipensky, M. Leitner, and B. Sepiol, "Multicolor laser assisted deformation of silver nanoparticles in glass," *Physics, chemistry and application of nanostructures: reviews and short notes to Nanomeeting 2007*, Eds.: V. E. Borisenko, S. V. Gaponenko, V. S. Gurin, 172-175 (WSP, Singapore, 2007).
6. **A. Stalmashonak**, G. Seifert, and H. Graener, "Optical three-dimensional shape analysis of metallic nanoparticles after laser-induced deformation," *Opt. Lett.* **32**, 3215-3217 (2007), *Virtual Journal of Ultrafast Science* 6(12) (2007), *Virtual Journal of Nanoscale Science & Technology* 16(22) (2007).
7. **A. Stalmashonak**, A. A. Unal, G. Seifert, and H. Graener, "Optimization of dichroism in laser-induced transformation of silver nanoparticles in glass," *Proceedings of SPIE* **7033**, 70331Z (2008).
8. A. A. Unal, **A. Stalmashonak**, G. Seifert, and H. Graener "Femtosecond shape transformation dynamics of silver nanoparticles in glass," *Proceedings of SPIE* **7032**, 703225 (2008).
9. **A. Stalmashonak**, A. Podlipensky, G. Seifert, and H. Graener, "Intensity-driven, laser induced transformation of Ag nanospheres to anisotropic shape," *Appl. Phys. B* **94**, 459-465 (2009).

10. A. A. Unal, **A. Stalmashonak**, G. Seifert, and H. Graener, "Ultrafast dynamics of silver nanoparticle shape transformation studied by femtosecond pulse-pair irradiation," *Phys. Rev. B* **79**, 115411 (2009), *Virtual Journal of Nanoscale Science & Technology* 19(12) (2009).
11. **A. Stalmashonak**, G. Seifert, and H. Graener, "Spectral range extension of laser-induced dichroism in composite glass with silver nanoparticles," *J. Opt. A: Pure Appl. Opt.* **11**, 065001 (2009), selected as feature article.
12. **A. Stalmashonak**, G. Seifert, A. A. Unal, U. Skrzypczak, A. Podlipensky, A. Abdolvand, and H. Graener, "Towards the production of micro-polarizers by irradiation of composite glasses with silver nanoparticles," *Appl. Opt.* **48**, F38-F44 (2009).
13. **A. Stalmashonak**, H. Graener, and G. Seifert, "Transformation of silver nanospheres embedded in glass into nanodisks using circularly polarized fs pulses," *App. Phys. Lett.* **94**, 193111 (2009), *Virtual Journal of Nanoscale Science & Technology* 19(21) (2009).
14. **A. Stalmashonak**, A. A. Unal, H. Graener, and G. Seifert, "Effects of temperature on laser-induced shape modification of silver nanoparticles embedded in glass," *J. Phys. Chem. C* **113**, 12028-12032 (2009).
15. A. A. Unal, **A. Stalmashonak**, H. Graener, and G. Seifert, "Time-resolved investigation of laser-induced shape transformation of silver nanoparticles in glass," *Phys. Rev. B* **80**, 115415 (2009).
16. G. Seifert, **A. Stalmashonak**, H. Hofmeister, J. Haug, M. Dubiel, "Laser-induced, polarization dependent shape transformation of Au/Ag nanoparticles prepared by ion implantation," *Nanoscale Res. Lett.* **4**, 1380-1383 (2009).
17. **A. Stalmashonak**, O. Kiriyyenko, C. Matyssek, W. Hergert, H. Graener, and G. Seifert, "Effect of local electric field enhancement on the shape transformation of Ag nanoparticles embedded in glass," in preparation.
18. **A. Stalmashonak**, H. Graener, and G. Seifert, "Production of micro-polarizing structures by fs laser irradiation of composite glasses with silver nanoparticles," in preparation.
19. A. A. Unal, **A. Stalmashonak**, H. Graener, and G. Seifert, "Effects of electron emission strengths on the formation of prolate and oblate spheroids from Ag nanospheres," in preparation.

# Acknowledgements

First of all, I would like to thank my supervisor Professor Dr. Heinrich Graener for giving me the opportunity to carry on this research, for fruitful discussions and nice ideas, enthusiasm and constant support in the scientific work.

I have to express my deepest gratitude to Priv.-Doz. Dr. Gerhard Seifert for support, encouragement, and discussions on many aspects of the work.

I must also thank everyone in the optic group, where I have been fortunate to be as a PhD student. Particularly, I am very grateful to Dr. Jens Lange for the technical support and Frau Otten for help in preparing the samples.

I would like to express my thanks to the old members of optic group, particularly, Dr. A. Abdolvand and Dr. A. Podlipensky, who have helped me in the beginning of work in the group.

Many thanks to CODIXX AG for providing samples with Ag nanoparticles for the experiments.

I am very grateful to Mr. F. Syrovatka (IWZ Materialwissenschaft, MLU Halle), Dr. P. Miclea (MLU, Halle) and Dr. H. Hofmeister (Max Planck Institute of Microstructure Physics-Halle) for help with the scanning electron microscopy (SEM) and the transmission electron microscopy (TEM).

Certainly, I greatly appreciate substantial care from my wife Alena and my family.

At the end, I would like to thank all my friends for moral support.



# **Erklärung**

Hiermit erkläre ich, dass ich diese Arbeit selbständig und ohne fremde Hilfe verfaßt, andere als die von mir angegebenen Quellen und Hilfsmittel nicht benutzt und die den benutzen Werken wörtlich oder inhaltlich entnommenen Stellen als solche kenntlich gemacht habe.

Eine Anmeldung der Promotionsabsicht habe ich an keiner anderen Fakultät einer Universität oder Hochschule beantragt.

Andrei Stalmashonak